Ultrafast time-resolved X-ray diffraction using an optimized laser-plasma based X-ray source

Von der Fakultät für Physik
der Universität Duisburg-Essen genehmigte

Dissertation

zur Erlangung des akademischen Grades eines Doktors der Naturwissenschaften
(Dr. rer. nat.)

von

Wei Lu

aus

Guangzhou (China)

Referent: Prof. Em. Dr. Dietrich von der Linde
Korreferent: Prof. Dr. Uwe Bovensiepen

Vorsitzender des Prüfungsausschusses: Prof. Dr. Peter Kratzer
Tag der mündlichen Prüfung: 09. Juli 2013

For Xi Shen

Acknowledgments

The works of this thesis would not have been possible to present here without the helps, assistances and supports of many people. At this point I would like to thank all those who have contributed to this work through any kind of activity.

First of all, I would like to thank my supervisor Prof. em. Dr. Dietrich von der Linde for providing me the opportunity to carry out my PhD study in the exciting research flied of ultrafast time-resolved X-ray diffraction at the University Duisburg-Essen, and also his support for accomplishing this thesis.

A very special thank also to my advisor Dr. Klaus Sokolowski-Tinten, whom it was indeed an honor and a pleasure for me to work with during my PhD study. Without his intensive cares, supports and guidance, this work could not be presented here.

A thank to Prof. Dr. Ulrich Teubner for taking care of me at the initial stage of my PhD studies and also a thank to Priv.-Doz. Dr. Paul Gibbon for his help in the X-ray production project.

I am very grateful to Prof. Dr. Uwe Bovensiepen and Prof. Dr. Peter Kratzer for their agreement to evaluate this work and the related efforts.

I want to thank Dr. Alexander Tarasevitch for his support by maintaining the 10 Hz laser system for all the experiments in this work, and also for many discussions and advices concerning laser – plasma physics.

I also want to thank Dr. Ping Zhou for his valuable helps and advices, for both my study and life in Germany.

To Dr Uladzimir Shymanovich and Dr. Matthieu Nicoul, who are my closest colleagues and also my best friends in Germany, I will never forget the days and nights we spend together in the lab measuring, driving me home many times especially at the midnight after the experiments, giving me advices to improve my skills in both study and life…Thanks for everything you have done for me.

Special thanks to our group secretaries, Kay Eibl and Christina Boese, for their helps in dealing with all the various paperwork and administration issues.

To our technical staffs, I want to thank Michael Bieske for making all the mechanical components, Doris Steeger for all the support cornering electronic devices, and Roland Kohn for all the computer related issues.

I thank Dr. Nicolas Bergeard and Carla Streubühr for their helpful suggestions and comments on this work.

Many thanks go to all the former and current members working in AG von der Linde and AG Bovensiepen: Dr. Nikola Stojanovic, Dr. Ivan Rajkovic, Dr. Manuel Ligges, Dr. Stephan Kähle, Dr. Konstantin Lobov, Dr. Oliver Heinz, Jan Göhre, Jens Wieczorek, Michael Vattilana and Florian Quirin and all of the diploma students and the student assistants who contributed to the wonderful working atmosphere in the groups. I enjoyed all our exchanges very much.

Finally, I want to thank my parents and my wife Xi Shen for their unlimited encouragement and assistance during my PhD studies. I could not have succeeded without their supports. I dedicate this work to them.

Contents

1. Introduction

1.1 Introduction and motivation

In order to study the ultrafast structural dynamics of matter excited by a femtosecond optical pulse, atomic spatial resolution (~Å) and temporal resolution comparable to characteristic time scales of atomic motion (femtosecond to picosecond) are required.

For a long time, static atomic resolution has been achieved by using either X-rays, which were discovered by William Conrad Roentgen in 1895 [1], electrons proved by George Paget Thomson and Clinton Joseph Davisson independently in 1920s [2, 3], or neutrons, which was established by Ernest O. Wollan and Clifford Shull in 1940s [4]. The knowledge of the structure of matter has been largely extended with the application of these invaluable tools. For their outstanding contributions, Roentgen earned the first Nobel Prize for Physics in 1901, Thomson and Davisson shared the Nobel Prize for Physics in 1937, and Shull was awarded one half of the 1994 Nobel Prize in Physics.

On the other hand, the temporal resolution had made no significant improvement until the development of femtosecond laser technology [5, 6]. Since then, the situation has changed rapidly. New types of radiation sources have been developed or are being developed to provide ultrashort pulses of photons or electrons with sufficiently short wavelength to enable the direct observation of structural changes on the relevant length- and time-scales. In the late 1980s/early 1990s, the first laser-produced plasma femtosecond x-ray sources were demonstrated [7-9]. In the early 2000s, ultrafast electron diffraction with sub-picosecond time resolution was realized [10-13]. In the mean time, also accelerator based short-pulse X-rays sources have been developed [14-18]. However, until now it has not been possible to generate ultrashort (sub-picosecond) pulses of thermal neutrons.

In the works presented in this thesis, ultrashort X-ray pulses are used as a tool to investigate ultrafast structural dynamics. Currently, there are six techniques exist to

produce femtosecond X-ray pulses:

1) Ultrafast X-ray tube, achieved by using pulsed femtosecond lasers to produce pulsed electron injection within a normal X-ray tube [19-21].

2) Direct conversion of the laser pulse into the X-ray region by nonlinear optical processes, i.e. high order harmonic generation（HHG）[22-25].

3) laser-produced plasma X-ray source, achieved by the interaction of high intensity laser pulses with solid targets [7-9].

4) The very recent developed laser-plasma wakefield accelerator-based betatron X-ray source [26-29].

5) Unlike the previous four laboratory-sized techniques, the large-scale electron synchrotron-based slicing X-ray sources, such as the Advanced Light Source "ALS" in Berkeley, USA [14], the Berliner Elektronenspeicherring-Gesellschaft für Synchrotronstrahlung "BESSY" in Berlin, Germany [15], the Swiss Light Source "SLS" in Villigen, Switzerland [16].

6) The large-scale linear accelerator-based X-ray Free electron lasers (XFEL), such as the Linac Coherent Light Source "LCLS" at SLAC in Standford, USA [30], the SPring-8 Angstrom Compact free electron LAser "SACLA" in Japan [31] and the X-ray Free-Electron Laser "XFEL" at DESY in Hamburg, Germany [32, 33].

For all of these ultrafast X-ray sources, the femtosecond laser pulses have to be employed in some ways, and the accelerated electrons play important roles in the conversion process. Each of these sources has its own characteristics in terms of the repetition rate, the minimum achievable pulse duration, the produced photon number, the photon energy range, the spatial and temporal coherence properties and the size or the cost of the installation.

Presently, the first two sources are not yet suitable for studying ultrafast structural dynamics due to the limited overall X-ray production. The betatron X-ray source is still under development [34-38]. The last two large-scale X-ray sources represent the most promising X-ray sources for performing ultrafast time resolved experiments. However, their construction and running costs are extremely high, and beam time access is very limited. The laser-produced plasma X-ray sources are presently unique because they are the easiest to operate laboratory-sized X-ray source that can deliver hard X-ray radiation with very short pulse duration, and at the same time provide perfect synchronization between the produced X-ray pulses and the

driving femtosecond laser pulses. This is the type of X-ray source that has been used for performing the time resolved X-ray diffraction experiments presented in this thesis. A part of the work in this thesis is dedicated to optimizing the X-ray emission from this X-ray source.

To obtain the time dependent information in sub-picosecond time scale, the common method using a fast detector (e.g. photo diodes or streak cameras) with one ultrashort pump pulse is not accessible due to the limited temporal-resolution capability of current fast detectors. Most experiments are performed in the ultrafast-pump–ultrafast-probe scheme with a slow detector. With this scheme, the time evolution of photoinduced structural changes can be studied by taking a sequence of diffraction patterns at different time delays with respect to (femtosecond) excitation. Since the ultrashort X-ray pulse was available, this scheme has been further extended to X-ray region. Using laser-pump X-ray-probe scheme, the first femtosecond time-resolved X-ray diffraction experiment was performed with laser plasma X-ray source in 1997 by Rischel *et al.* [39]. Since then, many ultrafast phenomena have been investigated by using ultrashort X-ray pulses. Reviews on these studies can be found in Ref. [40, 41]. The current researches cover the following fields:

1) Propagating GHz acoustic waves caused by the release of impulsive stress launched by the femtosecond optical excitation. [42-67]

2) Coherent optical phonon excitations which connect with unit-cell level transient structural changes. [67-73]

3) Non-thermal melting, which is melting before thermal equilibrium between electrons and lattice has been established after femtosecond laser excitation. [17, 18, 39, 46, 76-81]

4) Phase transition in ferroelectric [66, 82-87] and ferromagnetic [88-104] materials caused by femtosecond laser excitation.

5) Debye-Scherrer type time-resolved X-ray measurements on polycrystalline and powder samples, which allow obtaining much more information of the excited sample from one measurement through detecting simultaneously several diffraction orders, similar to studies by ultrafast electron diffraction. [105-110]

6) Utilizing X-ray diffuse scattering to investigate the transient nonequilibrium states of the lattice system following ultrafast laser excitation. [111, 112]

The ultrafast phenomena investigated in this thesis focus on structural dynamics in thin laser-excited metal films. These works covered by the research field includes

coherent excitations of acoustic phonons and optical phonons.

1.2 Overview and structure of the thesis

The thesis is organized as following:

Chapter 2 presents experimental results on the optimization of K_α X-ray emission from a laser-plasma based X-ray source. It contains the principle of X-ray generation with a laser produced plasma and a systematic investigation of optimizing the X-ray emission.

Chapter 3 describes a modular setup for time-resolved X-ray diffraction experiments. This chapter presents and discusses implemented improvements of the setup, such as hardware, software and methodology, which are essential to achieve the results of following time-resolved diffraction experiments.

Chapter 4 deals with the first time-resolved X-ray diffraction experiment with the improved modular setup. The Debye -Waller effect in a thin laser-excited Au film is observed. The evolutions of the lattice temperature are compared with the theoretical prediction of Two-Temperature Model (TTM).

Chapter 5 contains the study on the photoinduced softening of the A_{1g} optical phonon mode in laser-excited Bi. This work extends the studies of coherent optical phonons in laser-excited Bi to a higher fluence range that has not been studied previously.

Chapter 6 focuses on the experiments performed with X-ray Debye-Scherrer diffraction scheme. A static measurement on a Cu foil (20 μm) and a time-resolved measurement on an Au thin film (200 nm) have been carried out. The temporal behaviors of the measured data are discussed.

The last chapter summarizes the main results presented in this thesis. An outlook for the future studies is also provided.

2. Optimization of a laser-plasma based X-ray source

This chapter discusses the principles of X-ray generation using a laser-produced plasma and strategies to optimize the X-ray source for time-resolved X-ray diffraction experiments discussed in the following chapters. For this purpose the K_α-emissions from plasmas on Ti and Cu targets for different excitation and plasma conditions were investigated. Section 2.1 describes the mechanism for generating ultrashort X-ray pulses using the laser-produced plasma. The laser system and the experimental setup are presented in sections 2.2 and 2.3, respectively. Section 2.4 discusses the optimization of the K_α yield as a function of laser intensity. Measurements of the K_α yield as a function of target thickness and angle of incidence, and a detailed investigation of the influence of a pre-formed plasma by using a controlled pre-pulse with variable delay are presented and discussed in section 2.5. The experimental data show that for a given angle of incidence the K_α yield can be optimized by choosing a suitable pre-pulse, i.e. plasma scale-length conditions. For large angles of incidence a steep electron density gradient maximizes the yield. At near normal incidence maximum yield is achieved for a more expanded plasma, and the best energy conversion efficiency has been found in this case. For a certain scale-length range (between $0.1\lambda - 1\lambda$, here λ is the laser wavelength) the optimized yield is scale-length *independent.* It can be achieved by choosing the appropriate angle of incidence. This situation results from the strong dependence of collisionless absorption mechanisms – in particular resonance absorption (RA) – on the angle of incidence and the plasma scale length: By maximizing the absorption the highest K_α yield is achieved. The experimental data are supported by the results of calculations based on the classical resonance absorption mechanism (section 2.5) and of particle-in-cell (PIC) simulations (section 2.6). Finally, a summary of this chapter is given in section 2.7.

2.1 Generation of ultrashort X-ray pulses from laser-produced plasma

Optical radiation is absorbed by a metal within a thin layer of about 10 nm which is called the "skin depth" [113]. If the intensity of the laser radiation on the material is large enough, typically more than 10^{14} W/cm^2, the target material within the skin depth will be ionized and transformed into a plasma during the pulse. For laser intensities above 10^{15} W/cm^2, easily achievable with current femtosecond laser technology, it has been found that the hot plasma emits radiation in the (hard) X-ray range [7]. The emitted radiation consists of continuum emission from recombination in the plasma, characteristic line emission (K_α, K_β…) and Bremsstrahlung radiation. The latter two components come not only from the hot plasma resulting from transitions on the strongly ionized atoms, but also the interaction of high energy electrons, accelerated by the intense laser field, with the *cold*, non-excited material underneath [7, 9, 114, 115]. These laser-accelerated electrons, often called "*hot*" electrons in the laser plasma community, have a kinetic energy (~10…100 keV) significantly higher than the thermal energy of the overwhelming part of the plasma electrons. Among the three different contributions to the X-ray emission mentioned above, the characteristic line emission, especially K_α emission, is particularly interesting for applications (e.g. time-resolved X-ray diffraction). The generation of characteristic line radiation during the irradiation of a solid material with an intense femtosecond laser pulse is described detail in Ref. [9, 116-118].

The mechanism of K_α X-ray emission from a laser induced plasma is very similar to that in an ordinary X-ray tube. However, the static electric field used for electron acceleration is replaced by the femtosecond laser electric field. A brief description of the process of K_α radiation generation is given in Fig. 2.1. The interaction of a high intensity laser beam with a solid surface rapidly creates a plasma. The plasma electrons, interacting with the strong electric field of the incident femtosecond optical pulse, can acquire an energy which is high enough to leave the skin layer and penetrate into the non-excited material underneath the surface plasma layer. Some of these electrons will be slowed down and generate Bremstrahlung. Others collide with the non-excited atoms, kick out electrons from their inner electronic shells, which subsequently undergo inner shell recombination, leading to characteristic line emission. Therefore, the emission of the characteristic line radiation can only occur as long as the high energy

electrons are present, and can be regarded as a direct result of these "*hot*" electrons. These electrons exist only during the femtosecond laser pulse irradiation (and for a very short time afterwards which is determined by the flight-time of the high energy electrons through the material). Thus, one can expect that the duration of the X-ray pulses produced in this way is comparable to the laser pulse duration, i.e. in the sub-picosecond region [119-122].

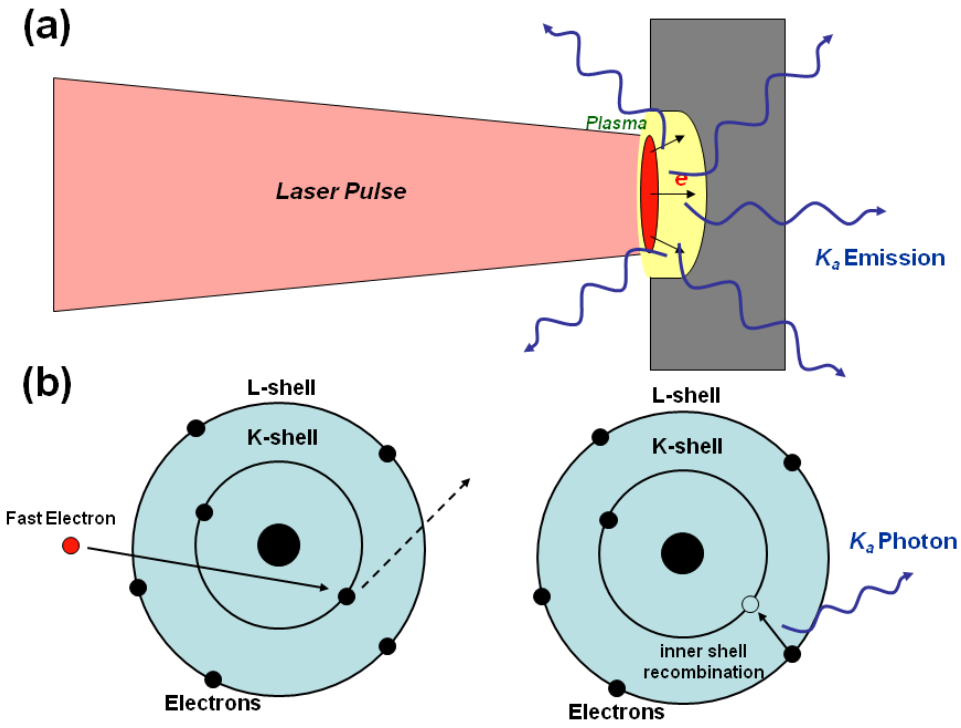

Fig. 2.1 Scheme for the generation of K_α radiation by focusing an ultrashort laser pulse on a solid target. (a) The focused laser pulse produces plasma on the surface of solid target (red area). Accelerated electrons from the plasma travel into non-excited material and produce there X-rays (yellow area). (b) The ionization of K-shell electrons and the subsequent inner shell recombination leads to K_α-emission.

The energy distribution and the corresponding number of these "*hot*" electrons have a strong influence on the characteristics of the emitted radiation, in particular the K_α yield. The task to optimize the conditions for K_α X-ray generation turns into the investigation of how the laser energy is converted into "*hot*" electrons with the appropriate energy distribution and their following dynamics inside the non-excited material. The energy conversion is dominated by the laser absorption mechanisms, which are in turn determined by the parameters of the driving laser, i.e. intensity, angle

of incidence, laser polarization, as well as by the properties of the plasma with which the laser pulse interacts [119, 123]. The subsequent interaction of the "*hot*" electrons and the solid is mainly via collisions. The mean free path of the "*hot*" electrons (or the stopping distance) and the ionization cross section in the solid dominate the rate of K_α emission [124-126]. Several studies based on simulations (particle-in-cell simulation [127] + Monte Carlo transport code [128]) were performed to investigate this question. Depending on the target material (Z) and the sample thickness, the simulations allowed to determine the laser parameters (i.e. laser wavelength, intensity, polarization and pulse duration), which lead to the optimum electron distributions for K_α emission [121, 129-131]. These results are in good agreement with previous experimental data [9, 115, 132, 133-137].

In this study, the effects of laser intensity, target thickness, angle of incidence and precise controlled pre-plasma conditions on the K_α-production from Cu and Ti elements are the objects for investigation. To my knowledge, systematic investigations of the latter two effects on both elements were first performed.

2.2 Laser system

In this section, the laser system used as a driver for the laser-plasma based X-ray source is described and some key parameters of this laser system are presented.

The 10-Hz Titanium-Sapphire femtosecond terawatt laser system at the University of Duisburg-Essen is based on the Chirped Pulsed Amplification (CPA) technique [5, 6, 138]. Its working principle can be briefly described as follows: A low energy femtosecond pulse produced by an oscillator first passes through a so-called “stretcher”. The stretcher consists of a dispersive delay line (gratings) and adds a controlled phase modulation to the laser pulse, thereby increasing its duration and decreasing its peak intensity. Typical stretching factors are 10^4. The “stretched” pulse can then be amplified to high energies, usually by several amplification stages. After amplification the pulse passes through the so-called “compressor”, which compensates the phase modulation imposed by the stretcher as well as any additional phase modulation acquired during amplification (for example due to material dispersion). Ideally the amplified pulse is recompressed to its original duration. This technique allows to produce high peak power laser pulses without deteriorating the pulse parameters and damaging the optical components during the amplification process.

The main components of the laser system used in the experiments are shown in Fig. 2.2. The "heart" of the system is a mode-locked titanium-sapphire oscillator pumped by a frequency doubled cw Nd:YVO_4 laser (type Coherent Verdi, diode-pumped , λ = 532 nm, P = 5 W). It produces a train of 45 fs (full width half maximum - FWHM) pulses with a repetition rate of 80 MHz and an energy of ~1 nJ per pulse. The central wavelength of the pulses is 800 nm with a spectral bandwidth (FWHM) of 21 nm.

The output pulses from the oscillator are directed to the stretcher, in which the duration of the pulses is extended to 200 ps. A grating with 1200 lines/mm is used in the stretcher as dispersive element for broadening the pulses. Before the pulses enter the amplification stages, the repetition rate is reduced to 10 Hz using an electro-optic selector consisting of a Pockels cell and a polarizer. By inducing a suitable fast switching electric field, this combination allows the precise selection and separation of pulses at a repetition rate of 10 Hz from the initial 80 MHz pulse train.

The following amplification system consists of two multipass stages, both using Ti:Sapphire crystals as gain medium, pumped by frequency doubled Q-switched Nd:YAG lasers (532 nm). In the first stage, the seed pulses make eight passes through the amplifying medium and are amplified to a pulse energy of about 1 mJ (amplification by a factor of approximately 10^6 - 10^7). The second stage is a four-pass power amplifier. To obtain homogeneous pumping, two lasers pumping from both sides of the amplifying medium are applied. After four passes in the second crystal, the pulse energy pulse is increased to about 200 mJ (amplification by a factor of approximately 100). Finally, the amplified pulses enter the compressor. The compressor contains again gratings as dispersive elements to recompress the pulse to the desired pulse duration. If the compressor is operated under vacuum, a maximum energy per pulse of 150 mJ with a minimum pulse duration of about 45 fs can be achieved. In the experiments discussed here, the compressor is operated in air and the pulse duration is adjusted to approximately 120 - 150 fs. With this duration self-phase-modulation (and self-focusing) in air can be avoided, and the pulse properties (spectrum, spatial beam profile) are not deteriorated during propagation.

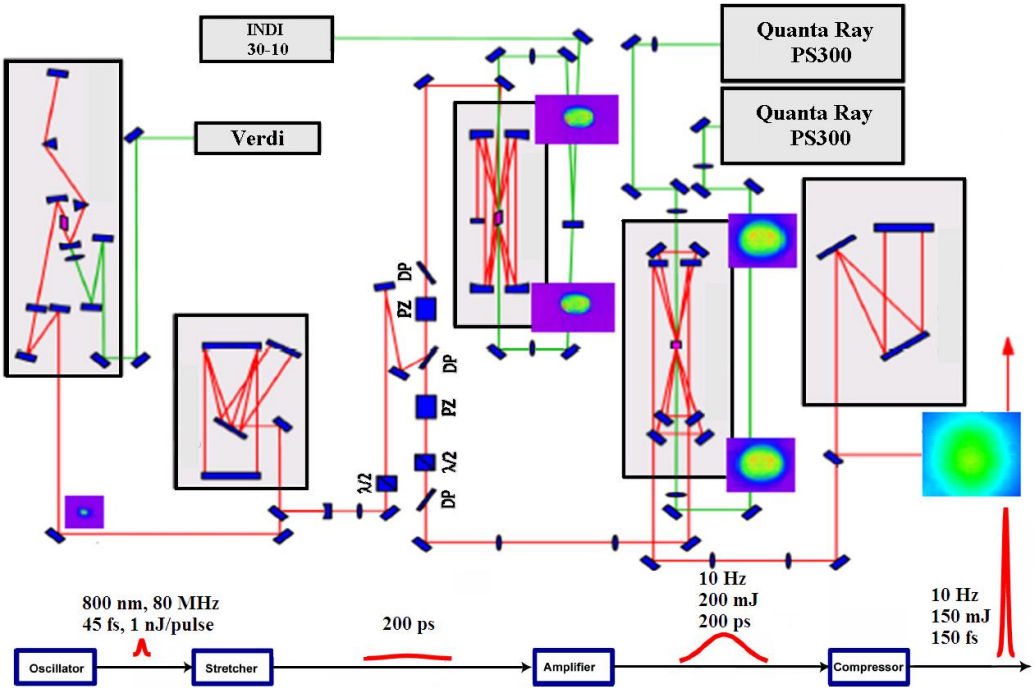

Fig. 2.2 The principle scheme of the laser system

The time-structure of the final output pulses was measured a third-order autocorrelator (fs- to ps-time-range). The amplified laser pulse exhibits a relative intensity of about 10^{-7} (i.e. contrast ratio of 10^{7}) approximately 1 ps ahead of the pulse maximum and the contrast ratio to the amplified spontaneous emission (ASE) is 10^{8} [139]. Due to such a high-contrast ratio the pre-plasma formation caused by laser pulse itself is negligible in the experiments presented later.

The key parameters of the laser system are summarized in the table 2.1 below:

central wavelength	800 nm
spectral width	21 nm
min. pulse duration	45 fs
in air pulse duration	120 ... 150 fs
maximum pulse energy	150 mJ
contrast ratio at 1 ps	10^{-7}
ASE	10^{-8}
repetition rate	10 Hz
beam diameter (FWHM)	25 mm

Table 2.1: Key parameters of the 10 Hz laser system.

The stability of the laser system, i.e. energy and pointing stability, is very important for the experiments presented in this thesis. Energy and pointing stability were recorded and analyzed pulse-to-pulse over a few hours by U. Shymanovich [140].

Typical values under normal working conditions are less than 100 μrad pulse-to-pulse pointing instability and 2.5% rms energy fluctuations.

2.3 Experimental setup

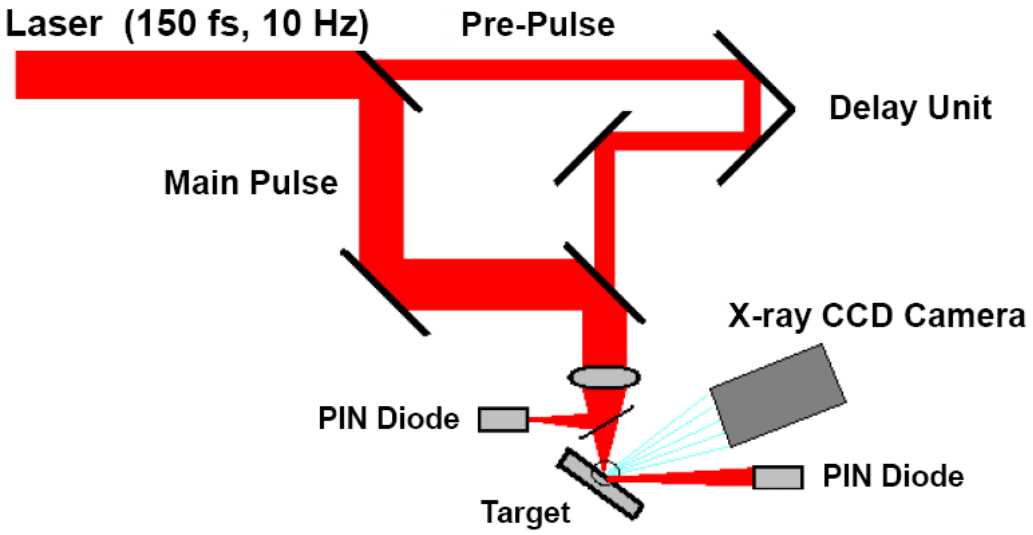

Fig. 2.3 Schematic of the experimental setup for K_α optimization.

All the works presented in this thesis were done with a few different experimental setups. For the investigation of the K_α production, a setup, as schematically shown in Fig. 2.3, was used. The 25 mm diameter (FWHM) p-polarized laser beam was reflected from a mirror with a 5 mm diameter hole in its center that allowed transmission of a small part of the beam. The transmitted part was time delayed with a variable delay line, and recombined with the main laser beam, using a second apertured mirror. The combined p-polarized laser beams were focused with a 30 cm focal length lens onto the target surface. This lens could be accurately translated along the direction of the laser beam propagation to change the focusing conditions, i.e. the focus size, on the target. Two PIN photodiodes, one for recording the incident energy and another for the reflected energy, were used to measure the reflectivity, from which the absorption of the laser energy can be deduced. By using a microscope objective combined with a CCD camera, the focal spot sizes of main and pre-pulse were measured as ~ 20 μm and ~ 70 μm FWHM, respectively. The focal area of the pre-pulse is about 12 times bigger than that of the main pulse and both pulses can be adjusted to spatially overlap well at all delay times. The angle of incidence was varied by rotating the target. For each specific angle, *the laser intensity was kept constant* by adjusting the laser energy. The targets were mounted on a motorized XYZ translation unit and moved between

consecutive laser pulses to provide a fresh surface for each pulse. In these experiments, four kinds of targets were used: 300 nm Cu and Ti films coated on a glass substrate and 20 μm Cu and Ti foils glued onto a glass substrate.

The X-ray radiation was detected with a Princeton Instruments CCD-camera (type PI-MTE: 1300B). It is back-illuminated Si-CCD that is suitable for the photon energy range relevant in this work (i.e. 2 to 10 keV). The chip area is 1340 pixels × 1300 pixels (20 μm × 20 μm each). The camera was located ~ 20 cm away from the X-ray source, and the average X-ray flux per pulse was reduced to 1 photon per 40 pixels by using an Al filter of moderate thickness (150 μm and 210 μm for Ti and Cu, respectively) in front of the camera. The filter also protected the CCD from low energy Bremsstrahlung and from visible light. This configuration allowed the camera to work in "single photon counting regime" as a spectrometer exploiting the fact that a X-ray photon detected with the CCD creates a charge strictly proportional to its energy (for Si the electron-hole pair creation energy is 3.66 eV [141] and thus a single Cu K_α photon (8.05 keV) will produce about 2200 photoelectrons). Therefore, one can obtain the energy spectrum of the detected X-rays from the distribution of the signal of all camera pixels (signal histogram of the recorded images). A typical single-pulse spectrum using Cu as target, with well resolved Cu K_α and K_β lines at 8.05 keV and 8.91 keV, respectively, is shown in Fig. 2.4. The single-pulse spectra of Ti, which are not shown here, are similar. The K_α yield can in principle be obtained by integrating the signal in the relevant energy range after appropriate background subtraction.

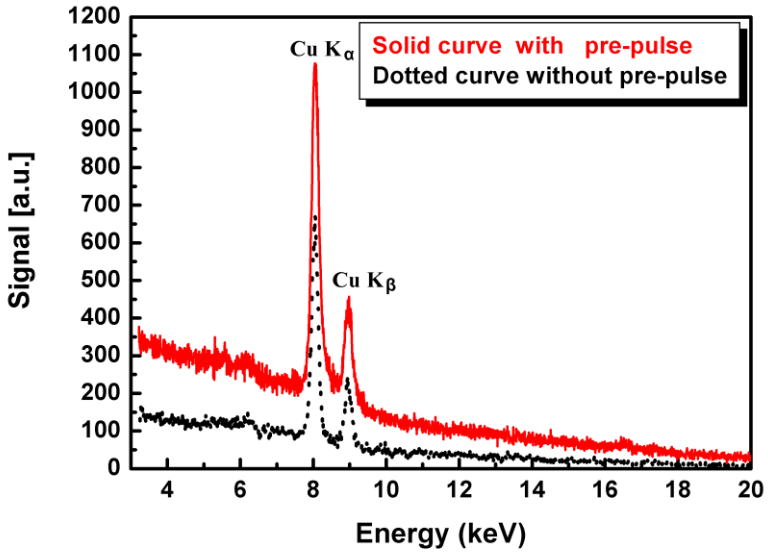

Fig. 2.4 Spectrum of the laser produced K_α emission of Cu.

However, to determine the absolute K_α yield of the source it has to be considered that a single X-ray photon not always generates charge in only a single CCD pixel, but that the generated charge may be distributed over many pixels ("many-pixel-events")[142]. This distorts the measured spectra and leads to an underestimation of the K_α yield since a "many-pixel-event" created by a single K_α-photon is detected/counted as several photons of apparently lower energy. For Ti and Cu K_α radiation, the spatially largest events involve 4 pixels as reported in Ref. [142]. In order to determine the percentage of single-pixel events in the detection system, a few images were randomly sampled from all the measured data and analyzed in detail. It was found that about 50% of all detected K_α-photons generated single-pixel events, while the other 50% were 2-, 3- and 4-pixel events (the number of events involving 5 and more pixels was negligible). Therefore, a correction factor of 2 was applied to the number of detected K_α-photons determined from the integration of the spectra. To derive from this the absolute K_α yield the transmission of the Al filters as well as the quantum efficiency of the CCD (18% at 8 keV, 55 % at 4.5 keV) [143] was taken into account. Moreover it was assumed that the X-ray emission is isotropic into the full solid angle.

2.4 Optimization of K_α X-ray emission by adjusting the laser intensity

In this section, the experimental results concerning the optimization of the K_α X-ray emission are presented. Two key factors, namely laser intensity and the pre-plasma scale length, were varied to study their influence on the K_α yield.

As mentioned in section 2.1, to efficiently ionize the K-shell electrons of the target material which in turn lead to an efficient X-ray emission, "*hot*" electrons with the appropriate kinetic energy should be produced. The kinetic energy of these "*hot*" electrons is strongly dependent on the accelerating laser field. Therefore, the laser intensity is one of the key factors to control and optimize the K_α generation. The average energy of the accelerated electrons, often described by an effective *"hot"* electron temperature T_h, generally relates to the pondermotive potential of the laser field and follows a power scaling law: $T_h \sim (I\lambda^2)^{1/3}$ [144, 145], as observed in many experiments [115, 146-148], and also found with PIC simulations [119]. For optimum K_α emission, the average electron energy should be a few times the K-shell ionization energy, depending on the geometry of the target and the atomic number [121, 129, 137,

[149].With this condition the laser intensity for optimum K_α production can be estimated. For example, to maximize the yield of Cu K_α (8.05 keV) radiation, the average electron energy should be between 25 keV and 50 keV [120, 121, 129, 148, 150, 151]. With the mentioned empirical scaling law $T_h \sim (I_0\lambda^2)^{1/3}$ this average electron energy corresponds to a laser intensity of a few times 10^{17} W/cm^2 at a laser wavelength of 800 nm [120, 121, 137]. For Ti, the predicted optimum laser intensity is a few times 10^{16} W/cm^2 [121, 152].

With the given focal length (30 cm) a maximum laser intensity of 1.6×10^{17} W/cm^2 can be achieved. The laser intensity dependence is investigated by varying the relative position of the laser focus with respect to the target surface. In this way the laser intensity on target changes while the pulse energy is kept constant. No additional pre-pulse is applied in this experiment. Fig. 2.5 shows the experimentally determined (normalized) K_α yield from 20 μm Cu and Ti foils as a function of the position of the target surface relative to the focus of the lens. In this measurement no attempt was made to convert the position scale into an intensity scale, but it is obvious that the K_α emission for the different target materials is optimized/maximized at different lens positions and thus at different intensities. For Cu the sharpest focusing and thus the highest intensity provides the largest K_α emission. For Ti this is achieved out of focus and thus at a lower intensity. This effect has been discussed before in the literature [130, 152, 153]. Fig. 2.5 indicates that for Ti, the "optimum" intensity for K_α-production is reached and exceeded in the experiments. This optimum intensity is lower than the maximum laser intensity reached at the focus, as predicted by theory [121]. For a Gaussian beam it is expected that the change of the spatial intensity distribution should be symmetric with respect to the focus. The asymmetry of the measured double-peak dependence of the Ti K_α yield indicates that this is not the case in the experiment. This is attributed to the method (hole in a mirror) used to split off the pre-pulse, that was used for the measurements described below, from the main pulse, leading to a non-Gaussian intensity distribution. For the higher atomic number material Cu, the optimum conditions for K_α-production correspond to higher laser intensity. Since no double-peak structure is observed for Cu it can be concluded that the maximum intensity used in the experiment is comparable or below the expected optimum value for this material, again in agreement with the predictions and estimates mentioned above.

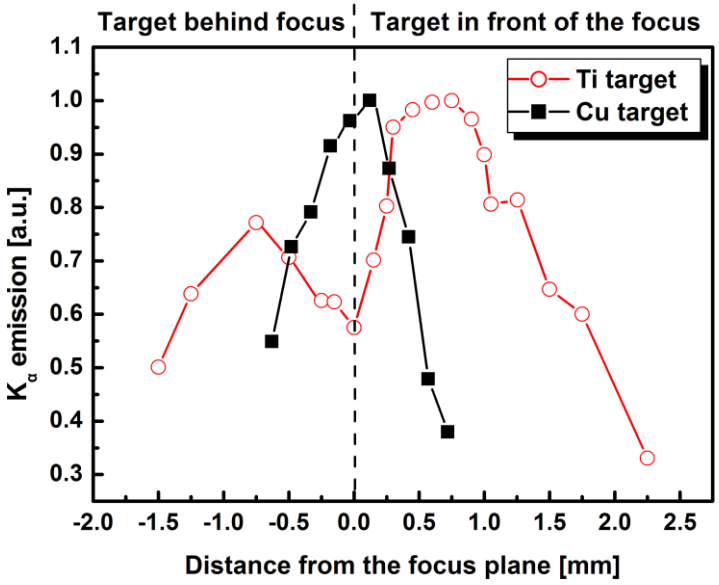

Fig. 2.5 K_α emission as a function of the relative position of the target surface of 20 µm Cu and Ti foils with respect to laser focus. The lines between the data points are only to guide the eye.

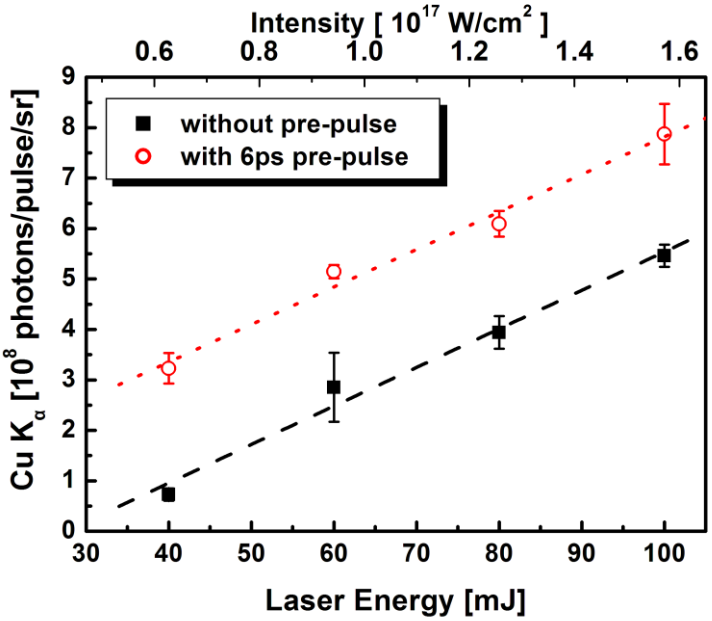

Fig. 2.6 Measured dependence of X-ray yield on laser energy for a 20 µm Cu foil. The angle of incidence is 45 °.

Since Cu K_α radiation has been used for the time-resolved diffraction experiments discussed in this thesis the emission from a Cu target has been investigated further. Keeping the spot size (position of the lens) fixed, a precise measurement as function of laser pulse energy was performed and it provided more detailed information on the laser intensity dependence with this target material. For laser energies above 30 mJ and intensities in the region from 10^{16} W/cm^2 to 10^{17} W/cm^2, the Cu K_α yield scales linearly

with laser energy/intensity - Fig. 2.6. There has been no evidence of saturation, in agreement with theoretical calculations which predict an optimum intensity for Cu K_α-production of a few times 10^{17} W/cm^2 [121, 137]. Additionally, a data set with a controlled pre-pulse arriving 6 ps before the main pulse is also presented in this figure. An obvious improvement in the K_α-production is observed. A detailed discussion of this effect will be presented in the next section. The maximum absolute yield obtained in this measurement is in line with other reported Cu K_α sources [107, 148, 154, 155].

2.5 Optimization of K_α X-ray emission by using a controlled pre-plasma

Another approach for optimization of the K_α emission is to improve the energy conversion efficiency, from the laser pulse to electrons and subsequently to K_α photons. The dominant absorption mechanism at laser intensities around 10^{17} W/cm^2 is expected to be resonance absorption (RA) [116, 121, 131, 133, 152, 156-158]. The crucial parameter for the efficiency of the energy transfer for this mechanism is the plasma density scale length at the time when the maximum pulse intensity is reached. Assuming isothermal plasma expansion an exponential electron density profile $n_e(x) = n_{e0}\exp(-x/L)$ is produced [159], and the plasma density scale length L is defined as : $L = n_e / |\nabla n_e|$. Since the plasma expands with a typical velocity of ~10^6–10^7 cm/s [160-162], the time interval between the plasma-formation threshold and the maximum intensity largely determines the scale length seen by the pulse during the interaction. Therefore, the conversion efficiency in this case is very sensitive to the temporal structure of the rising edge of the laser pulse. For this reason, control over the time structure of the pulse provided by the laser system becomes important to control the K_α emission. An important parameter of the laser pulse time structure is the contrast ratio, defined as the ratio of intensity of the pulse at the maximum and pre-pulses/background before the main pulse. In some previous work [130, 148, 152, 156] using laser systems with low contrast ratio, pre-pulses and/or amplified spontaneous emissions (ASE) usually cause plasma formation long before the peak of the pulse reaches the target. Such long pre-plasma scale lengths provided by the laser systems already lead to strong absorption, making additional improvements difficult. However, relying for a particular laser system only on its inherent pre-pulse for “optimization” is hardly satisfactory because the scale length will rarely be optimized and matched to other parameters. On the other hand, with a very

high contrast laser system it has already been demonstrated that introducing a pre-formed plasma using a weak artificial pre-pulse can increase the conversion efficiency of the X-ray yield from laser produced plasmas [118, 137, 163-167] (this effect is also visible in Fig. 2.6). Therefore, systematic investigations of the plasma scale length requirements for different experimental conditions are necessary. In this section, the mechanism of the resonance absorption will first be explained. Then the experimental results are presented, followed by their discussion.

2.5.1 The resonance absorption (RA) and its optimum condition

The resonance absorption occurs when an electromagnetic wave with p-polarization (the electric field in the plane of incidence) is obliquely incident in an unmagnetized, inhomogeneous plasma. In this process, the electromagnetic wave couples with the electron plasma wave at the region of critical density (defined as $n_c = m\omega_L^2/4\pi e^2$, where *m* and *e* are the charge and the mass of the electron respectively and ω_L the angular frequency of the laser light.), where the local electron plasma frequency equals the incident wave frequency. There, the energy is effectively transferred from the incident electromagnetic wave to electron plasma wave and the electron plasma wave can be resonantly enhanced. As the electron plasma wave grows, nonlinear wave-breaking [168, 169] can lead to the consequent production of "*hot*" electrons.

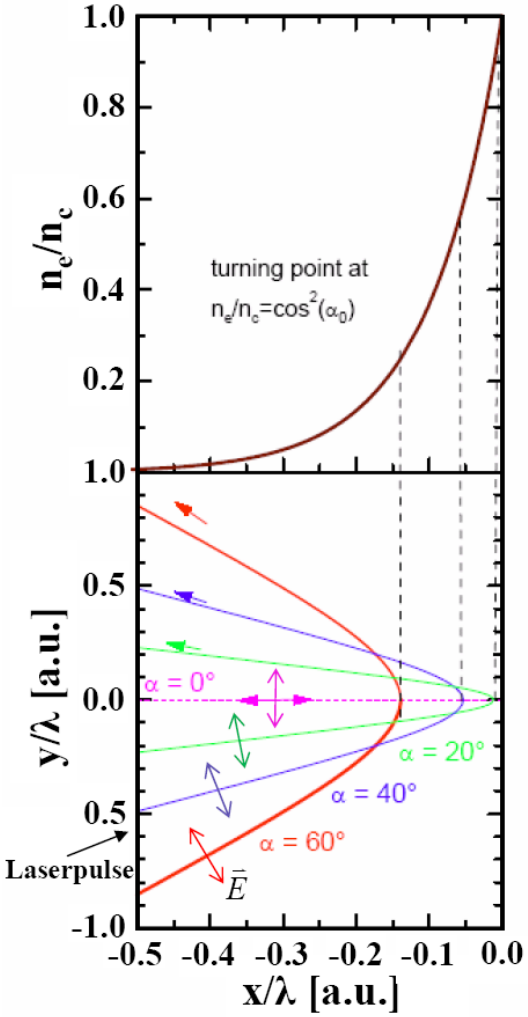

Fig. 2.7 Scheme of oblique incident laser pulse traveling inside a plasma. The red, violet, green and magenta trajectories represent the propagation path of the incident laser pulses with angle of incidence of 60 °, 40 °, 20 ° and 0 °, respectively. The double arrows perpendicular to the trajectories represent the polarization of the electric fields (p-polarization). The trajectories are reflected before reaching the critical density layer, where $n_e/n_c=1$. The turning point depends on the angle of incidence.

A simple theoretical estimate of the optimum condition for RA is given by the formula: $(2\pi L/\lambda)^{2/3}\sin^2\alpha_{max} = 0.6$ [147], where L/λ is the plasma scale length normalized to the laser wavelength, α_{max} is the angle of incidence at which RA is optimized. This equation is obtained by solving the wave equation for light wave propagation in a plasma with linear density profile. It expresses an important relation between the plasma scale length and α_{max}: *the angle of incidence for the optimum absorption decreases with increasing plasma scale length.* The mechanism can be described qualitatively in Fig 2.7. The absorption occurs in the critical density region, where $n_e=n_c$, n_e is the local electron density in the plasma. The total absorption depends on

how large the field driving the resonance is at the layer of critical density. This field is firstly determined by the angle of incidence because only the field component along the density gradient, which varies as sinα, contributes to the excitation of electron plasma wave. Secondly, since the refractive index of the plasma in the undercritical region decreases with increasing density (i.e. Drude-model) an obliquely incident light wave is refracted towards regions of lower density and "reflected" at a density lower than the critical density ("turning point") with $n_e = n_c \cos^2\alpha$ [147]. Although the laser light wave can propagate only up to turning point before it is specularly reflected, some amount of the light energy will tunnel into the critical density region and drive the resonance. The value of this driving field at the turning point can be estimated using the Airy function solution [170] and it decays exponentially depending on its travel distance as it penetrates beyond the turning point. Thus the resulting driving field at the layer of critical density is a competition between maximization of the electric field component along the density gradient and the distance of the field penetration beyond the "turning point". Particularly in the situation of the experiments that will be presented later, for a long scale-length system (e.g. $L/\lambda \approx 1$), the turning point of a steep angle of incidence is closer to the layer of critical density as one can see in the Fig. 2.7. Although the field component normal to the density gradient is weak in this case, the short attenuation distance to the critical density surface provides a stronger driving field than the one with large angle of incidence, which has large field components normal to the density gradient, but the field decay dramatically due to the large "tunnel" distance to reach the critical density surface. The stronger driving field at a small α (e.g. ≈ 25°) leads to the stronger absorption than with a large α (e.g. ≈ 55°). On the other hand, for a short scale-length system (e.g. $L/\lambda \approx 0.1$), the positions of turning points of all incidences are all close to the layer of critical density thus the attenuations of their driving fields due to the "tunnel" distance are neglectable,. With increasing angle of incidence α (e.g. ≈ 55°), the electromagnetic wave spends progressively more of its time near n_c and the excitation of the electron plasma wave at the critical density layer becomes more efficient. This leads to more efficient absorption than at small α (e.g. ≈ 25°).

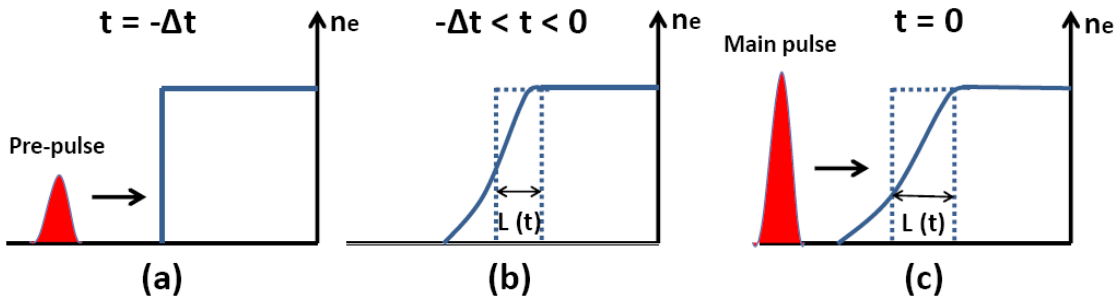

Fig. 2.8 Plasma density profile for different times: (a) arrival of the pre-pulse, (b) between pre- and main pulse, and (c) when the main pulse arrives

In order to establish a well defined plasma scale length in the work described later, the pre-plasma is produced by a laser pre-pulse arriving with a controllable delay before the main laser pulse. In Fig. 2.8, a schematic of this arrangement is presented. The pre-pulse strikes the target surface and ionizes the material. Subsequently the created plasma starts to expand. Assuming a constant expansion velocity $C_s = (ZkT_e/M)^{1/2}$ the plasma scale length L grows linearly in time according to $L \equiv C_s\Delta t$ [171] (T_e is the electron temperature determined by the pre-pulse intensity, Z is the average ionization degree, k is the Boltzmann constant, and M is the ion mass). After a certain time Δt, the main pulse arrives and strikes on this pre-formed plasma with a specific density scale-length L. This scheme offers the possibility of actively manipulating and optimizing the coupling efficiency, "*hot*" electron distribution, and thus the K_α emission. With such a precisely controlled pre-plasma, the optimum conditions for RA discussed in this section can be used to compare with the experimental conditions for which the K_α yield is optimized in the following experiments.

2.5.2 Experimental results

According to the results discussed in the previous section, the experiments in this chapter where performed under “optimum” focusing conditions: The Cu targets were placed exactly in the focus of the lens, while the Ti targets were placed about 900 µm in front of the focus. These configurations lead to intensities on the Cu and Ti targets of 1.6×10^{17} W/cm^2 (focus diameter ~20 µm FWHM) and 9.2×10^{16} W/cm^2 (~25 µm FWHM) for the main pulse and 2.0×10^{14} W/cm^2 (~70 µm FWHM) and 1.1×10^{14} W/cm^2 (~90 µm FWHM) for the pre-pulse, respectively.

The absolute Cu and Ti K_α emission as a function of the main pulse delay at a fixed angle of incidence of 45 ° on targets of different thickness are presented in Fig. 2.9 (a) and Fig. 2.9 (b), respectively. The Cu and Ti K_α emission signal, normalized to the emission measured at negative time delay (5.2×10^8 photons/pulse/sr for 20 µm Cu, 8.2×10^7 photons/pulse/sr for 300 nm Cu, 1.4×10^9 photons/pulse/sr for 20µm Ti and 1.2×10^8 photons/pulse/sr for 300 nm Ti), are presented in Fig. 2.9 (c) and Fig. 2.9 (d), respectively. The K_α yields of the 20 µm targets are six and eleven times larger than for the 300 nm Cu and Ti thin film targets, respectively. This is because at these intensities, the mean-free-path of the "*hot*" electrons is much larger (several µm [121, 130, 172]) than the thickness of the thin film targets. Therefore, in the thin films only a small fraction of all the "*hot*" electrons will create a hole in the K-shell and thus the K_α emission is much less than for a bulk target.

In the presence of an extended pre-plasma created by the pre-pulse, the K_α yield starts to improve. After a certain time delay, the K_α yields reach their maximum value and start to drop with further increasing delay times. A very similar behavior is observed for thick and thin targets as can be seen from Fig. 2.9 (c) and (d). These results show that the pre-plasma which is generated by the controlled pre-pulse permits effective K_α production: At an angle of incidence of 45 ° an “optimum” time delay for K_α production exists on all types of targets. Under these optimum conditions, the K_α production on all targets is improved by almost a factor of 2; whereby the coated targets exhibit slightly better improvements than the thick foil targets. On the other hand, it should be noted that the Bremsstrahlung-background also increases with increasing K_α yield. This is shown in Fig. 2.9 (e) where the measured X-ray signal, integrated in the energy range from 6 - 30 keV for Ti and 10 - 30 keV for Cu, is plotted as a function of pre-pulse - main pulse delay. These energy ranges have been chosen to exclude the above mentioned "many-pixel-events" produced by single K_α photons, since these "many-pixel-events" contribute to the background only below the K_α energy.

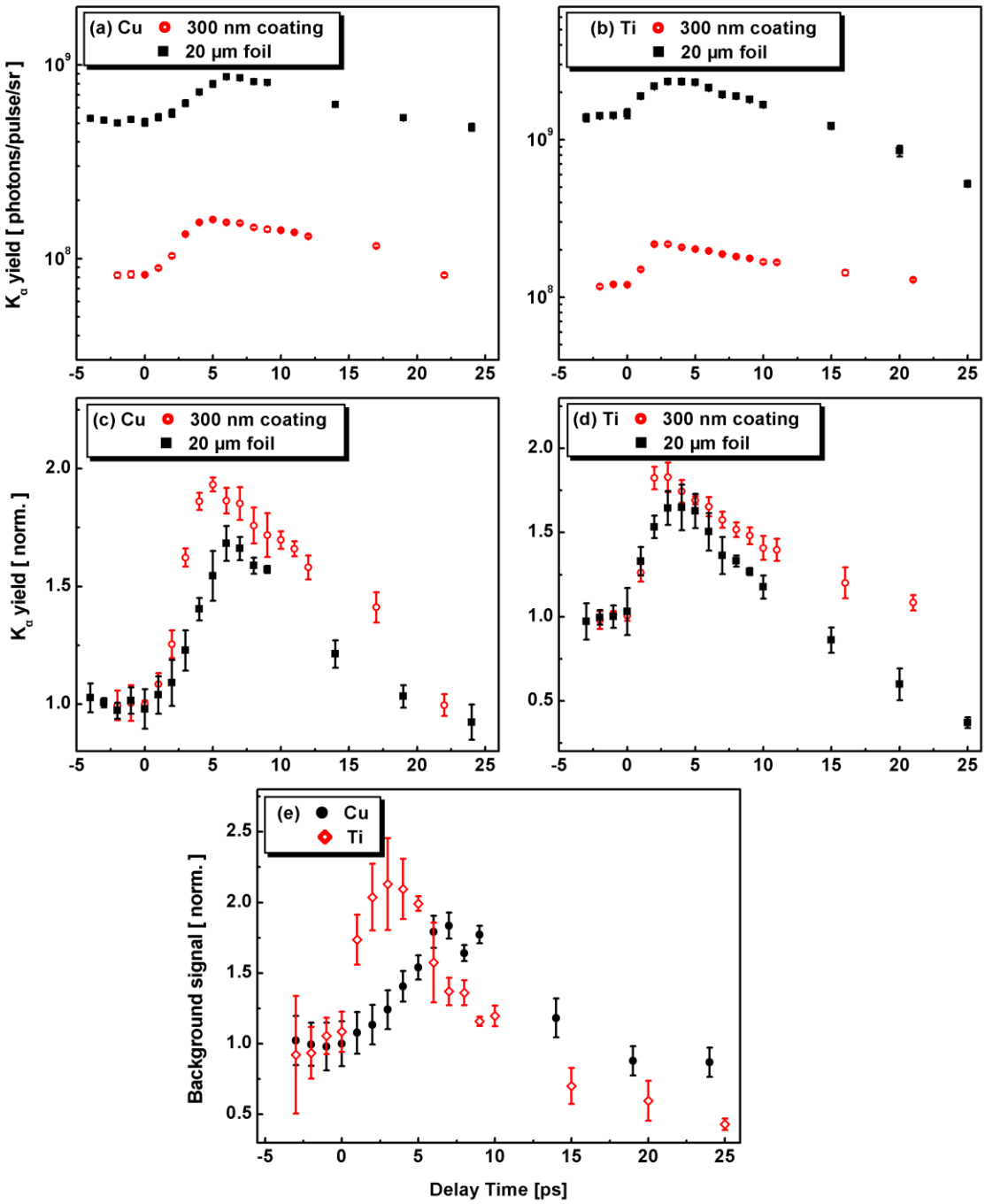

Fig. 2.9 K_α emission as a function of main pulse delay at a fixed angle of incidence of 45 °on targets of different thickness. (a) Cu and (b) Ti. (c) K_α emission of Cu-targets normalized to the emission measured at negative delay time (5.2×10^8 photons/pulse/sr and 8.2×10^7 photons/pulse/sr for d = 20 μm and 300 nm, respectively). (d) K_α emission of Ti-targets normalized to the emission measured at negative delay time (1.4×10^9 photons/pulse/sr and 1.2×10^8 photons/pulse/sr for d = 20 μm and 300 nm, respectively). (e) Hard X-ray background signal as a function of main pulse delay on 20μm targets.

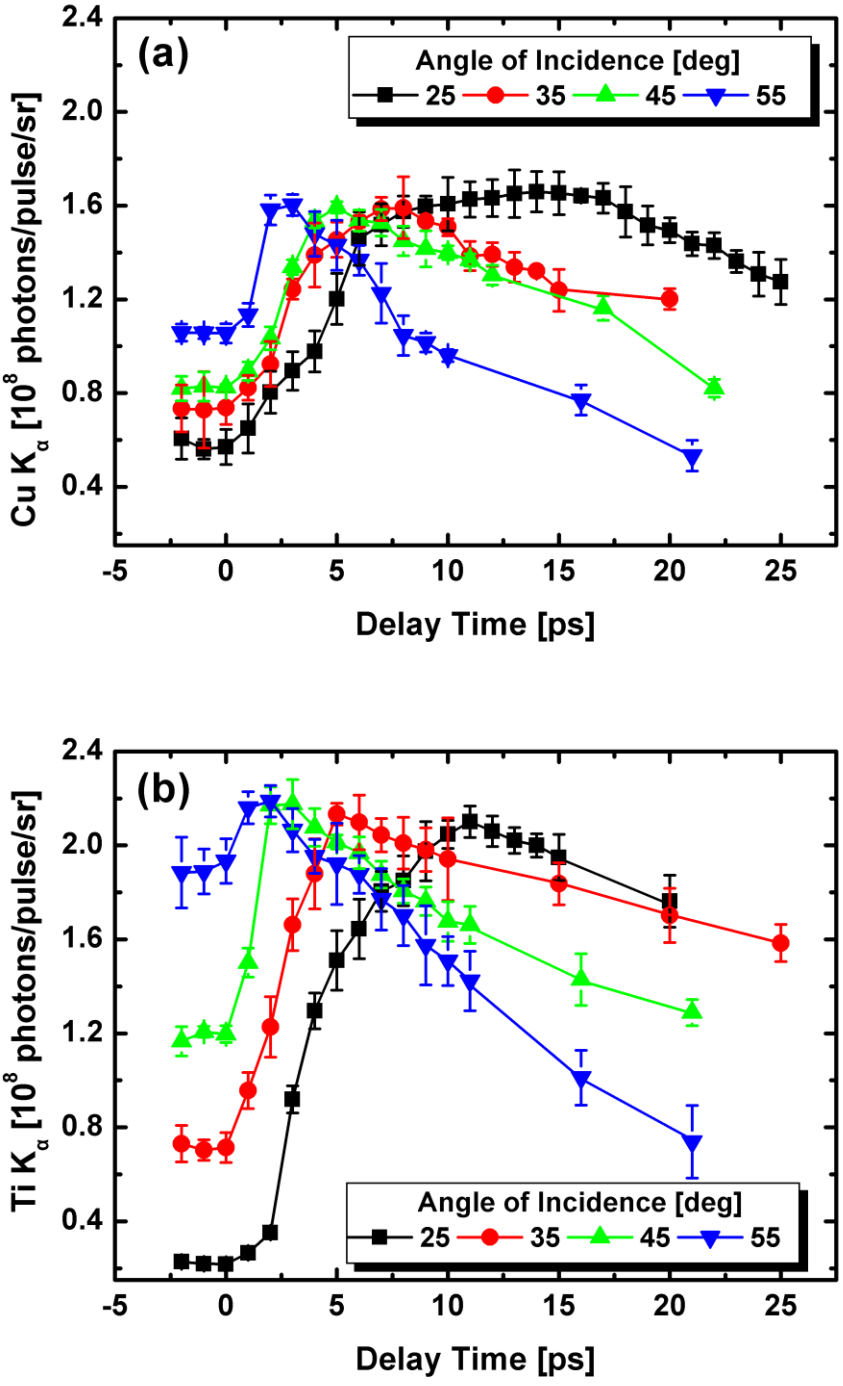

Fig. 2.10 Absolute K_α emission as a function of main pulse delay at different angle of incidence, (a) Cu and (b) Ti. The measured K_α yield at negative or zero delay is the same as obtained without pre-pulse.

In the following, a more systematic study of the influence of a pre-plasma on the K_α production using the 300 nm thin film targets will be presented. With their high (optical) surface quality the uncertain condition for the formation of plasma caused by

surface roughness can be avoided [173]. Based on the very similar behaviour of thin film and bulk targets for the specific conditions of the measurements presented in Fig. 2.9 it is presumed that the results obtained on thin films, which will be discussed below, can be transferred to thick targets (by scaling of the absolute yield). Fig. 2.10 (a) and (b) show the Cu and Ti K_α emission as a function of the main pulse delay at different angles of incidence, respectively. Since the pre-pulse arrives after the main pulse and thus does not play a role at negative delay time, the X-ray yields obtained in this situation will be refer to the situation as ”without pre-pulse” in the later discussions. Introducing a pre-pulse results in an increase of the K_α yield, which is particularly important for small angles of incidence. The K_α yield of both target elements exhibit similar qualitative dependencies on delay time and angle of incidence, though the Ti target shows noticeably larger relative variations.

2.5.3 Discussion

Due to the high contrast ratio laser pulses used in the present experiment, the scale-length in the *absence* of the controlled pre-pulse will be very small. With short scale-lengths, as already discussed in section 2.5.1, the maximum absorption occurs at a large angle of incidence α_{max}, typically 70° or 80° [147, 174, 175]. In such a case the absorption should increase monotonically with the angle of incidence and this is expected to result in an increase of the K_α yield. In Fig. 2.11, the measured absorption of the main pulse and the Cu and Ti K_α yield without pre-pulse from Fig. 2.10 are presented together. The measurement was carried out at constant laser intensity (~1.6×10^{17} W/cm^2 for Cu and ~9.2×10^{16} W/cm^2 for Ti). With a sample thickness of 300 nm, no light is transmitted. Thus the absorption A can be simply determined from a measurement of the reflectivity R, using the two photodiodes shown in Fig. 2.3, as A = 1 - R. As can be seen in Fig. 2.11, the laser absorption does indeed increase with the angle of incidence α for both target elements, so do the K_α yields. These observations are in agreement with the previous works [147, 174, 175].

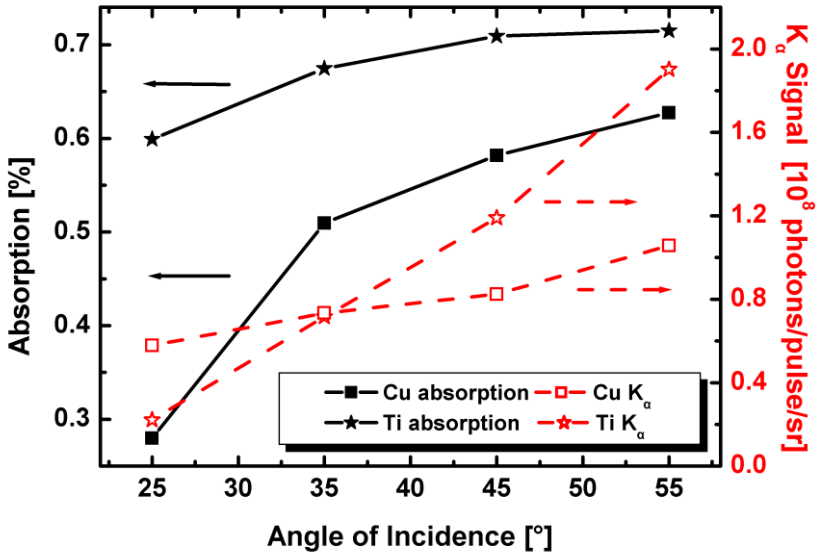

Fig. 2.11 Absorption measurement with main pulse only, measured at constant laser intensity. Scale on left hand side: absorption, scale on right hand side: Cu and Ti K_α yield without pre-pulse (data taken from Fig. 2.10).

With a specific target material the only two variable parameters determining the plasma scale-length L are Δt (delay between the pre-pulse and the main pulse) and T_e (the electron temperature, determined by the pre-pulse intensity) (see section 2.5.1). When the pre-pulse laser intensity is constant, L can be assumed to be approximately proportional to Δt. For this reason, although the absolute values of the scale-length were not measured in the experiment, the relative values from these data can be deduced and be compared to the theoretically estimated values assuming RA as the dominant absorption mechanism. This comparison revealed that the maximum K_α yields correlate with the maximized absorption.

Using $(2\pi L/\lambda)^{2/3}\sin^2\alpha_{max} = 0.6$ as the condition to maximize RA (see section 2.5.1), optimum normalized scale lengths of 0.135, 0.209, 0.392 and 0.980 are calculated for angles of incidence of 55 °, 45 °, 35 °, 25 °, respectively. In Fig. 2.12 (a), the optimum delay times of the pre-pulse for maximum K_α emission in Fig. 2.10 are shown. The maxima appeared at about 3ps, 5ps, 8ps, and 15ps on the Cu target at 55 °, 45 °, 35 °, and 25 °, respectively. For Ti, they were at about 2ps, 3ps, 5ps, and 11ps at 55 °, 45 °, 35 °, and 25 °, respectively. Fig. 2.12 (b) compares the optimum delay time from Fig. 2.12 (a) normalized to the value found at 55 ° with the theoretical estimate of the optimum scale length for RA normalized also to the 55 °-value. Since the intensity

was kept constant (of the pre-pulse as well as of the main pulse) the scale length is proportional to the delay time. The comparison shows that the normalized plasma scale lengths for the best K_α yield from both target materials are in good agreement with the theoretically estimated optimal scale length for RA. The optimum pre-pulse delay increases with decreasing angle of incidence since the optimum plasma scale length for maximum RA increases with decreasing angle of incidence. Fig. 2.12 essentially proves that a maximized absorption corresponds to maximum K_α yield.

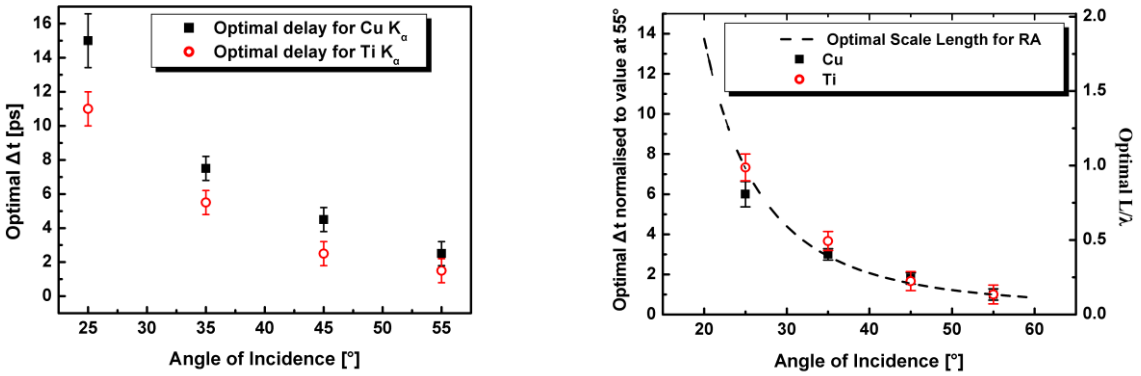

(a) **(b)**

Fig. 2.12 (a) The optimum delay time for the pre-pulse having the maximum K_α yields, extracted from Fig. 2.10. (b) Comparison of experimental data and theoretical estimation. Points are the experimental data in (a) normalized to their respective value at 55 °. Dashed curve is the theoretical calculation of the optimum plasma scale length for resonance absorption, also normalized to 55 °-value. The theoretical curve is calculated from $(2\pi L/\lambda)^{2/3}\sin^2\theta = 0.6$ [147] and its absolute value indicates at Y-axis on the right hand side.

In order to see how the K_α yield develops for different conditions of plasma scale length and angle of incidence, the dependencies of the K_α yield as a function of the angle of incidence for different fixed pre-pulse delay times Δt are deduced from the data of Fig. 2.10 and plotted in Fig. 2.13. For the present experimental conditions, Δt essentially represents the value of the plasma scale length L and thus the data plotted in Fig. 2.13 show the K_α yield as a function of the angle of incidence for different plasma scale lengths. From the previous discussion of Fig 2.12, the plasma scale length at Δt = 15 ps for Cu is estimated as L = 0.82λ, and for Ti L = 1.26λ. For Δt = 0 ps (very short scale length), the K_α yield increases monotonically with α. The maximum K_α yield is beyond 55 °. When the delay Δt (scale length) is increased, the maximum K_α yield shifts to a smaller angle of incidence, e.g. in (a) for Δt = 4 ps the maximum appears at 45 °, for Δt = 7 ps at 35 °. Finally, for Δt = 15 ps, the K_α yield decreases

monotonically with α, indicating the maximum K_α yield is reached at angles of incidence of less than 25 °. As discussed above, the maximum K_α yields correlate with maximum absorption, which in turn shifts to small angles of incidence at large Δt (large plasma scale length). The behavior of the K_α yield proves once again that RA is the dominant absorption mechanism.

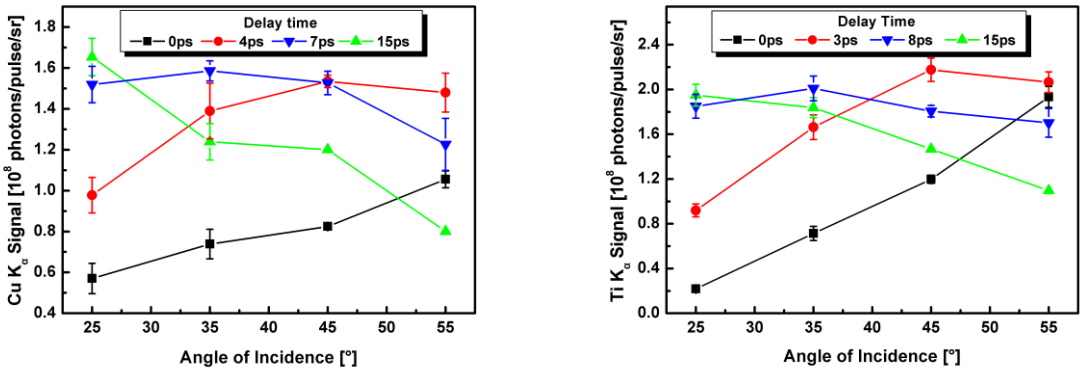

(a) **(b)**

Fig. 2.13 K_α emission as a function of the angle of the incidence at fixed pre-pulse delay. a) Cu at Δt = 0ps, 4ps, 7ps, 15ps. (b) Ti at Δt = 0ps, 3ps, 8ps, 15ps.

Since the goal for this study is to achieve the best K_α yield for time-resolved X-ray diffraction experiments, it is worth to compare the absolute K_α yield for different angles of incidence at optimum scale length and without pre-pulse. As can be seen from Fig. 2.14, without pre-pulse the Cu and Ti K_α yields increase linearly with the angle of incidence. On the contrary, at the optimum delay (optimum plasma scale length) the K_α yield is essentially *independent* of the angle of incidence. Although these observations have not been fully understood, it indicates that the reduced main-pulse-only yield at smaller angles of incidence can be fully compensated (i.e. the yield can be brought back to its maximum value) by an appropriate pre-pulse.

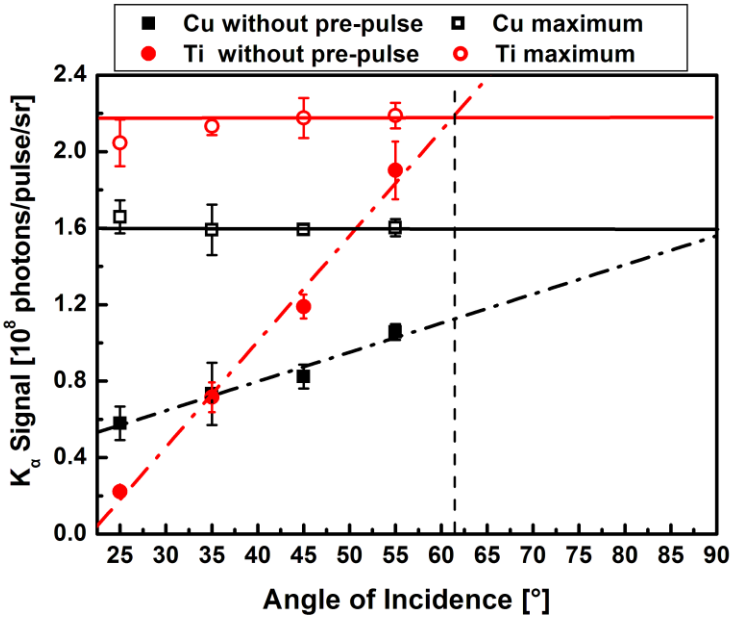

Fig. 2.14 Cu and Ti K_α yield as a function of the angle of incidence at the maximum value and without pre-pulse. The lines are to guide the eye only.

If one extrapolates the linear dependencies measured without pre-pulse to higher angles they reach the angle-independent optimized level at a finite angle of incidence. In the case of Cu this seems to occur at a large angle of incidence near 90°. For Ti this level is already reached at angles of incidence slightly above 60°. This result might arise from the presence of a short scale length pre-plasma caused by the leading edge of the main pulse alone (even for a high contrast laser pulse and in the absence of any further pre-pulse). As discussed for the absorption in Fig. 2.11, it indicates that in the present experiment at this large angle of incidence the plasma scale length generated by the main pulse alone fulfills the condition for optimum RA and thus maximized K_α generation. Hence the optimized K_α yield can be achieved without introducing an artificial pre-pulse – a conclusion which is also supported by PIC simulations (see section 2.6). This would also explain why in many experiments even a relatively poor contrast ratio laser system allows to achieve high K_α yields [130, 148, 152, 156].

Nevertheless, it can be concluded that for a given contrast ratio (given by the laser system) *and* ion mass or a given scale-length in the experiment, one should choose the appropriate angle of incidence α to obtain the maximum K_α yield. Or vice versa: if α is fixed, then one has to adjust L accordingly via pre-pulse control. Such an optimization could be achieved at least in the range of the values of α and L (obtained from Δt) covered by the current experiment, i.e. α ~ 25deg … 55 deg and L/λ ~ 0.1 … 1.

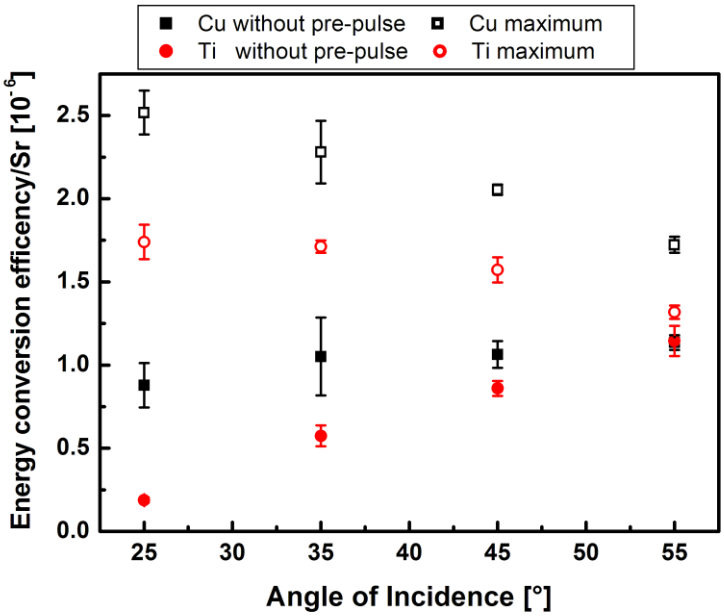

Fig. 2.15 Energy conversion efficiency vs angle of incidence with pre-pulses and without pre-pulses.

An important note concerning the energy conversion efficiency should also be made here. The angular independent optimized K_α yield shown in Fig. 2.14 was obtained by keeping the laser intensity constant. The focused spot size projected onto the sample surface increases with angle of incidence as $1/\cos(\alpha)$. Therefore, at large angle of incidence (e.g. $\alpha = 80°$), one needs more laser pulse energy than at small angles of incidence (e.g. $\alpha = 20°$) for the same amount of produced photons. (In this example a factor $\cos(20°)/\cos(80°) \sim 5$ times more for $\alpha = 80°$ compared to $\alpha = 20°$.) It can be noticed that the energy conversion efficiency from laser pulse into K_α X-rays essentially decreases with the increasing angle of incidence. To clarify this issue more clearly, the energy conversion efficiency has been deduced from Fig. 2.14 using the known laser energies, K_α photon energies and K_α yields and is presented in Fig. 2.15. In principle, the conversion efficiencies obtained here are in line with other experimental results reported in the literature [129, 176].Without the pre-pulse, the conversion efficiency increases with the angle of incidence for both materials. As already discussed in Fig. 2.10, the absorption improves with increasing angle of incidence for the given small pre-plasma scale length that is caused by the main pulse itself and thus leads to a higher K_α yield. On the contrary, at the optimized pre-pulse conditions, the conversion efficiency decreases with increasing angle of incidence as predicted.

2.6 Comparison of the experimental results with simulations

Particle-in-Cell simulations (PIC) are a very powerful and direct numerical tool for modeling laser-plasma interactions [177-179]. In the PIC simulation, the charged particles (electrons, ions, neutrals, molecules, dust particles, etc.) are modeled as individual macro-particles, moving in non-physical grid across the plasma (the "cell" part of the name) using Newton's laws and self-consistently calculated electric fields resulting from external (applied) fields and internal fields from charge distributions. By solving the equations of motion of these particles, the moments of the distribution of the particles such as densities and currents can be obtained simultaneously. The results of PIC simulations presented in this section were preformed by M. Mašek and P. Gibbon, with whom we cooperated.

To obtain a quantitative estimate of the K_α production, this simulation consists of two steps. The energy distribution of "*hot*" electrons generated by the laser-plasma interaction was first determined with PIC simulations. Then the total K_α photon yields produced by fast electrons going inside the target were calculated with a Monte-Carlo method, which is a stochastic technique using random numbers and probability statistics to investigate mathematical or statistical problems [180].

The detailed PIC simulations were performed by using the 1D3V (1 spatial, 3 velocity coordinates) code BOPS (Boosted Oblique Particle Simulation) [127, 131] which can treat oblique incidence. Up to 6000 spatial grids and 500000 electrons and ions are used in the simulation. The laser is p-polarized with fixed intensities as in the experiments. The initial plasma parameters were chosen as close as possible to those expected in the experiment. More details can be found in Ref. [181].

Fig. 2.16 shows the dependence of absorbed energy on the plasma scale-length from the simulation. It is found that the scale length at which absorption becomes maximum decreases with increasing angle of incidence, qualitatively in agreement with the simple RA-picture presented above (Fig. 2.12(b)). Moreover, the scale-length dependencies of the absorption show a general qualitative correlation with the experimental dependencies of the K_α yield with delay time as shown in Fig. 2.10.

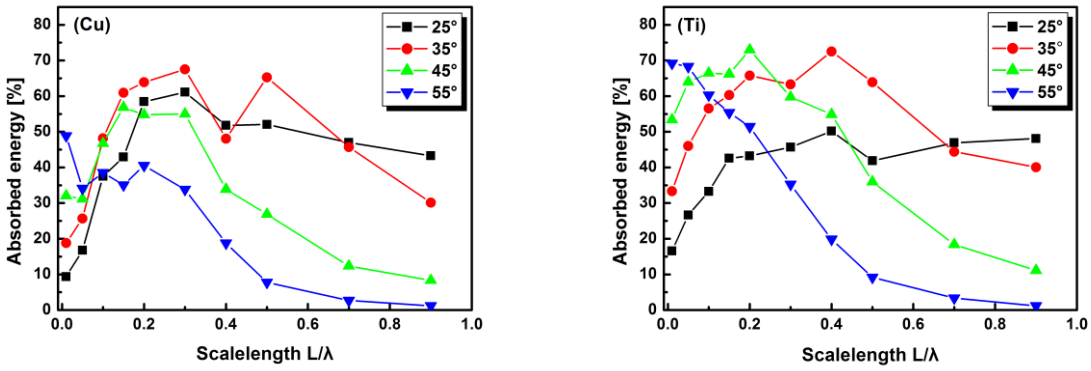

(a) **(b)**

Fig. 2.16 The calculated absorbed energy as a function of the initial plasma density scale length and incidence angle for Cu (a) and Ti (b) targets. Pictures reproduced from Ref. [181].

The total number of K_α photons generated by the "*hot*" electrons during their propagation through the nonexcited solid material underneath the plasma layer was calculated according to a standard cross section model using a method similar to Ref. [129, 182]. The electron distributions obtained from the PIC simulations are split into several monoenergetic beams and transported through the foil which is divided into several cells. Using the relativistic K-shell ionization cross section [124], the number of generated K_α photons is calculated. With the Monte-Carlo method, each electron beam is slowed down via collisions according to the Bethe stopping formula, whereby the stopping power is taken from the NIST database [183] for both materials. Once the electron beam escapes from the rear of the target it is assumed to play no further role in the K_α production, a reasonable assumption because the foils were mounted on low-Z (glass) substrates. The reabsorption of K_α photons is also taken into account. The attenuation coefficient is taken also from the NIST database [184].

Fig. 2.17 shows the dependence of the K_α yield on the initial density scale-length. It is clear that the qualitative behavior from Fig. 2.17 (a) and 2.17 (b) is the same for both materials as in the experiment (Fig. 2.10). The K_α yield reaches its maximum for roughly the same scale-length as the laser absorption, indicating that the K_α yield is largely determined by the absorption efficiency. On the other hand, the absolute values of K_α yields obtained from the PIC simulations are roughly a factor of 3 to 4 times *lower* than the measured values, a discrepancy which could be due in part to the geometrical simplifications in the model. There are also differences in the positions and

values of the K_α maxima, although these are difficult to define precisely for the simulations because of insufficient statistics.

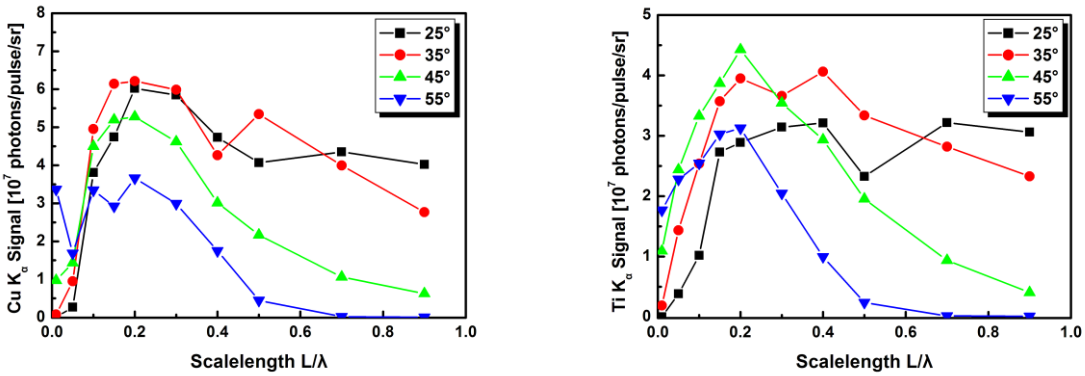

(a) **(b)**

Fig. 2.17 Calculated K_α yield as a function of the intial plasma density scale length and incidence angle for (a) Cu and (b) Ti targets. Pictures reproduced from Ref. [181].

Finally, I would like to add a comment on the time structure of these X-ray pulses predicted from the PIC simulation, although it does not directly relate to this measurement. The result of PIC simulation did show that the duration of these X-ray pulses is in the sub-picosecond region [121], and this prediction has been experimental proved in the following time-resolved experiments.

2.7 Summary

In summary, the emission of K_α-photons of Cu and Ti targets was measured at different laser intensities, sample thickness, angles of incidence and different pre-pulse/pre-plasma conditions. It has been shown that for the given experimental conditions an optimum laser intensity for K_α-production can be reached in the case of Ti. For Cu this optimum intensity appears to be higher than the maximum intensity attainable in the experiment. For constant laser intensity on a steep density gradient plasma, the K_α yield is highest at large angles of incidence. For smaller angles the yield decreases and reaches its lowest value when approaching normal incidence. However, introducing a pre-pulse at appropriate time in advance to the main pulse, the yield can be increased to the same value as at large angle of incidence without a pre-pulse. Therefore the optimized K_α yield is *independent* on the angle of incidence and it can be achieved by proper choice of the pre-pulse timing. Experimentally this was verified for angles between 25 deg to 55 deg.

It was also experimentally found and supported by simulations that the Cu and Ti K_α generation follows the laser absorption, as known for other materials [77, 118, 164, 172, 156, 163, 167]. As expected, resonance absorption (RA) has been proved to be the dominant absorption mechanism in this process and optimization of the K_α production results from a maximized absorption of the laser pulse. For a high contrast laser system, as used in this experiment, controlled pre-pulses provide well defined pre-plasma scale-lengths allowing systematic investigation on the optimization of absorption / K_α production for the other given experimental conditions (material, angle of incidence, pulse energy, intensity). The simulations with these well defined initial parameters show the qualitative agreement with experimental observations and provide insights into the physical process of laser energy absorption, "*hot*" electron generation, electron transport in the material, and the resulting K_α generation.

For practical purposes, the present work indicates that for long plasma density scale lengths created by the leading edge of a low contrast ratio laser system and other experimental conditions (within the range $L/\lambda \sim 0.1\text{-}1.0$), the K_α emission from a laser produced plasma could be optimized by operating the X-ray source at the matched angle of incidence. Experimental arrangements in which an unintentional (or unavoidable) pre-pulse is present could probably be improved simply by using a small angle of incidence instead of the $45\,°$ geometry typical of many setups: The present study indicates that the X-ray emission could be increased by a factor of 2 or 3 in this case, with obvious advantages for many applications of fs-K_α sources, such as time-resolved X-ray diffraction (TRXD). On the other hand, for a high contrast laser system leading where the self generated plasma exhibits a steep density gradient (small scale lenghth), these findings still suggest to use a small angle of incidence and a matched Δt: For the same value of K_α emission, this requires less energy to achieve the same on-target intensity as with a large angle of incidence and subsequently leads to a better energy conversion efficiency.

In the following chapter, these results are applied to improve the laser-plasma based X-ray source for the TRXD experiments.

3. Improvements of the modular setup for time-resolved X-ray diffraction experiments

As it has been discussed in detail in the previous chapter, focused laser intensities in the range of 10^{17} - 10^{18} W/cm^2 are required to efficiently generate X-rays in the multi-keV range. If the irradiated target is surrounded by an atmosphere, non-linear effects (e.g. self-phase-modulation, self-focusing [185]) and plasma formation (breakdown) in the atmosphere will severely deteriorate the spatial intensity distribution of the focused femtosecond pulse and the required on-target intensities cannot be reached. Therefore, the X-ray target has to be placed in vacuum. Two different set-ups to perform time-resolved X-ray diffraction are currently used at the University of Duisburg-Essen. One scheme uses a large vacuum chamber to place not only the X-ray target but the whole setup (including X-ray optics, samples and detectors) under vacuum [70, 140]. This scheme avoids absorption losses of the generated X-rays in air (which is more critical for lower energy radiation like Ti K_α - 4.51 keV), but it poses some geometrical restrictions due to its limited size. Moreover, operation of the setup is relatively complicated since most of the components in the chamber require remote control.

To overcome some of these drawbacks, a second scheme for time-resolved X-ray diffraction experiments had been designed and built up mainly by Dr. Matthieu Nicoul [186] and since then it has been continually further developed. This setup has a modular design and only the X-ray source/target itself is operated under vacuum, and all the other experimental components are placed in air. This gives a lot of advantages, such as more space for experimental components and convenience in adjusting them. It was the aim of the work described in this chapter to improve the existing setup to allow for time-resolved Bragg-diffraction experiments with increased accuracy (see chapter 5) and to enable new experimental schemes that had not been possible before (i.e. time-resolved Debey-Scherrer-diffraction; see chapter 6). In the first part of this chapter, the fundamental components of the previously existing setup are briefly described. In the

second part, I present and discuss the implemented improvements including hardware, software and methodology. Finally, a summary for this chapter is given.

3.1 The fundamental components of the current setup

A scheme of the current setup is shown in Fig. 3.1. The fundamental components (labeled with black letters on Fig. 3.1) had already been described in detail in Ref. [186]. In order to provide the necessary information to the reader, the important components will be briefly pointed out in this section. The implemented improvements/additions to this setup are also represented on Fig. 3.1 (labeled with blue letters) and they will be discussed in the next section 3.2.

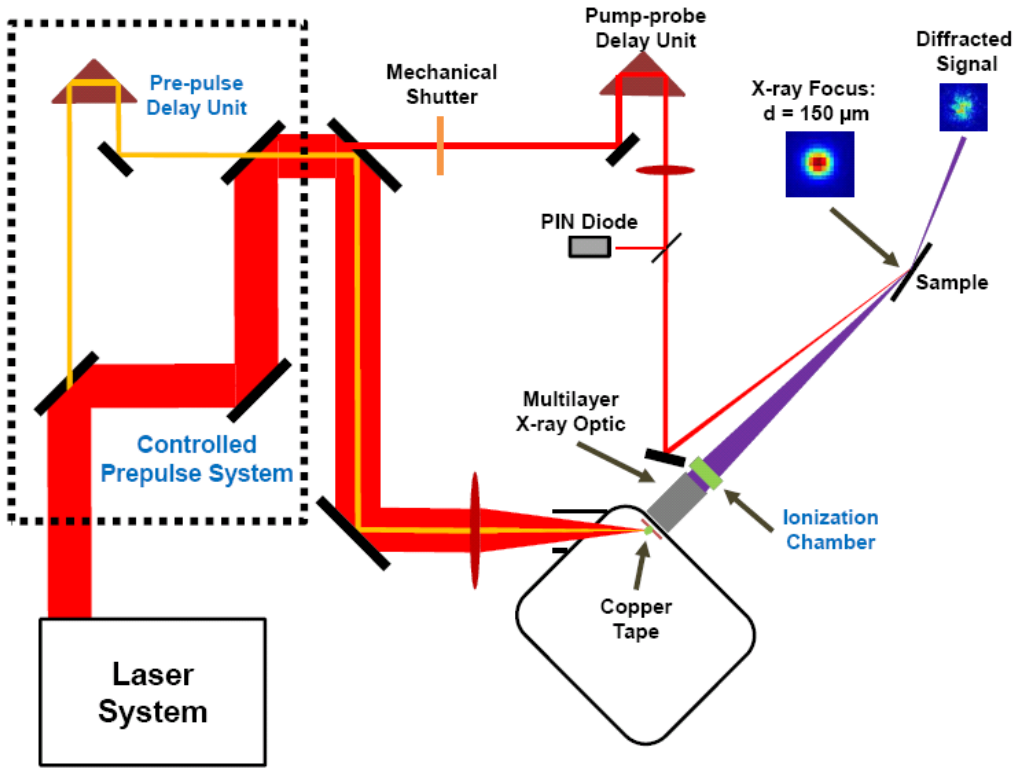

Fig. 3.1 Scheme of the current modular setup for time-resolved X-ray diffraction experiments. The elements labeled with black letters are components of the previously existing setup and the ones labeled with blue letters are components implemented during my PhD work.

The CPA Ti:sapphire laser system, described in chapter 2, delivers 150 fs laser pulses at a wavelength of 800 nm with an energy of 120 mJ at a repetition rate of 10 Hz. The laser beam (the red optical path in Fig. 3.1) is split into two parts by a mirror with a small off-center hole (7mm in diameter). The transmitted part serves as the

optical *pump* beam to excite the sample under study, while the reflected part is focused by a lens of 300 mm focal length onto a Cu-tape target with an incident angle of 45 °(p-pol.), to produce the Cu K_α (8.05 keV) *probe* pulse.

For the reasons mentioned in the introduction of this chapter the Cu-target is placed inside a compact vacuum chamber (size 24×30×30 cm^3), which includes connectors for the vacuum pump, a pressure gauge, and electrical feedthroughs as shown in Fig. 3.2. For mechanical and radiation safety reasons, this chamber is made of stainless steel with a wall thickness of 15 mm. Additionally a 2 mm lead cover was added inside the chamber to enhance security and to reduce the level of background radiation that may reach the detector. The working pressure of the chamber is 0.1 mbar.

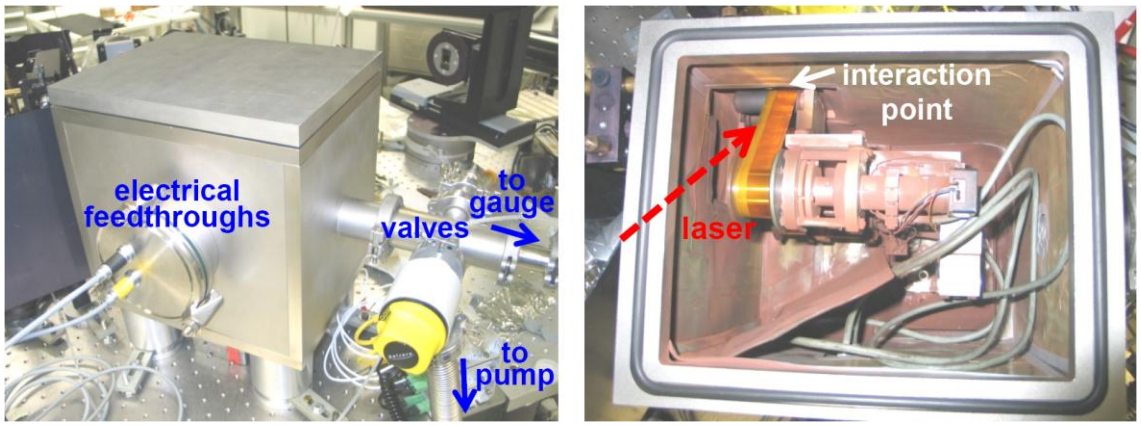

(a) **(b)**

Fig. 3.2 Overview of chamber. (a) outside and (b) band target inside the chamber.

The target consists of a 10 µm thick Cu tape mounted on a motorized spooling system, which works similarly to an audiocassette recorder (Fig. 3.3 (a)). The pulling speed is approximately 8 mm/s (i.e. 800 µm motion between two consecutive laser pulses) to ensure that a fresh surface area is provided for each laser pulse. The tape shifts vertically to its pulling direction by about 0.8 mm when the pulling direction is (automatically) changed. One set of band (25 mm wide and 15 m long) can provide more than 12 hours experiment time. In order to minimize the deposition of ablated material, in particular at the small hole where the X-rays can leave the chamber [187], a 8 µm Kapton foil has been rolled together with the Cu tape before mounting it to the spooling system. The Kapton foil runs simultaneously with the tape to pick up the debris which is predominantly ejected at the back-side of the tape normal to its surface [187]. Close to the laser-target interaction point it is mechanically separated from the Cu tape by about 2 mm (see Fig. 3.3 (b)).

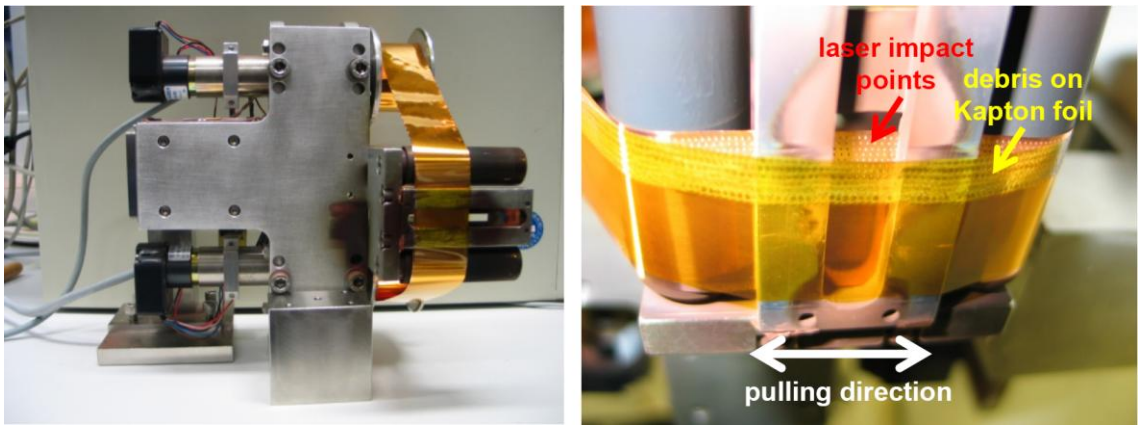

(a) **(b)**

Fig. 3.3 (a) Photo of band target. (b) Kapton foil used for reducing material deposition.

Using a pin-hole camera, the size of the X-ray source on the tape target was found to be similar to the spot size of the focused laser beam, i.e. ~25 µm [187]. The Cu K_α emission is close to 5×10^9 photons/pulse in 4π solid angle *without pre-pulse* and 1×10^{10} photons/pulse *with an optimized pre-pulse* (see section 3.2.1). Since the X-ray emission is into the full solid angle, a multilayer X-ray optic with *Montel-Helios* geometry [188] is used to collect the radiation and to refocus it onto the sample under investigation. The multilayer X-ray optic reflects both, the Cu $K_{\alpha1}$ and $K_{\alpha2}$ emission lines, but suppresses other spectral components (i.e. K_β). More details on the working principle and the specifications of this mirror can be found in Appendix A.

The focused X-ray beam was characterized at different positions of the beam path through four relevant parameters [186]: the beam profile directly after the multilayer optic, the total number of reflected photons, the convergence of the beam, and the size of focus spot. A direct detection CCD camera was used to measure the first three relevant parameters of the X-ray beam, since it allows a rather accurate estimation of the absolute detected X-ray signal (e.g. number of diffracted photons per pulse). A X-ray beam profile taken at 4 centimeters after reflection on the multilayer optic is shown in Fig. 3.4 (a). Since the X-ray emission from the plasma is isotropic (i.e. homogeneous illumination of the mirror), the intensity distribution measured at such a short distance after the optic gives direct information on the spatial reflection properties of the two multilayer mirrors. The image in Fig. 3.4 (a) demonstrates the uniformity of the reflectivity over the mirror surfaces. Due to the mounting configuration of the multilayer mirrors inside the housing, the beam shape is a 45 ° rotated square [Appendix A]. The convergence angle of the beam was measured to be approximately 0.23 °, which

corresponds to the specifications of the manufacturer (0.24 °). Using the known sensitivity of the direct detection CCD camera [186], the Cu K_α flux in the focused beam can be determined from images like the one shown in Fig. 3.4 (a). With an *optimized pre-pulse* a typical flux of 1.3×10^5 photons/pulse was obtained. The intensity distribution at the focus spot was measured with an indirect, phosphor based detector ("Gemstar") [186]. A typical image, with horizontal and vertical cross sections, is shown in Fig. 3.4 (b). The measured FWHM of the focus spot is 150 µm in horizontal and 127 µm in vertical. With the given source size of approximately 25 µm and the 5x magnification of the multilayer optics this is close to the expected value.

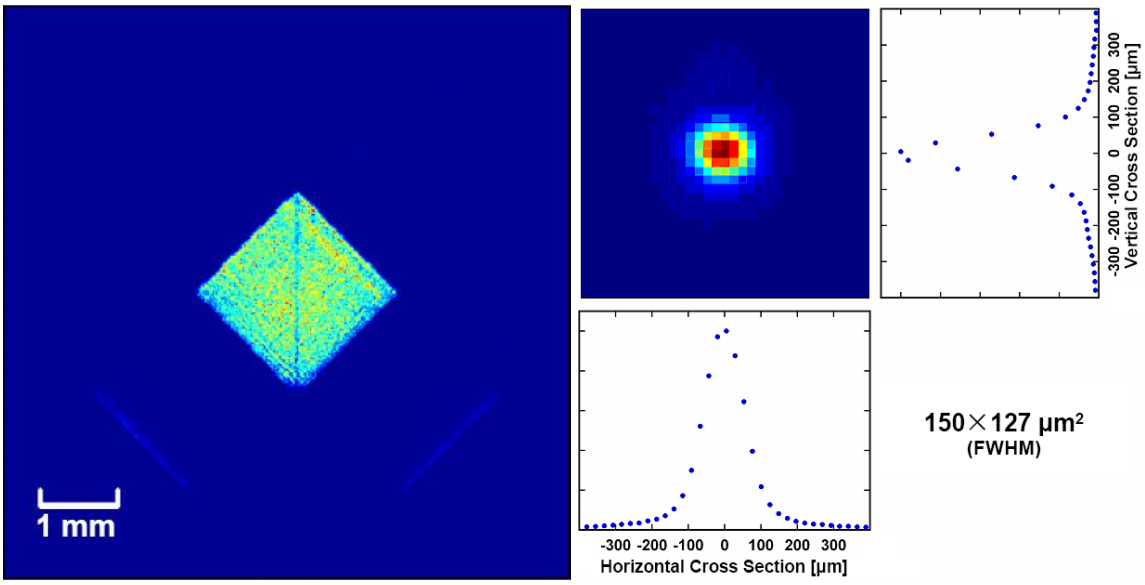

Fig. 3.4 (a) Topography of Cu K_α beam observed with the direct detection CCD camera 4 cm after reflection on multilayer mirror. (b) Intensity distribution of Cu K_α emission at the focal point of the multilayer optic, obtained with the phosphor based detector. Pictures reproduced from Ref. [186].

Since most of the experimental components of the modular setup are placed in air, they are easily accessible and can be conveniently manipulated. In order to minimize losses by absorption of the Cu K_α-radiation in air [189], the optics housing is purged with He, and He-purged beam-tubes were installed in the X-ray beam path. Although the X-ray beam path cannot be covered completely, more than 90% of the radiation collected and reflected by the X-ray optic is delivered to the sample.

The samples are mounted on a motorized x-y-θ stage to adjust the Bragg-angle (θ) and the beam position on the sample (x-y). The diffraction signals have been recorded so far by two different X-ray sensitive area detectors. The first detector is a direct

detection CCD-camera (type PI-MTE: 1300B) which has also been used for the measurements discussed in chapter 2. As it has been explained before, due to the strict relation between the X-ray photon energy and the generated charge, this detector can be used as a spectrometer (see chapter 2) and allows determination of the absolute X-ray signal with rather high accuracy (single photon sensitivity). The low quantum efficiency (18 %) and the slow readout time are its main drawbacks. The second area detector uses "indirect" detection: A phosphor screen converts incoming X-ray photons into visible photons. The optical signal is amplified by an image-intensifier and then detected by a normal CCD. Although this system allows single photon detection at high gain of the intensifier, there is no well-defined relation between the detected signal and the X-ray photon energy. On the other hand, this detector has a high quantum efficiency (85% for Cu K_α radiation [186].) and high read-out rate (up to 10 Hz), so that an image can be recorded for each single X-ray pulse. A more detailed discussion of these detectors and their specific advantages and drawbacks can be found in Ref. [186] as well as in Appendix B.

The energy of the *pump* beam used to excite the sample is adjusted with a half-wave-plate in conjunction with a thin film polarizer and monitored with a PIN diode. A motorized translation stage with a retro-reflector allows varying the delay between the optical pump and the X-ray probe beam. The p-polarized pump beam is focused with a lens of 1 meter focal length onto the sample surface. The angle between laser pump and x-ray probe beam is set to be as small as possible, i.e. approximately 10 °. In order to ensure that the measured diffraction signals represent the response of an almost homogeneously excited region, the diameter of the pump beam is chosen to be at least 3 times larger than the X-ray spot size. Since the available amount of energy in the pump-path (about 1 mJ per pulse) is more than sufficient for the experiments discussed in this thesis, a diaphragm has been used to adjust the pump beam spot size. A removable mirror which can be inserted in the beam path directs the beam to a CCD camera positioned at a position equivalent to the distance to the sample to monitor the size and the shape of the focused beam.

3.2 Improvements of the modular setup

During my thesis work, several improvements of the setup have been implemented in order to (i) optimize/increase the X-ray flux of the plasma source, (ii) improve the measurement sensitivity/accuracy, and (iii) automatize and speed up the experimental

procedures. This section describes in detail the necessary steps and modifications which were essential to achieve the results of the time-resolved diffraction experiments discussed in the following chapters, in particular the results of the phonon softening obtained on photo-excited Bismuth (Chapter 5).

3.2.1 Controlled pre-pulse to enhance the X-ray production

In chapter 2 it has been discussed in detail that a controlled pre-pulse with suitable delay can be used to improve the X-ray production. Based on this result a pre-pulse unit (beam splitter and combiner, delay stage; see the black-dotted box in Fig. 3.1) has been added to the modular setup. The main pulse energy is 110 mJ and the pre-pulse energy is 1.5 mJ, which results in intensities at the focus of the lens of 1.6×10^{17} W/cm^2 for the main pulse and 2.0×10^{14} W/cm^2 for the pre-pulse, respectively. With a pre-pulse arriving 5 ps before the main pulse, the X-ray production of the modular setup has been improved by about a factor of 2, which leads to more than 10^5 Cu K_α photons/pulse collected and focused by the X-ray mirror on the sample under normal experimental conditions. The positive effect of the pre-pulse was also briefly underlined and presented in Dr. Nicoul's thesis.

3.2.2 Avalanche photodiode (APD)

It was pointed out by Nicoul [186] that the modular setup with the magnifying/collimating *Montel*-optic is most appropriate for experiments in which the shape or angular position of the rocking curve of the excited sample does not change but only the total diffraction efficiency (i.e. due to structure factor changes). Under these conditions it is not necessary to use a detector with 2D resolution, and therefore, a single-channel detector is sufficient. Since the diffraction efficiency of the thin-film samples typically used in the time-resolved experiments is low (10^{-3}-10^{-4}, resulting in diffraction signals of 10 - 100 photons/pulse), a detector with high sensitivity down to the single-photon level is required. X-ray sensitive avalanche photodiodes (APD) fulfill these requirements. An APD is a photodiode with internal gain obtained by applying a high reverse bias voltage to the photodiode which creates an intense electric field inside its volume. It combines the benefits of a photomultiplier tube (gain) and conventional photodiodes (high quantum efficiency).

For the modular setup a large area (10 mm in diameter) Silicon APD was chosen (its technical data are given in Appendix B). Using the direct detection CCD for calibration the quantum efficiency of the APD for Cu K_α radiation was measured to (36 ± 7) %, in agreement with previously published data [190, 191]. This detector can be easily operated at a repetition rate of 10 Hz and with more convenience (compact size, no need for water cooling) as compared to the phosphor based area detector. To digitize the detected X-ray signal, a gated, charge-integrating analogue-to-digital converter (ADC) [192] is used. In order to match the APD-output to the input specifications of the ADC, a pulse shaper/amplifier is added directly to the APD.

The APD/ADC-combination was calibrated for the detection of Cu K_α radiation by reducing the incident X-ray signal to the few-photons-per-pulse-level (0 to 6) and analyzing the signal value distribution (histogram) of a large number of pulses (typically a few thousand) for different bias voltages. Results are shown in Fig. 3.5 (a). The signal value distributions exhibit a multi-peak structure as it is expected for a Si-detector with its rather well defined relation between the charge generated by a single X-ray photon and the photon energy (e. g. one Cu K_α photon produces 3.66×10^{-4} pCb). A multi-peak fit was applied to separate the individual peaks and to determine in particular the position of each peak (marked in the figures). The first left peak corresponds to the dark current background (no photon detected, proven by blocking the X-rays) and the second, third, fourth … peaks are correspond to one, two, three … detected photons, respectively. By plotting the peak position as a function of photon number in Fig. 3.5 (b) and fitting the result by a linear function (Y = m + n X), the corresponding ADC output (given in counts) for the background signal (parameter m) and for a single Cu K_α photon (parameter n) can be determined for different bias voltages. The result is shown in Fig. 3.5 (c). The ADC output per Cu K_α photon (black squares) increases rapidly with bias voltage reflecting the corresponding increase of the APD-gain. It has to be noted that the dark current is also amplified with increasing bias voltage, underlined by the increase of the background signal (red circles).

Since the X-ray-to-charge conversion is known as well as the amplification of the amplifier (11x) and the sensitivity of the ADC (32 counts per pCb) this APD-gain can also be deduced from the information above. The result is plotted in Fig. 3.6 as a function of bias voltage, together with results of optical measurements (see below) and data provided by the manufacturer. All data are in a good agreement and the maximum gain of 10^3 is proven to be achievable with this device.

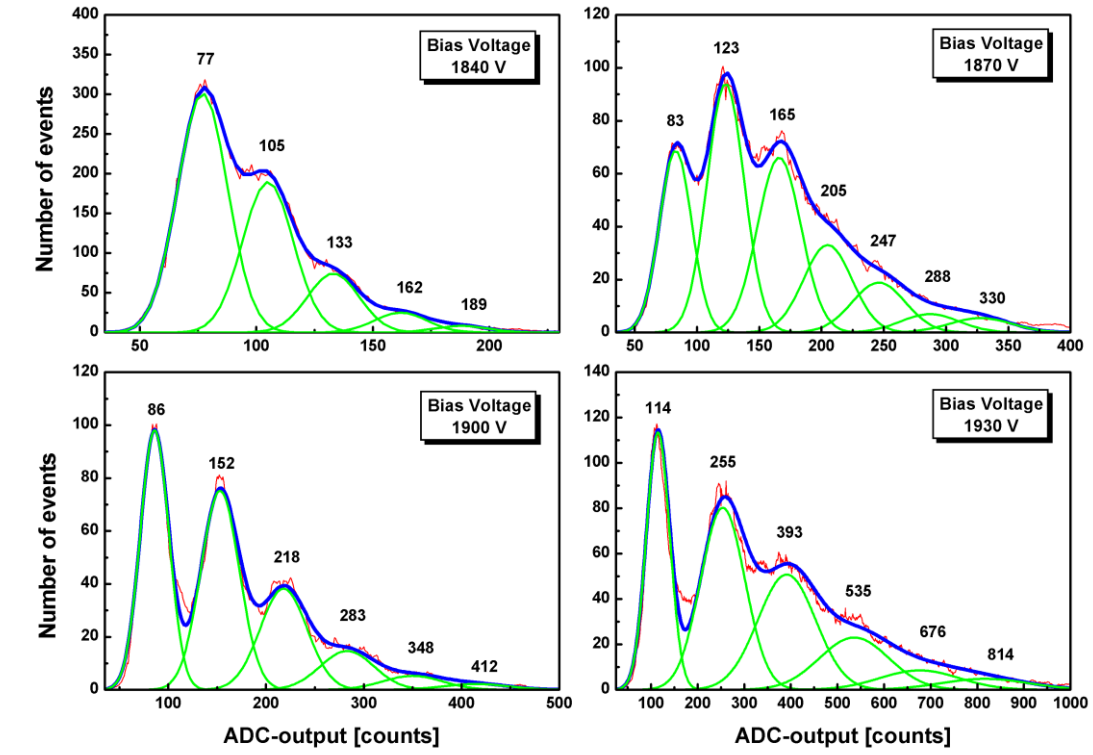

(a)

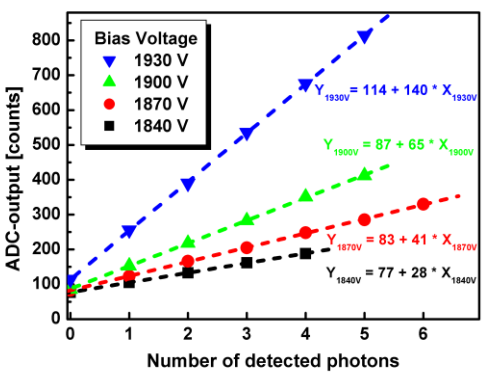

(b)

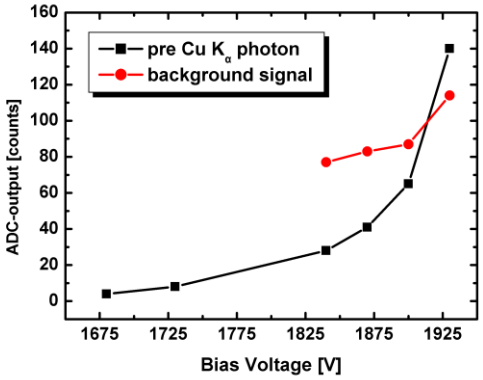

(c)

Fig. 3.5 (a) The signal value distributions (histograms) measured with the APD at the few-photons-per-pulse-level at different bias voltages. The blue curves are the total multi-peak fits and the green peak profiles are the separated individual peaks. The peak positions are indicated on the top of each peak. (b) The values of peak positions in (a) as a function of the number of detected photons. With the linear fitting function (Y = m + n X), the background signals and corresponding ADC outputs (given in counts) pre Cu K_α photon can be determined by the fitting parameter m and n, respectively. (c) The corresponding ADC outputs per Cu K_α photon (black square points) and the background signals (red circle points) at different bias voltages.

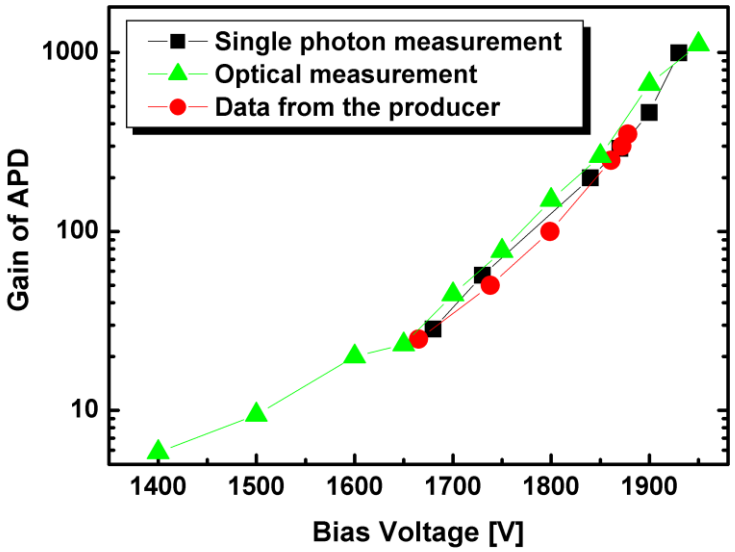

Fig. 3.6 Comparison of the gain of APD from three measurements.

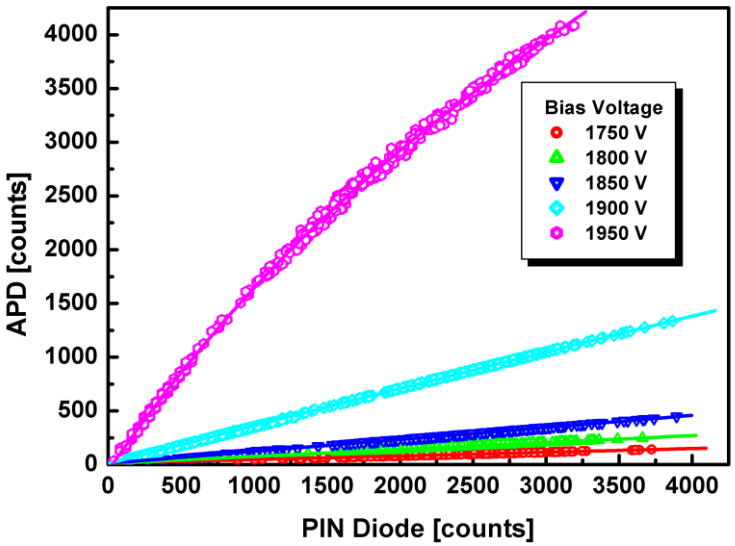

Fig. 3.7 APD signal as a function of PIN diode signal with different operating voltages.

Another important information concerns the question whether the (electric) output signal is proportional to the (X-ray or light) input signal (linearity). The linearity of the APD was checked by measuring an optical input with the APD at different bias voltages and a regular Silicon PIN-diode which was known to be linear over the used range of incident optical power. In Fig. 3.7, the APD-signal is plotted as a function of the PIN diode signal for different APD bias voltages. It turns out that the response of the APD is linear for an ADC-output up to about 1000 counts. For higher signal levels the response becomes nonlinear. Since the APD and the assembled electronic

shaper/amplifier were not tested separately, the source of the nonlinearity cannot be determined at this point. In the time-resolved diffraction experiments the nonlinearity of the APD needs to be taken into account and corrected.

3.2.3 Ionization chamber detector (ICD)

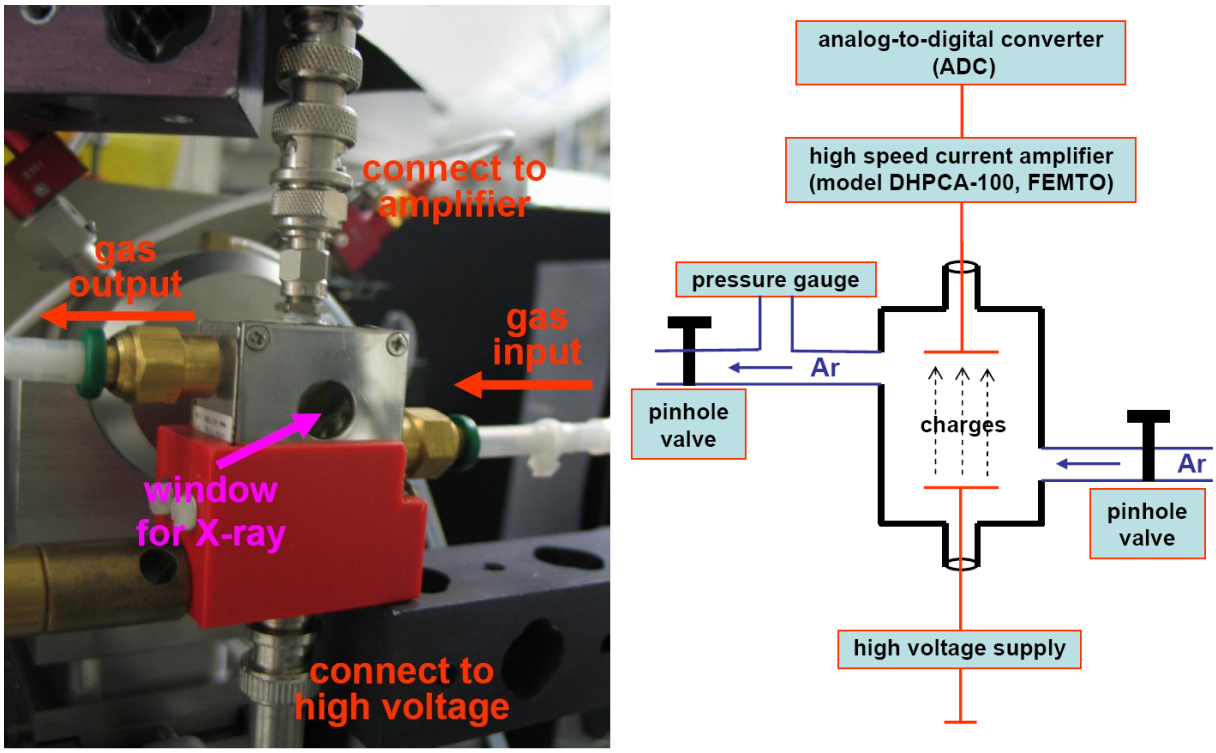

(a) **(b)**

Fig. 3.8 (a) Photo of the ionization chamber detector and (b) its working scheme.

In order to normalize the diffraction signals and to determine the changes in the X-ray diffraction efficiency of an optically excited sample with high accuracy it is necessary to measure also the (relative) incident X-ray flux for each pulse. For this purpose a small ionization chamber detector has been placed behind the X-ray multilayer optic. A photo of the installed chamber and its working scheme is shown in Fig. 3.8. Part of the Cu K_α radiation reflected by the optic is absorbed and ionizes the Ar-gas with which the cell is filled. The Ar-pressure is around one atmosphere. At 8 keV a transmission of 72% is measured and it agrees with the expected transmission value of 1.6 cm Ar at 1 atm plus 16 µm of Kapton foil used as cell windows [189]. To collect the charge generated by ionization a high bias voltage is applied (2000 kV). A high speed current amplifier (type DHPCA-100, FEMTO) with a gain of 10^5 is used to

match the output signal of the ionization chamber to the input of the gated charge-integrating ADC (same as used for recording the APD-signals).

In order to characterize the ionization chamber detector its linearity was measured using the phosphor based area detector, which can be regarded as a linear detector. The result of this measurement shown in Fig. 3.9 (each data point corresponds to an acquisition time of 30 sec.) clearly shows the linear response of the ionization chamber.

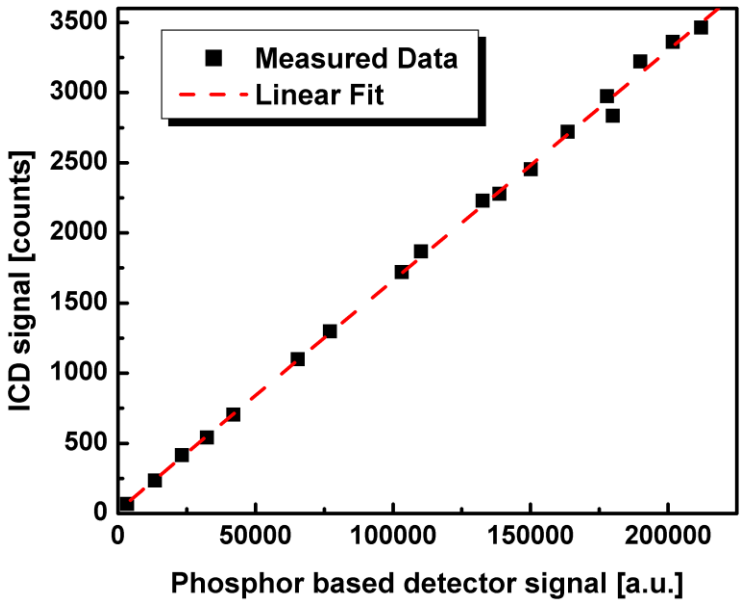

Fig. 3.9 Calibration between ionization chamber detector and phosphor based detector. Red dashed line is a linear fit of the measured data.

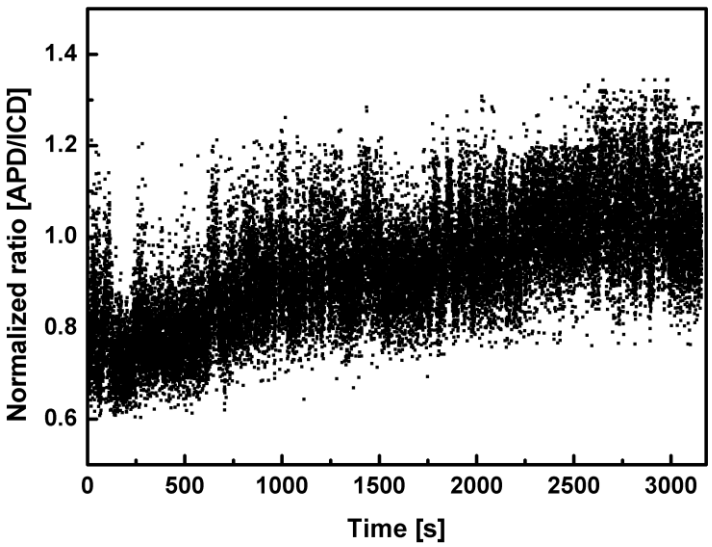

Fig. 3.10 Long term drift of the normalized ratio.

It should be noted that the output signal of the ionization chamber is surprisingly very sensitive to changes of the Ar-pressure (approx. 30% change of signal for <1% change of pressure). Therefore, the pressure inside the chamber needs to be stabilized during the whole measurement. For this purpose a pressure control system, consisting of two pinhole valves and a pressure gauge, was implemented (see Fig. 3.8). It allows stabilizing the pressure inside the chamber to about ±0.1 mbar (relative to the external pressure). Despite stabilizing the pressure in the ICD we observed long term drifts of the ICD-signal during the diffraction measurements. As an example, the ratio between the APD and ICD signals from one representative measurement, recorded over about one hour, is presented in Fig. 3.10. The large pulse-to-pulse variations of the ratio are caused by the counting statistics limited fluctuations of the APD-signal (only a few photons per pulse are detected in this particular measurement). Additionally the ratio which should be constant on average changes slowly with time. So far no clear explanation has been found for this effect. These drifts can severely limit the achievable accuracy in a time-resolved experiment when for example the different pump-probe delays are sequentially measured during an experimental run. The issue has been solved by applying a “fast” delay scanning technique in the experiments which will be discussed in section 3.2.6.2.

3.2.4 Experiment control program

The modular setup is entirely controlled by a software program developed using the LabVIEW environment. The functions of this program include control and monitoring of the different elements and detectors in the setup as well as data recording and pre-processing. All functions can be accessed from one interface (shown in Fig. 3.11), which has been geometrically divided into two parts.

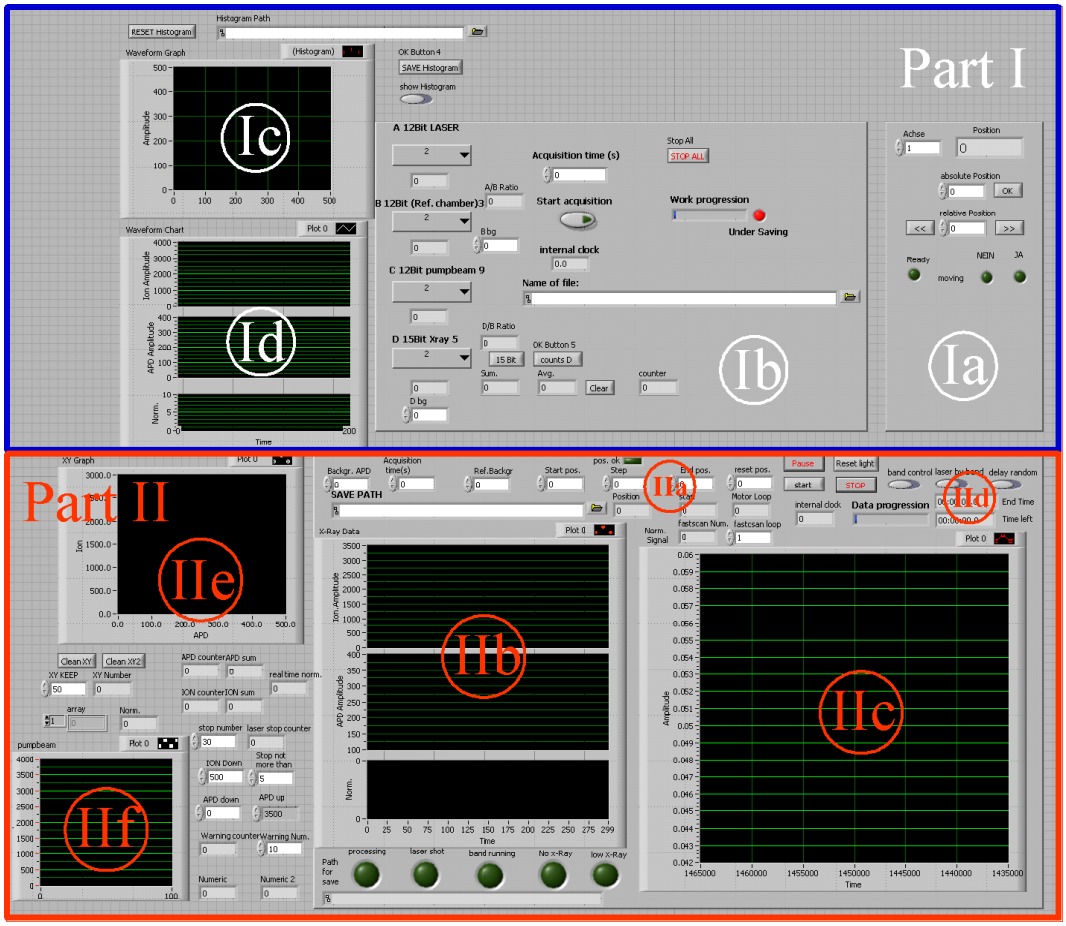

Fig. 3.11 Interface of the experiment control program.

The upper part (part I) is used to prepare an experiment and to perform some simple test measurements, e.g. checking signal levels, the background signals of the detectors, etc.. Frame (Ia) is a control panel for the pump-probe delay unit. In frame (Ib), the detected signals from individual detectors (i.e. PIN diodes, APD, ICD) can be selected and displayed. The received data can be recorded into files. Frame (Ic) is a waveform graph to show the histogram of the signal of the detector selected in frame (Ib). Frame (Id) displays the real time trace for the selected detector.

The lower part (part II) is used for the time-resolved diffraction experiments. In region (IIa), one can enter the relevant measurement settings, e.g. background signal of the different detectors, acquisition time for the individual measurement points, delay range, delay steps, and saving folder. Frame (IIb) shows the real time traces of the measurement, and the ratio APD/ICD. The five indicators at the bottom of this frame indicate the status of the measurement system. Frame (IIc) displays a constantly updated preliminary analysis (i.e. ratio APD/ICD vs. delay time) of the measured data. In region (IId), several switches allow to change between different operation modes of the tape target, the laser triggering and the delay unit (e.g. "fast" scanning, see below).

Frame (IIe) displays the correlation between APD and ICD and Frame (IIf) displays the pump beam energy.

part I	To prepare the experiments and to perform some simple test measurements.
Frame (Ia)	Control of the pump-probe time delay
Frame (Ib)	Selection and value display of the signals from individual detectors
Frame (Ic)	Display of the signal value distributions of the selected detectors.
Frame (Id)	Display of real time traces for the selected detectors.
part II	To perform the time-resolved diffraction experiments
Frame (IIa)	Input of the relevant measurement settings.
Frame (IIb)	Display of real time traces of APD, ICD, and their ratio.
Frame (IIc)	Display of a preliminary analysis of the measured data.
Frame (IId)	Control of tape motion and “fast” scanning.
Frame (IIe)	Display of APD-signal vs. ICD-signal.
Frame (IIf)	Display of the pump beam energy.

Table 3.1 The functions of the individual areas in the user interface of the experiment control program.

For a better overview, the functions described above are briefly summarized in Table 3.1. This program has been proven very useful during the performed experiments. However, further improvements are possible. For example, integration of control functions for the sample holder might be required to allow a synchronized motion of the sample during data acquisition (e.g. for experiments where the sample is irreversibly damaged/modified by a single laser pulse).

3.2.5 Spatial and temporal overlap adjustments with APD

A very important and non-trivial part of performing a time-resolved diffraction experiment is to find spatial and temporal overlap between the (invisible) X-ray probe beam and the laser pump beam. To find spatial overlap, a similar procedure is applied as described in Ref. [186]. The sample is moved vertically and horizontally with the translation stage in order to scan its border through the X-ray beam. Since the sample surface is monitored by a camera on a video screen, the disappearance of the X-ray diffraction signal allows to localize the X-ray beam position by marking the sample border in horizontal and vertical direction on the screen. Then the optical beam can be easily adjusted to overlap with X-ray beam on the marked position. The spatial overlap needs to be checked before every measurement.

Once the spatial overlap is established, the temporal overlap is adjusted by exciting the sample with the laser and monitoring changes of the diffraction signal while scanning the delay stage. Two examples are presented in Fig. 3.12. which show

the relative decrease in the diffraction signal upon laser excitation on thin films of Au (333)-reflection (a) and Bi (111)-reflection (b) While the different physical processes responsible for the observed signal changes will not be discussed here (see chapter 4 and 5) the time-traces allow to determine delay zero (temporal overlap). The accuracy depends obviously on the speed of the induced changes and can reach the sub-picoseconds level if the changes are fast (i.e. Bi). Moreover, it should be emphasized that using the APD and the new experiment control program allows to obtain such results in just a few minutes. Without the implemented improvement it usually took around 45 to 60 minutes for the same purpose [186]. Finally it should be noted that the observed decay of the Bi-diffraction signal in less than 400 fs (Fig. 3.12b) represents an upper limit for the temporal resolution that is possible with the modular setup. A temporal resolution of about 100 fs has been demonstrated with a similar X-ray source in Ref. [106].

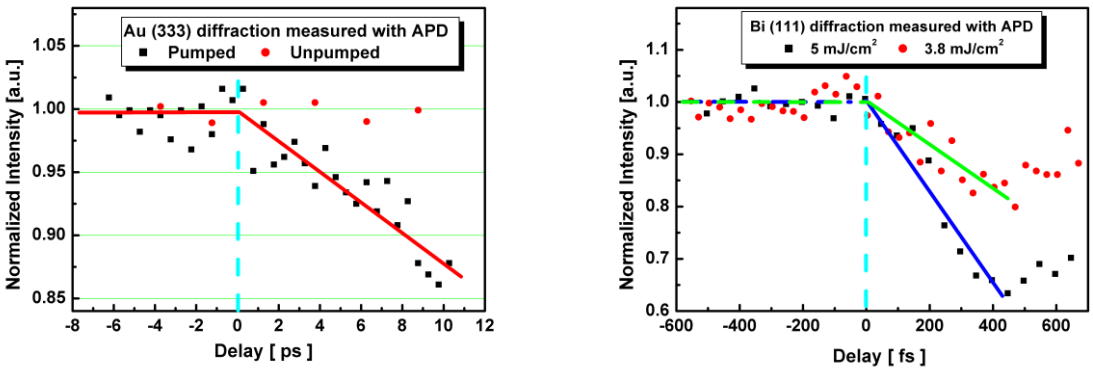

(a) **(b)**

Fig. 3.12 Time-resolved measurements with high temporal resolution detected using APD. (a) Au (333) and (b) Bi (111). The cyan dashed line marks the position of time zero.

3.2.6 Normalization of X-ray signals

Since only a few photons per pulse are diffracted from the thin film samples typically used in the time-resolved X-ray diffraction experiments, it is necessary to accumulate signal over a sufficiently long time (a few hours are usually required for a complete experiment) to enable the measurement of transient changes of the diffraction efficiency at the percent level. During this time, the variation of the X-ray flux delivered to the sample cannot be avoided without a normalization procedure. In the following one needs to distinguish between short-term fluctuations and long term drifts.

"Short-term fluctuations" refers here to all intensity variations of the X-rays occurring within seconds down to pulse-to-pulse fluctuations. They are mainly caused by energy and spatial (pointing stability) instabilities of the driving laser. As mentioned in chapter 2, the laser energy essentially affects the total X-ray yield. Hence, the pulse-to-pulse energy fluctuation results in a fluctuation of the X-ray output signal. For the modular setup, spatial instabilities represent the most critical issue, which had already been detailed discussed in Ref. [186]. Together with the position instabilities of the copper tape with respect to the focused laser spot (caused mainly by mechanical instabilities of the pulling system), the finite pointing stability results in fluctuation of the spatial position of the X-ray source. Due to the short source-to-mirror distance, the overall reflection efficiency of the multilayer X-ray optic is very sensitive to variations of the source position, which lead to significant changes of the X-ray output behind the optic.

"Long term drifts" refer to variations of the X-ray flux within minutes up to hours (see Fig. 3.10). While the sources of these drifts are not completely understood, it must be noted that they cannot be simply averaged out.

Therefore, suitable measurement schemes with reliable normalization procedures are required to maximize the accuracy of the measurement and to minimize the necessary experimental time. Two measurement/normalization schemes are described and discussed in the following sections which allow to handle both, short term fluctuations and long term drifts.

3.2.6.1 Chopping normalization scheme with a shutter

The first normalization scheme I call the "chopping method", which is a low repetition rate variant of a well-known normalization scheme used for all-optical pump-probe experiments at high repetition rate laser systems [193-196]. In this scheme, the pump beam is periodically blocked ("chopped") in order to record the probe signal with and without laser excitation within a short time interval. To achieve this, a mechanical shutter is installed in the pump beam path (see Fig. 3.1) and operated at 1 Hz with an opening time of 0.5 sec. Given the 10 Hz repetition rate of the laser system, the diffraction signal is recorded 5 times with sample excitation followed by 5 times without sample excitation within one shutter cycle. The signals from the PIN diode used to monitor the pump beam energy, allow to mark “pumped” and “umpumped” events in the data stream. The relative change of the signal due to the laser excitation

can be retrieved by normalizing the sum of “pumped” signals to the sum of the “umpumped” signals. In this way both, short term fluctuations (by averaging) and long term drifts (by comparing "pumped" and "unpumped" signals every second) are properly taken into account. However, only one half of the total flux contributes to the transient diffraction signal while the other half is used for normalization.

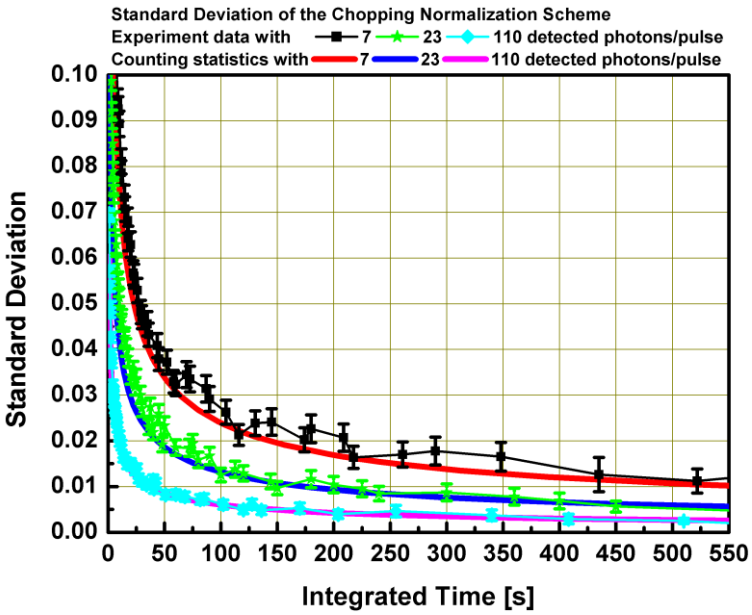

Fig. 3.13 Chopping normalization scheme: Standard deviations as function of integrated acquisition time with different detected photon numbers per pulse. Data points obtained from the experiment and solid curves are calculated from counting statistics.

In the ideal case the achievable accuracy of the experiment is determined by the counting statistics through the total number of detected photons (given by the laser repetition rate, the number of diffracted photon per pulse and the acquisition time). Since the laser repetition rate is fixed and the number of diffracted photons per pulse is determined by the diffraction efficiency of the sample and the X-ray source performance, the acquisition time is the only parameter to control the accuracy of the experiment. In order to define the required acquisition time for a desired accuracy, a series of test measurements were performed with Bi- and Au- samples. Each set of the diffracted signals from these two samples were recorded with the APD for approximately one hour in the same experimental conditions without sample excitation. The detected APD-signal for each set of data was varied by changing X-ray source production (adjusting the energy of the driving laser for the X-ray source) and by choosing different Bragg-reflections. The data are analyzed with a MATLAB routine

which artificially groups the data in "pumped" and "unpumped" events (assuming "chopping" at 1 Hz) and averages and normalizes the diffraction signal over bins of different size (i.e. the number of pulses used to produce one normalized data point). Each specific binning produces a set of data with different number of points, as the number of points times the binning size equals the same number determined by the total acquisition time. The standard deviations of each data set are calculated and presented in Fig. 3.13 as a function of the acquisition time for one point (determined by the binning size). Since the APD has been calibrated one can calculate the expected standard deviation of the measured diffraction signal S, assuming that it is determined only by counting statistics as $\Delta S / S = N^{-1/2}$, where N is the total number of detected photons in the respective acquisition time [197, 198]. These calculated values are plotted as solid lines in Fig. 3.13 and they are used to compare to the experimentally determined values. Note that due to the "chopping" method used for normalization only one half of the detected photons contributing to the signal have been taken into account in the latter calculation (the other half has been used as reference for the normalization). As one can see in Fig. 3.13, the experimental data strictly follow the counting statistics curves with the respective number of detected photons. It indicates that this normalization scheme allows to reach the fundamental limit set by counting statistics in the experiment. Moreover, this figure also provides the required acquisition time for a desired accuracy for a given diffraction signal (number of detected photons per pulse). For example, if one intends to have an accuracy of 1% with 23 detected photons per pulse, an acquisition time of 150 seconds per data point is sufficient.

3.2.6.2 Direct normalization scheme with the ionization chamber detector

As I have already pointed out in section 3.2.3, that the ICD allows the direct measurement of the X-ray beam intensity behind the multilayer optic. The signals generated by the ionization chamber are proportional to the incident X-ray flux on the sample. Therefore, they can be used as a reference to normalize the diffraction signals on a pulse-to-pulse basis. In order to account for the long term drift of the ICD signal mentioned in section 3.2.3, a “fast” scanning technique adapted from all-optical experiments [199] has been combined with this normalization scheme. "Fast" scanning means that the full delay range to be investigated in a particular experiment is

repetitively scanned in a relatively short time (during which drift effects are small) and the data from all scans are summed up and averaged.

In order to check the accuracy achievable with this scheme, a series of similar test measurements as above were performed using the ICD for normalization for different levels of the diffraction signals (given again in number of detected photons per pulse). This time the data were treated as a set of “fast” scanning measurements by artificially sorting them into a number of "delay scans" with a certain number of delay points and pulses per delay before normalization. As the result of this analysis, Fig. 3.14 shows the obtained standard deviation as a function of the total measurement time for a single "delay" at different levels of the diffraction signal (data points) and compares the experimental data to calculated curves assuming again counting statistics as the limiting source of error. Again the experimental data agree well with the counting statistics curves, demonstrating that the "fast" scanning scheme can indeed correct the long term drifts.

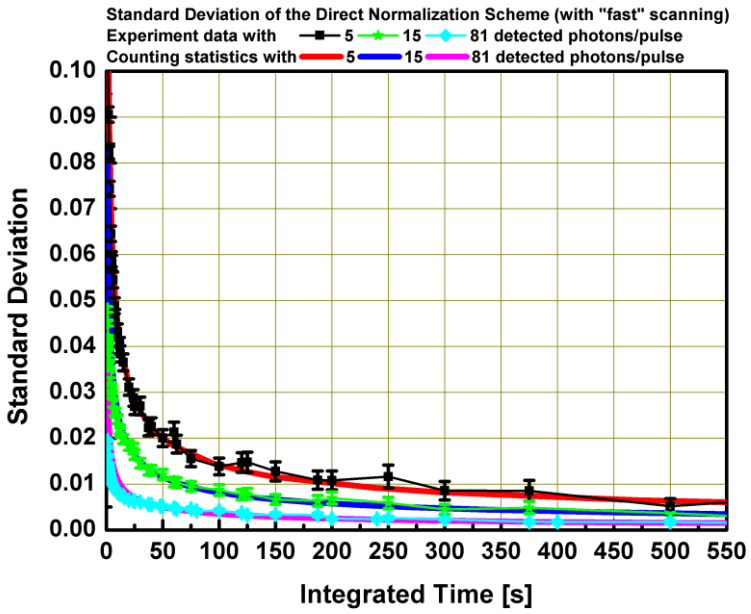

Fig. 3.14 Direct normalization scheme with the “fast” scanning technique: Standard deviations as a function of integrated acquisition time with different numbers of detected photons per pulse. Point data obtained from the experiment and solid curves are calculated from counting statistics.

3.2.6.3 Comparison of normalization schemes

Finally the two normalization schemes discussed above will be compared in this section for similar experimental conditions (i.e. same X-ray flux after the X-ray optic, same diffraction efficiency of the sample). For this comparison one needs to consider that the ICD has a transmission of 72%. Therefore using the direct normalization scheme 28% of the incoming X-ray flux serves as reference signal and only 72% are used for diffraction. Since the number of detected photons in the ICD is large (a few times 10^4) the error of the measurement with direct normalization is determined only by the counting statistics of the diffraction signal (see previous section). The standard deviation in this case is $\sqrt{\frac{1}{r \times t \times (0.72 \times \mathrm{n})}}$, where r is the repetition rate of laser, t is the total integration time in second, and n is the number of detected photons per pulse. On the other hand, when the "chopping" scheme is used for normalization, the ICD can be removed from the beam path and the full X-ray flux reaches the sample. However, as already mentioned above, only one half of the total signal contributes to the "transient" diffraction signal while the other half is used for normalization. Both, "transient" diffraction and normalization signals are limited by counting statistics, which doubles the error of the normalized signal. Then the standard deviation in this case gives as $\sqrt{\frac{2}{r \times (t/2) \times n}}$. Combining this information one can show that for the same experimental conditions (with same r, t, n), the direct normalization scheme (with "fast" scanning) should give a factor of 1.7 better accuracy than the "chopping" scheme.

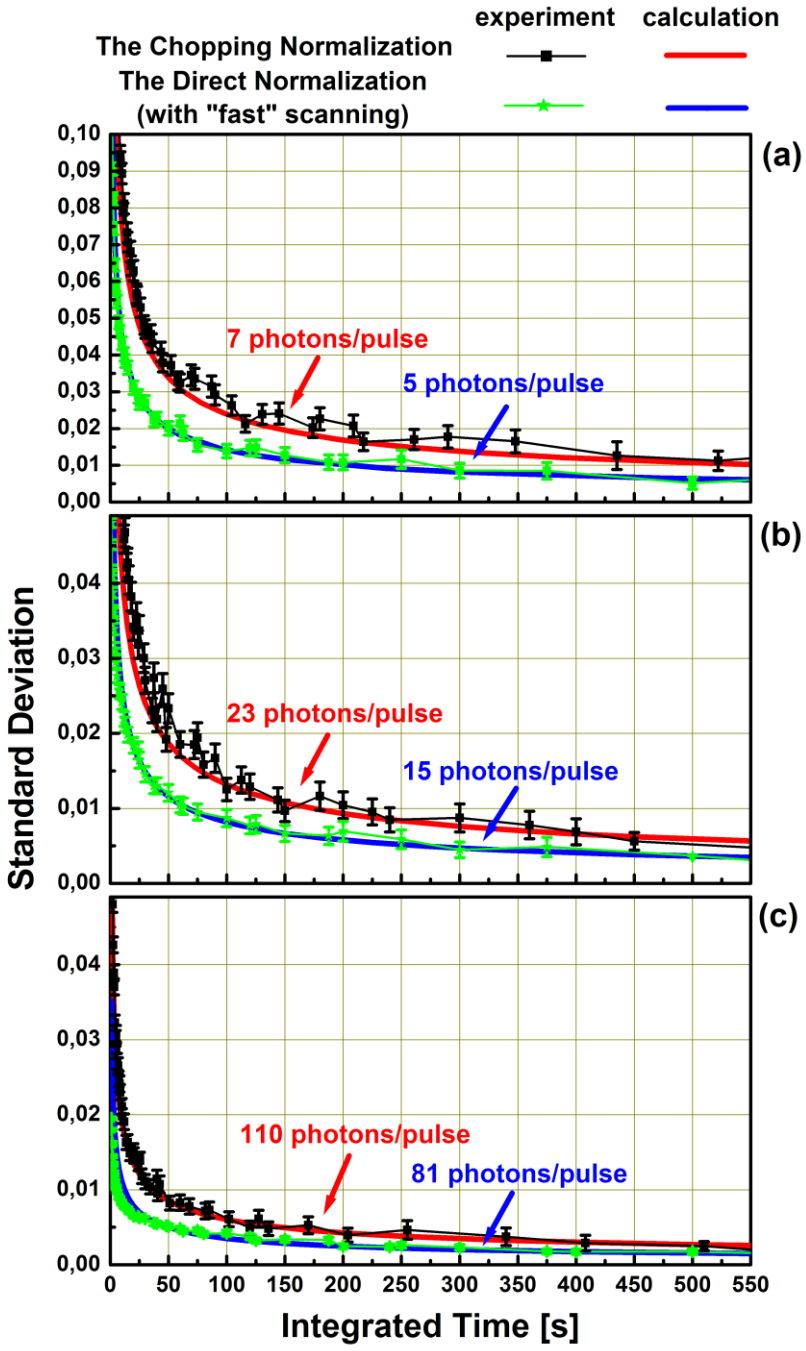

Fig. 3.15 Comparison of the chopping normalization scheme and the direct normalization scheme (with "fast" scanning processing) for the same amount of incident photons from the X-ray optic. (a) with 7 and 5 detected photons, (b) with 23 and 15 detected photons and (c) with 110 and 81 detected photons for the chopping and direct normalization scheme, respectively.

Fig. 3.15 compares the measured error (data points) as a function of accumulation time for the two normalization schemes at different levels of the diffraction signal (the signal level for direct normalization with the ICD is lower than for the "chopping" scheme to account for the transmission losses of the ICD). The red and blue curves

show the calculated error based on counting statistics. Not only do experimental and calculated errors agree very well, the data quantitatively confirm the advantage of the direct normalization scheme discussed above.

In conclusion, the direct normalization scheme represents the most efficient way to perform time-resolved diffraction measurements with the modular setup. Depending on the level of the diffraction signal an accuracy of better than percent for an individual data point can be achieved with accumulation times of tens of seconds to a few minutes.

3.3 Summary

This chapter discussed a modular setup for time-resolved X-ray diffraction experiments at the University of Duisburg-Essen. All components of the previously existing setup as well as the components that have been added to improve its performance have been presented and characterized. Due to its compact design, the setup is easy to operate and adjustments of components are convenient. Applying the results discussed in chapter 2 the X-ray production in the setup has been improved using a controlled pre-pulse. Using an avalanche photodiode as detector for the diffraction signal it has been shown that the combination of "direct" normalization with an ionization chamber as reference detector and the “fast” delay scanning scheme represents the most efficient way to achieve a high measurement accuracy. The setup in its current status has proved its capabilities through several preliminary experiments and has been successfully used for the diffraction experiments that will be presented in the following chapters.

4. Observation of the Debye -Waller effect in Au

Ultrafast x-ray diffraction is a relatively new technique that provides both high temporal and atomic scale spatial resolution to directly observe the atomic motions and changes in the atomic structure of matter upon optical excitation. This chapter will present a laser-pump/X-ray-probe experiment on a thin Au film, the first time-resolved experiment performed with the modular setup described in the previous chapter. The lattice vibrations that result from the electronic energy relaxation following optical excitation have been directly observed through the Debye–Waller effect. The rise times of the lattice temperature were measured for different absorbed laser fluences and compared with the Two-Temperature Model (TTM) [200]. These experimental results are consistent with previous data obtained by ultrafast X-ray diffraction [61] as well as ultrafast electron diffraction [201], and prove the capability of the new built modular setup.

This chapter is organized as follows: The first section is a brief description of the Au sample used in these experiments. In the second section, the Debye –Waller effect is discussed. In the third section, the time-resolved experiments are described and experimental results are presented. In the fourth section, a comparison between the experimental results and calculations based on the TTM model are discussed. In the final section, a summary will be drawn.

4.1 Au sample

Au, a noble metal, has been extensively studied with respect to its transient properties and transient structure after femtosecond optical excitation [61, 186, 201-208]. In

particular, the transient Debye – Waller effect has been recently used in ultrafast electron diffraction experiments to study fast lattice heating after femtoseond laser-excitation of thin, polycrystalline Au films [201, 206].

In the experiments described in this chapter, an epitaxial Au film was used. The 150 nm thick, (111)-oriented Au samples had been grown on (001)-oriented, high quality Mica using a magnetron sputtering technique and were provided by the company Phasis [209]. Relevant physical parameters of this sample are provided in Appendix C.3.

To maximize the pump-induced changes of the diffraction signal due to the Debye-Waller effect, measurements were performed using the symmetric (333)-reflection (see also next section). The corresponding Bragg angle (measured relative to the surface!) is $78.9\,°$ for Cu K_α radiation. Given the angle of $10\,°$ between the optical pump beam and the X-ray probe, the angle of incidence (measured to the surface normal!) of the pump is $20\,°$. The corresponding reflectivity of the sample at 800 nm is 97%. The optical penetration depth is about 13 nm, which is much smaller than the film thickness [210]. Nevertheless, fast ballistic electronic transport distributes the deposited energy over the whole film thickness within a few hundred femtoseconds [211-213]. Therefore, the sample can be considered as being homogeneously excited on the time scale of a picosecond.

4.2 Debye –Waller effect

Debye [214] and Waller [215] found that by heating the lattice, the intensity of Bragg-reflections decreases, whereas their angular profiles (*rocking curves*) remain unchanged. This decrease is described by the Debye-Waller factor DW(T):

$$DW(T) = \frac{I_T}{I_0} = \exp(-\frac{1}{3}\left\langle \Delta\vec{r}^{\,2} \right\rangle G_{hkl}^2) \qquad (4.1)$$

where I_T is the integrated intensity of a particular Bragg-reflection with Miller indices (hkl) (determined by the reciprocal lattice vector G_{hkl}) at temperature T, I_0 is

the integrated intensity in the case of the perfectly ordered and 'frozen lattice', and $\langle \Delta \vec{r}^{\,2} \rangle$ is the mean square atomic displacement [216].

By calculating $\langle \Delta \vec{r}^{\,2} \rangle$ within the Debye theory for the specific heat [217] and taking into account Braggs law $2d_{hkl}\sin(\theta_B) = \lambda$, the Debye-Waller factor can be represented as [218].

$$DW(T) = \exp\left(-\frac{6h^2 T}{m k_B \Theta_D^2} \cdot \Phi\left(\frac{\Theta_D}{T}\right) \cdot \frac{1}{(2d_{hkl})^2} \right) \tag{4.2}$$

where h is Plank's constant, T is the temperature of material, m is the mass of the atom, k_B is the Boltzman's constant, Θ_D is the Debye temperature of the material, $\Phi\left(\frac{\Theta_D}{T}\right)$ is the Debye function and d_{hkl} is the corresponding lattice constant. Eq. 4.2 indicates that the Debye-Waller effect becomes stronger with a smaller d_{hkl}, i.e. larger changes in the diffracted signal are expected for higher diffraction orders (hkl).

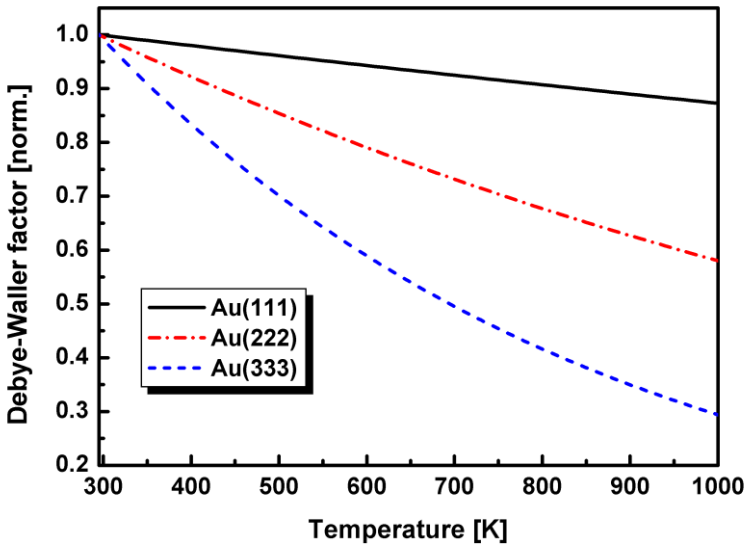

Fig. 4.1 Calculated Debye-Waller factor for Au.

According to Eq. 4.2, the Debye-Waller factor for the (111), (222), and (333) Bragg diffraction of Au are calculated as a function of temperature and presented in Fig. 4.1 (normalized to the corresponding value at 295 K). Since the changes of the

integrated signal are more pronounced for higher orders, the (333)-reflection has been used in following experiments, as mentioned above.

4.3 Time-resolved X-ray diffraction experiments on Au

4.3.1 Bragg diffraction of Au

Before performing the time-resolved experiments for studying the Debye – Waller effect in Au, several preparation experiments were carried out using an area detector ("Gemstar" camera; see Appendix B) to pre-characterize the structural response of the sample upon ultrafast optical excitation.

Fig.4.2 shows as one result the variation of the total diffraction signal with the angle of incidence of the X-ray beam for the Au (333)-reflection. In principle such angular dependencies represent the convolution of three contributions, namely (a) the sample rocking curve, (b) the angular intensity distribution of the focused X-ray beam, and (c) the source spectrum. As a consequence the angular dependence shown in Fig. 4.2 exhibits a two-peak structure which can be attributed to the $K_{\alpha 1}$- and $K_{\alpha 2}$-lines of Cu which are both reflected by the mirror. Each individual peak exhibits a FWHM of about $0.7°$. This is significantly more than the expected width of about $0.26°$ due to the combined effects of the spectral width (FWHM) of the two emission lines (approx. $0.13°$) [219] the angular FWHM of the focused X-rays ($0.17°$ FWHM) [Appendix A], and the expected FWHM of the rocking curve of a 150 nm film ($0.14°$) [220]. The broadened diffraction curve is attributed to the mosaic structure of the Au-film [221].) The following experiments are performed at a sample angle of $78.95°$ corresponding to the maximum detected diffraction signal.

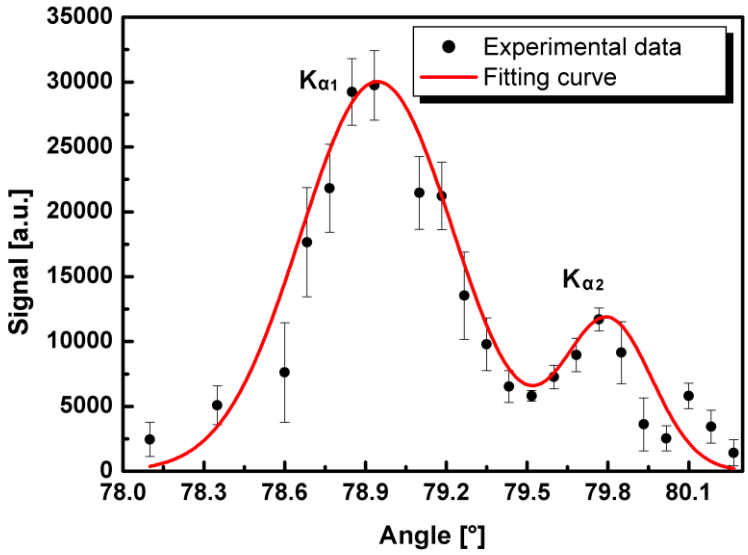

Fig. 4.2 The diffraction signal as a function of sample angle for the Au (333)-reflection, without excitation.

However, upon excitation of the sample not only the intensity of a particular Bragg-reflection can change (e.g. due to the Debye-Waller effect) but also its angular position (and shape) due to laser induced strain. With respect to the latter one it has to be stressed that the angular FWHM of the incident X-ray beam covers only a part of the total width of the diffraction curve. Therefore, for a fixed sample angle, changes of the diffraction signal might be caused by both, real intensity changes as well as a peak shift, due to the fact that strain, if sufficiently large, can shift the diffraction curve out of the narrow angular range of the incident X-ray beam. In order to (preliminary) clarify the effect of strain, time-resolved measurements have been performed for different fluences, both at fixed sample angle as a function of pump-probe time-delay and as a function of sample angle for a fixed time-delay.

Fig. 4.3 shows the shift of the diffraction peak (center of gravity of the distribution of diffracted X-rays measured on the area detector mentioned above) for a (low) absorbed pump fluence of 1.5 mJ/cm^2 (black open squares; the red dots show reference data measured in the course of the experiment without laser pumping). As it is evident, the Bragg-peak starts to shift shortly after excitation towards smaller diffraction angles indicating lattice expansion. The maximum shift/expansion is

reached after about 45 ps. Subsequently the Bragg-peak shifts back to larger diffraction angles indicating recompression of the material. Before discussing this behavior it should be noted that this measurement could be performed with a *fixed* sample angle using an area detector because of the low absorbed fluence, with which the shift of the Bragg-peak is smaller than the angular range of the incident X-ray beam.

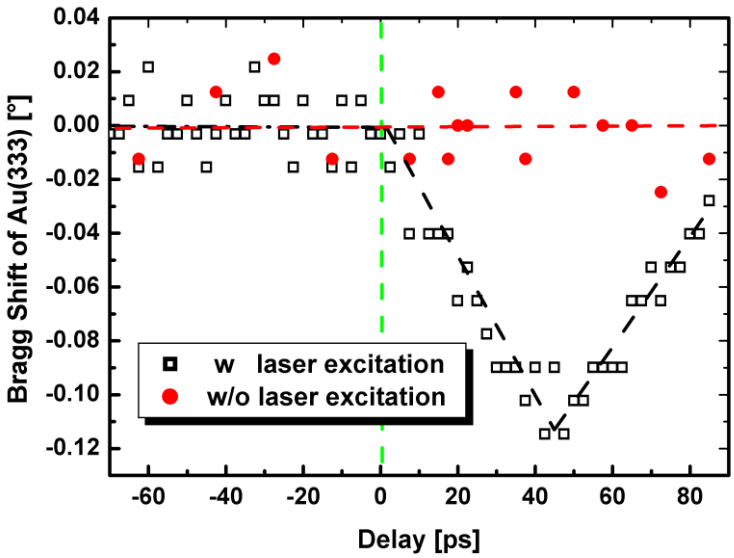

Fig. 4.3 Centers of gravity of the Au (333) rocking curves, measured with the Gemstar camera. Red circles correspond to data obtained on the non-excited sample; the black squares represent data from the excited sample.

The observed behavior, in particular the oscillatory time-dependence of the Bragg-peak shift is in line with the generation and propagation of acoustic waves launched by an almost instantaneous increase of pressure after optical excitation [222, 223]. In this interpretation, the observed period of 45 ps should correspond to the time τ_{ac} that a longitudinal acoustic wave with speed c_s needs to travel through a film with thickness d: $\tau_{ac} = d/c_s$. With the known speed of sound of $c_s = 3.39$ km/s [224] in Au along the (111)-direction and using the nominal film thickness of (150 ± 5) nm, I obtain τ_{ac} = (44 ± 1.5) ps, which is in agreement with the experimentally found value. Very similar results have been recently reported by

Nicoul et al. on a similar Au-sample of smaller thickness (d = 90 nm) [61]. The close correspondence in the time-evolution of the Bragg-peak shift, in particular its "triangular" shape*, give clear indication that also the 150 nm film is homogeneously (as expected – see above) and almost instantaneously pressurized over its whole thickness.

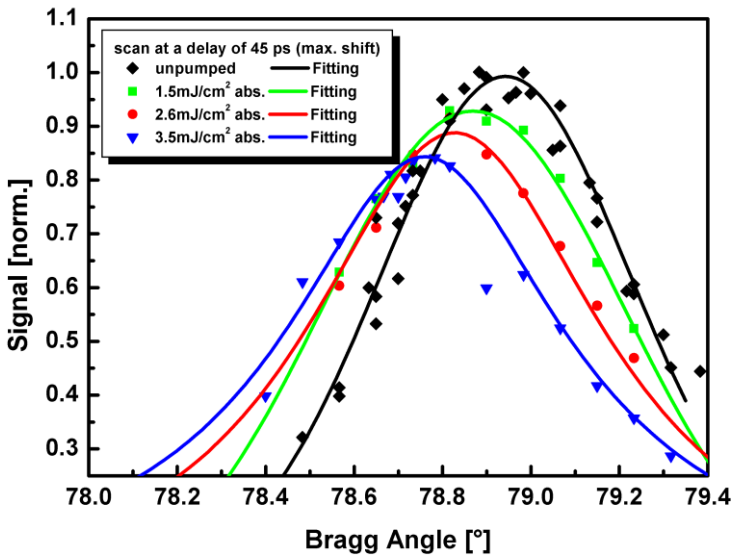

Fig. 4.4 The diffraction signal as a function of sample angle for the Au (333)-reflection at a delay of 45 ps (maximum shift), measured with APD. The points are measured data and the solid curves represent Gaussian fits.

Fig. 4.4 shows the diffraction signal measured with the APD at a delay of 45 ps (maximum shift) as a function of sample angle for different pump fluences; the solid curves represent Gaussian fits to the measured data. The APD has a sufficient large detecting area allowing to perform this measurement without moving its position. As expected the shift of the Bragg peak increases with pump fluence. The peak positions were obtained from the fitting function and are shown as function of absorbed fluence

* The "triangular" shape of the time-trace indicates that the changes of the average interspacing distance inside the sample can be assumed to be linear with time. It is expected for the *time-independent* pressure/stress (the strain waves exhibit a rectangular shape) which results from instantaneously and homogeneously heating of a sample. Detailed interpretations can be found in Ref. [140, 186].

in Fig. 4.5. As it can be seen in Fig. 4.5, the maximum shift of the Bragg-peak caused by laser induced strain scales linear with the absorbed fluence. Such behavior was also observed in other X-ray diffraction experiments [140, 186, 225].

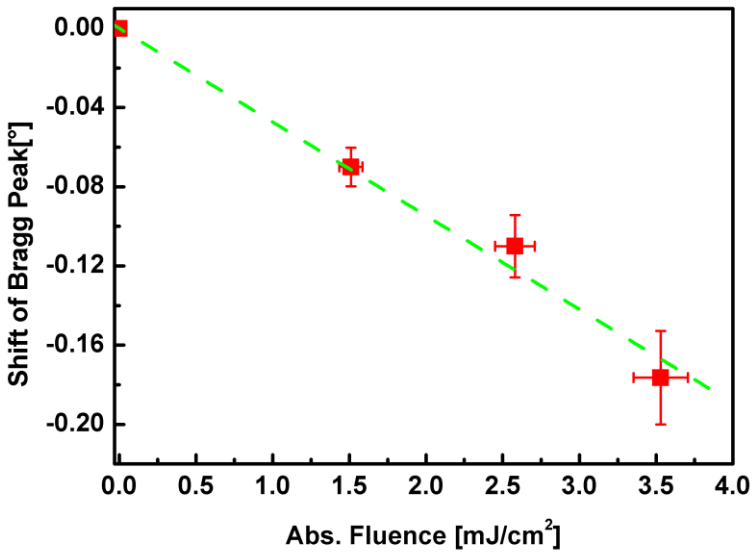

Fig. 4.5 Angular shift of Bragg peak as function of absorbed fluence. The green dashed lines are linear fits for the data points.

In summary the experiments above show that the strain caused by laser-excitation result in a linear shift of the Bragg-peak both, with time (for the first 45 ps) and fluence.

4.3.2 Observation of Debye –Waller effect on Au

In order to obtain the temporal evolution of the Debye –Waller effect without being affected by the laser induced angular shifts of the Bragg peak, an angular compensation procedure is applied during the measurements. This method is based on the results shown in Figs. 4.3 and 4.5, namely the linear increase of the Bragg-peak shift with time and fluence. This allows to properly adjust the sample angle both as a function of pump-probe time delay as well as fluence to stay always at the angular position of the maximum of the diffraction signal.

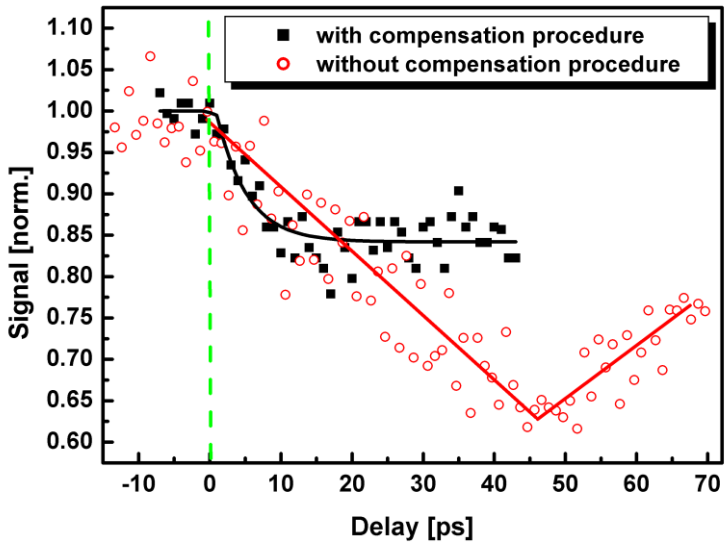

Fig. 4.6 Time-resolved measurements with and without the angular compensation procedure. The black curve is an exponential fit for the data with compensation; the red curve is a guide to eye for the data without compensation.

To illustrate the effect of this compensation Fig. 4.6 shows the results of time-resolved measurements with and without angular compensation at a fluence of 3.5 mJ/cm^2 (absorbed). Without the compensation the detected diffraction signal represents the combined effects of the strain-induced angular shift of the Bragg peak and the Debye–Waller effect. As it can be seen, in this case the detected diffraction signal drops and rebounds at 45 ps, essentially resembling the temporal behavior of the angular shift of the Bragg peak after excitation (see Fig. 4.3). However, with the compensation method, the Debye-Waller effect can be isolated. In this case the measured (normalized) diffraction signal shows a much faster exponential drop with a time constant of about 4.3 ps.

Additional measurements were performed at lower pump fluences applying this angular compensation. The results are presented in Fig 4.7. In all cases the experimental data were fitted with an exponential function and the fitting curves are depicted as solid lines in the figure. Most obvious and not unexpected the decrease of the overall change of the diffraction signal increases with fluence due to the larger

temperature increase achieved at higher fluences. The temporal evolution of the diffraction intensities directly maps out the excitation of lattice vibrations (increase of $\left\langle \Delta \vec{r}^{\,2} \right\rangle$) during heating. After approximately 20 ps, all diffraction signals reach their asymptotic values, which can be considered as the sign of reaching the new thermal equilibrium state in the lattice system.

Applying eq. 4.2 the measured asymptotic drop of the diffraction signal as obtained from the exponential fitting can be converted into a temperature increase. The results are plotted as blue squares in Fig. 4.8 (a). The experimentally determined temperature increases are compared to the temperature increase estimated from the deposited laser energy and the specific heat of the material (red circles). Both data sets agree within their error bars, thus confirming that lattice heating and the Debye-Waller effect is responsible for the observed decrease in diffraction intensity.

The time constant of the exponential fit represents how fast the lattice is heated and the new thermal equilibrium state is reached. The time constant is plotted in Fig. 4.8(b) as a function of absorbed laser fluence (bottom axis) and lattice temperature (top axis). For comparison two data points from previously published experiments [61, 201] have been added. Since the absolute fluence values are often difficult to compare in independent experiments the absorbed fluence value is not used for this comparison but the observed temperature increase (top axis). My measurements agree within the error bars with the previously published data.

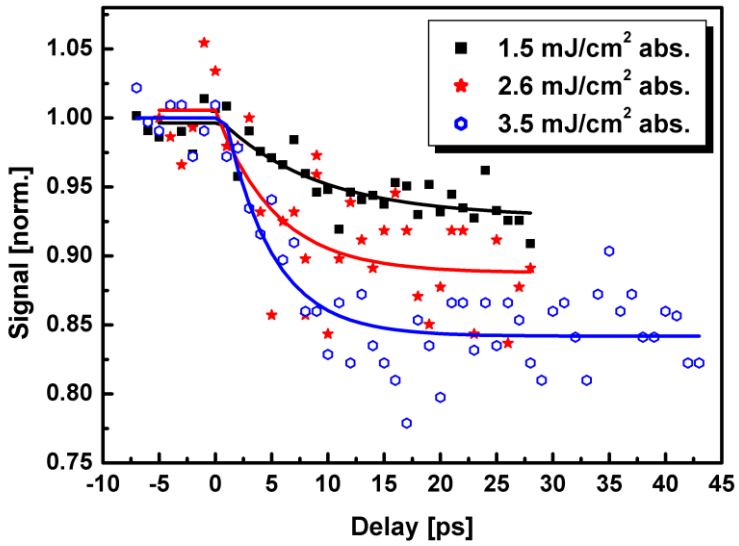

Fig. 4.7 Diffraction signal as a function of delay time for different absorbed fluences (obtained with the angular compensation procedure). The solid curves are exponential fits of the measured data.

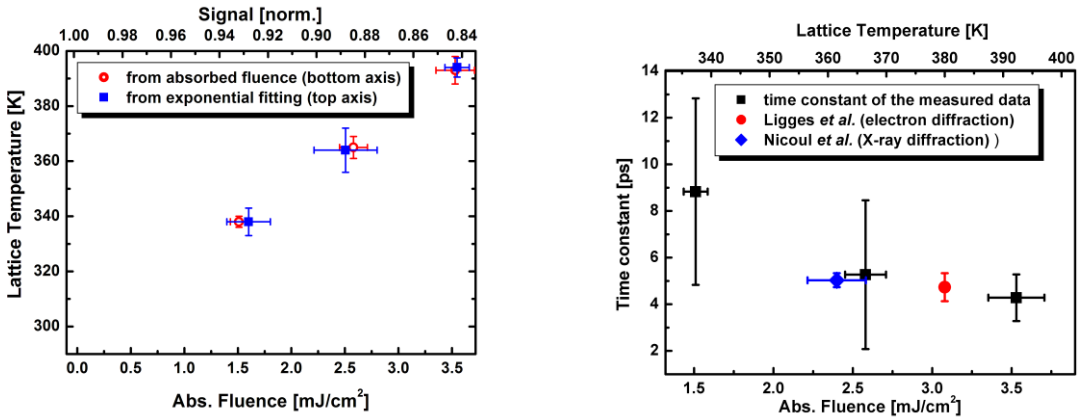

(a) **(b)**

Fig. 4.8 (a) Asymptotic temperature after laser-excitation as a function of absorbed fluence. Blue squares: Values determined by using eq. 4.2 and the experimentally observed asymptotic drop of the diffraction signal (top axis). Red circles: Estimated temperatures from the deposited optical energy. (b) Decay time constant as a function of absorbed fluence (bottom axis) and lattice temperature (top axis). The black square points are obtained from the exponential fits of the measured data in Fig. 4.7. The red circle and the blue diamond are taken from Ref. [201] and [61], respectively.

The data in Fig. 4.8(b) seem to show a tendency that the decay constant decreases with increasing fluence. However, due to the large errors of the derived decay time constants at low fluences this effect will not be discussed further. The only remark to be made here is that the frequently used TTM (see below) does predict the opposite.

4.4 Comparison with the Two – Temperature Model (TTM) and discussion

Upon the laser excitation, the laser energy is first absorbed by free electrons and then exchanges between electrons and the lattice through electron-phonon collisions. The evolutions of the electron and lattice temperature are determined by the electron-phonon coupling constant [226]. In order to understand this process of above experimental results, in this section I compare the experimental results with the theoretical prediction of the two-temperature model (TTM) [200], which is a simple and frequently used model to describe the electron-phonon energy relaxation.

The TTM is based on the assumption that the electronic and lattice system can be described by two different time-dependent temperatures T_e and T_l. The rate of energy exchange between these two subsystems depends linearly on the temperature difference and is given by

$$C_l \frac{\partial T_l}{\partial t} = -C_e \frac{\partial T_e}{\partial t} = \alpha (T_e - T_l) \tag{4.3}$$

where C_e and C_l are the specific heats of electrons and phonons (in principle temperature dependent), respectively. The energy exchange rate parameter α is related to the electron-phonon coupling constant. Solving the differential equation 4.3 numerically by using the coupling constants determined from all-optical measurements [227], not only the electron dynamics, but also the evolution of the lattice temperature can be predicted.

In order to solve this differential equation, the initial temperature of the electronic system is calculated by using the experimentally determined asymptotic

lattice temperature T_{asy}. According to the law of energy conservation and assuming no energy losses, the total initial energy in electronic system soon after laser excitation and in lattice system at initial room temperature is equal to the total energy of electronic and lattice system at asymptotic lattice temperature. One obtains:

$$C_e(T_{e,0})T_{e,0} + C_l T_R = (C_e(T_{asy}) + C_l)T_{asy} \tag{4.4}$$

and

$$C_e(T_e) = A_e T_e \tag{4.5}$$

where A_e and T_R are coefficient of electronic heat capacity and the room temperature, respectively. Then the corresponding initial electron temperature $T_{e,0}$ can be expressed as:

$$T_{e,0} = \sqrt{(\frac{2C_l}{A_e}(T_{asy} - T_R) + T_{asy}^2)} \tag{4.6}$$

Using the deduced parameters and the material constants summarized in table 4.1, equation 4.3 was numerically solved and the results of temporal evolution of lattice temperature are shown in Fig. 4.9 (red dashed curves) together with the measured data for the further discussions.

A_e[J/m^{3}K^2]	C_l [MJ/m^{3}K]	α [10^{16}W/m^{3}K]
67.6	2.45	2.1
T_R [K]	T_{asy}[K]	$T_{e,0}$[K]
295	335	1736.3
	365	2283.1
	390	2654.4

Table 4.1 The material constants of Au and parameters used in the TTM calculations [228].

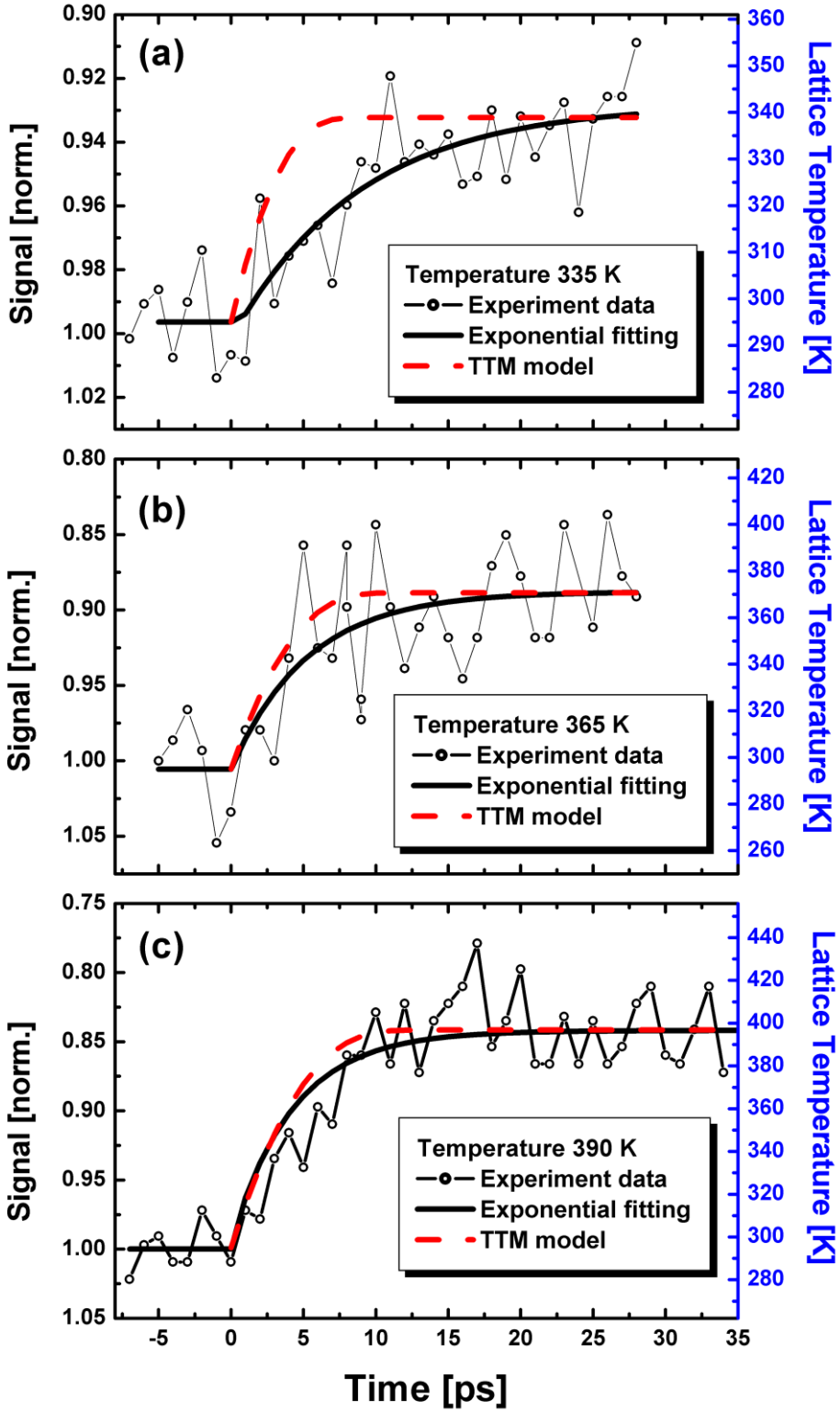

Fig. 4.9 Temporal evolution of the detected X-ray signal (data points, left axis) with exponential fits (black solid curves, left axis), and the results of the numerical solutions of the TTM for the maximum/asymptotic lattice temperature at (a) 335K, (b) 365K and (c) 390K (red dashed curves, right axis).

Fig 4.9 shows again the temporal evolution of the relative changes of the X-ray diffraction signal (data points; note the flipped signal axis to the left) together with the exponential fitting (black solid curve). The right axis displays the corresponding lattice temperature obtained from the DWF. The experimental data are compared to calculated time dependencies (red dashed curves) of the lattice temperature obtained from the TTM-calculations for maximum/asymptotic lattice temperatures T_{asy} of (a) 335K, (b) 365K and (c) 390K. It is evident from this comparison that the TTM with "standard" parameters (table 4.1) provides a good description of the experimental data only for the highest fluence. For the lower fluences the TTM predicts a faster energy relaxation/lattice heating than observed in the experiment. Although B. Rethfeld [229] has predicted such a delayed energy exchange which deviates from the TTM for weak excitation, the effect will not be discussed further here because of the large error of the experimentally determined time constant for the lower fluences. At least for the highest fluence the TTM provides a reasonable description of the experimental data which are, moreover, in good agreement with previously published results [61, 201].

4.5 Summary and conclusion

As the first time-revolved experiment performed with the improved modular setup, the observation of the Debye -Waller effect in Au and its good agreement with both, previous experimental results [61, 201] as well as the TTM at high fluences demonstrates that it is well suited to perform time-resolved diffraction experiments with good accuracy. However, this experiment also reveals a major limitation of the setup: Due to the narrow convergence angle of the incident X-ray beam an angular compensation technique, as discussed above, needs to be applied to eliminate strain effects. As a consequence a pre-characterization of the response of a particular sample is necessary. This made the experiment quite time consuming and might have introduced additional error sources. The modular setup is, therefore, most suitable for measurements where the position and/or shape of the Bragg-peak does not change

upon laser-excitation (at least for a certain range of fluences and/or pump-probe time delays). As will be discussed in chapter 5, this is the case for laser-excited Bi where the Bragg-peak does not start to shift for almost 5 ps after laser excitation.

5. Extreme phonon softening in laser-excited Bi

Bi is a group-V (Nitrogen group) element which contains 5 electrons in its outer shell. It is stabilized at equilibrium into the A7 structure, a rhombohedral structure with two atoms per unit cell. The pairing of these two atoms is attributed to the so-called Peierls–Jones mechanism [230]. This mechanism states that in order to arrange the lattice system in the minimum energy configuration, every second atom along the body diagonal of the Bi unit cell ((111) direction) moves closer to one neighbor and further away from the other, leading to the pairing of atoms along the body diagonal and doubling of the lattice constant. As a consequence of this distortion, a small band gap is introduced at the Fermi level, lowering the total energy of the occupied electronic states, and hence lowering the total energy of the system. This opened band gap is responsible for Bi being a semimetal. A more detail description of the structure of Bi will be presented in Section 5.1.

Due to the unique properties of the broken symmetry ground state of the crystal, the equilibrium structure of Bi is sensitive to external perturbations, i.e. changes of pressure and temperature or electronic excitation [231- 234]. Among these perturbations, the ultrafast electronic excitation with ultrashort laser pulses is particularly unique since the laser induced non-equilibrium states which depend on the excitation level can be precisely controlled by adjusting the pump laser fluence, and thus it can provide unique non-equilibrium states of matter for the investigation of the transient dynamics. Following ultrafast laser excitation, the valence electrons are promoted to the conduction band. The interatomic potential which defines the position of the atoms in the unit cell is altered by the optically induced redistribution of electrons and

the potential minima shift. If this alteration occurs fast in comparison with the time scale of atomic motion, it triggers a coherent atomic motion around the new equilibrium position along the body diagonal, resulting in the modulation of the equilibrium distance of the two paired atoms towards the phase of the higher symmetry. This coherent atomic motion represents the A_{1g} optical phonon mode of the crystal. The generation mechanism has been named *displacive excitation of coherent phonons* (DECP) [231, 232], which can be also considered as a special case of impulsive stimulated Raman scattering for absorbing materials [235, 236].

Within the framework of the DECP mechanism, it has been predicted by theory [237] that the broken symmetry ground state of Bi (the Peierls distortion), can be reversed with high enough density excitation. This structural transformation is accompanied by the change of the electronic properties. The opened band gap at Fermi level should close and Bi transforms from a semi-metal to a metal on the sub-picosecond range. The study of this phase transition process can provide important information not only for the understanding of non-equilibrium structural dynamics in Peierls distorted systems but also for designing future ultrafast electronic devices. So far it is not clear whether this phase transition can be achieved without subsequent disordering/melting of the Bi sample for an initial room temperature lattice. Moreover there is no experimental evidence yet that the structural phase transition to the high symmetry state can be realized. This experimental challenge has been addressed in my PhD work.

In this chapter, the evolutions of laser-excited coherent optical phonons in Bi have been investigated by directly monitoring the atomic motion using time-resolved X-ray diffraction. The observed extreme softening of the A_{1g} phonon mode indicates transient disappearance of the Peierls distortion. This chapter is organized as follows: Section 5.1 provides a brief introduction of Bi. Section 5.2 presents the experiment results and discussion. Section 5.3 summaries the main results of this chapter.

5.1 Research background

5.1.1 Structure of Bi and the phonons

The crystalline form of Bi is the di-atomic basis rhombohedral A7 structure [238], which is derived from a simple cubic structure in two steps. First a simple cubic lattice is stretched along one of the body diagonals creating a smaller shear angle than the cubic value of 60 °. Then a Peierls instability [230] causes the atoms to be displaced along the same diagonal in opposite directions, leading to a reduction of the structural symmetry and a doubling of the lattice constant. Fig. 5.1 illustrates the primitive unit cell of Bi. The first atom is placed at the node of the primitive unit cell and the second atom lies along the body diagonal with a slight displacement from the center of the unit cell. The length of the body diagonal is defined as d, then the corresponding distance for the second atom is $x \cdot d$. At room temperature, the lattice parameters are: $a = b = c = 4.55$ Å, body diagonal $d = 11.86$ Å and $x = 0.468$, i.e. the distance of the pair of atoms is $x \cdot d = 5.5505$ Å.

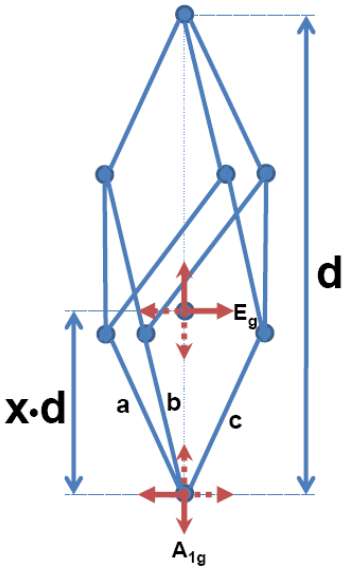

Fig. 5.1 Primitive unit cell of Bi and the motion directions of the A_{1g} and E_g phonon mode.

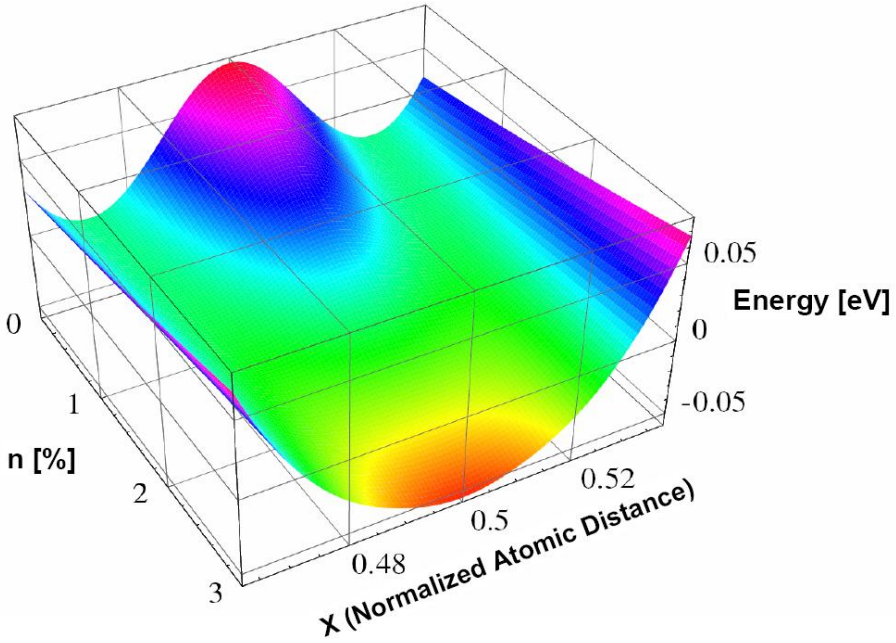

Fig. 5.2 Potential energy surface in Bi as a function of percentage of electrons excited into the conduction band *n* and normalized atomic distance *x*. Picture reproduced from Ref. [237].

Upon the external perturbations, the motion of the two atoms against each other along the body diagonal corresponds to the A_{1g}-optical phonon mode. The motion of the atoms in the plane perpendicular to the body diagonal corresponds to the two (degenerate) E_g-optical phonon modes (Fig. 5.1). The work presented in this chapter has focused on studying the laser excited A_{1g}-optical phonon that can be characterized by the changes of the normalized atomic distance *x* along the body diagonal. Murray *et al.* have used density functional theory (DFT) to compute the potential energy surface (PES) along *x* for different levels of electronic excitation [237]. Fig. 5.2 (taken from Ref. [237]) displays the potential energy as a function of the percentage of carriers excited into the conduction band and the normalized atomic distance *x*. To interpret the experimental results, this PES will be frequently referred to in the remaining sections of this chapter.

5.1.2 Previous works

Bi has been studied by methods of ultrafast optics for over two decades. The coherent optical phonons launched in Bi after femtosecond laser excitation were first

observed by Cheng *et al.* [239] in time-resolved reflectivity measurement. By monitoring the oscillations in the optical reflectivity, the A_{1g} phonon motion was detected and its frequency compared to the results obtained by spontaneous Raman scattering and inelastic neutron scattering [240]. Owing to the high temporal resolution and high accuracy, optical techniques are powerful to retrieve quantitative information about the frequency of the excited phonon and its decay dynamics. The subsequent experiments explored coherent phonon dynamics by studying the phonon frequency [231, 232], the electron-phonon energy coupling [241, 242], the temperature dependence [236, 243, 244] and the excitation level dependence [237, 244-249]. The E_g mode was also observed with optical techniques [236, 244, 249, 250].

However, optical techniques measure the modulation of the dielectric constant. Therefore, they can provide only indirect information about the magnitude of the atomic motion in the excited sample. Providing direct information about the atomic motion in laser-excited Bi ultrafast time-resolved X-ray diffraction [7-9, 17, 18, 39-41, 67-69, 73, 251, 252] and electron diffraction [12, 13, 81, 253, 254] have been recently applied. Two time-resolved X-ray diffraction experiments, which are closely connected to the study presented in this thesis, will be described in detail in the following part.

When a thin film sample with a thickness much smaller than the extinction length [255, 256] is investigated with X-ray diffraction, the secondary scattering of the Bragg reflected beam can be neglected. This treatment is known as the kinematic approximation. Thus the intensity of a particular Bragg reflection (hkl) of Bi is determined by the squared modulus of the geometrical structure factor:

$$I_{hkl} \propto \left|F_{hkl}\right|^2 = \left| 2 f_{Bi} \cos\left[\pi \left(h+k+l\right) x\right] \right|^2 \qquad (5.1)$$

where h, k and l are the Miller indices, f_{Bi} is the atomic scattering factor for Bi, x is normalized atomic distance, which becomes time-dependent after laser excitation. If the Debye-Waller factor is assumed to be constant, a direct indication of the atomic displacement along the trigonal direction inside the unit cell after laser excitation can be presented by the changes in the normalized diffraction signal for the (111) and (222) reflections as

$$\frac{I_{nnn}(t)}{I_{nnn}(0)} = \frac{\cos^2[3n\,\pi\,x(t)]}{\cos^2[3n\,\pi\,x(0)]}, \text{ n=1 for (111), n=2 for (222) reflection} \qquad (5.2)$$

Figure 5.3 shows the normalized X-ray diffraction efficiency of the (111) and (222) Bragg-peaks of Bi as a function of *x*. The diffraction intensity is normalized to the value of x = 0.468 (actual equilibrium value in the unperturbed crystals) and plotted as a function of *x*. In the high-symmetry, non-Peierls distorted state where x = 0.5 (2nd atom in the centre), diffraction from (111) planes is forbidden, whereas (222) diffraction becomes the minimal diffraction order and reaches a maximum value. Impulsive electronic excitation suddenly displaces the minimum of the PES closer to x = 0.5 and the atoms are set in motion towards the new equilibrium position. As a consequence of this motion, the changes in the X-ray diffraction signal are expected to evolve in opposite directions: An increase for the (222)-reflection and a decrease for the (111)-reflection. Following these initial changes, the oscillatory atomic motion around the new equilibrium position should give rise to oscillations of both, the (222)- and the (111)- diffraction signal with a frequency corresponding to the A_{1g} optical phonon mode.

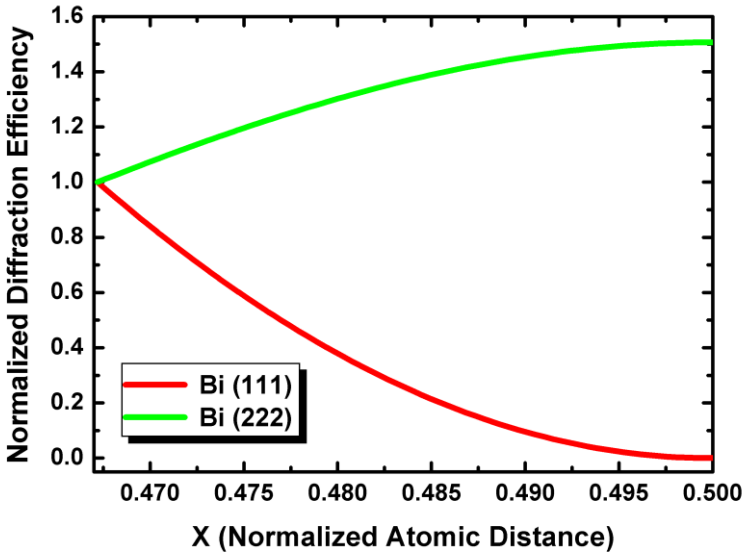

Fig. 5.3 Normalized intensity of Bragg peak (111) and (222) versus atomic displacement expressed in the relative position along the body diagonal.

The first time resolved experiment where X-ray diffraction had been applied to directly follow the atomic motion associated with the laser-excited coherent phonon in Bi was performed by Sokolowski-Tinten *et al.* [68, 251]. In this work, the evolutions of two Bragg-reflections of a laser-excited 50 nm Bi thin film were measured (Fig. 5.4). The frequency of the A_{1g} mode was found to be only 2.12 THz, substantially smaller than the frequency of 2.92 THz measured in non-excited Bi (i.e. by Raman-spectroscopy). The large displacements as well as the strong softening indicated substantial changes of the interatomic potential which had not been observed before in all-optical experiments.

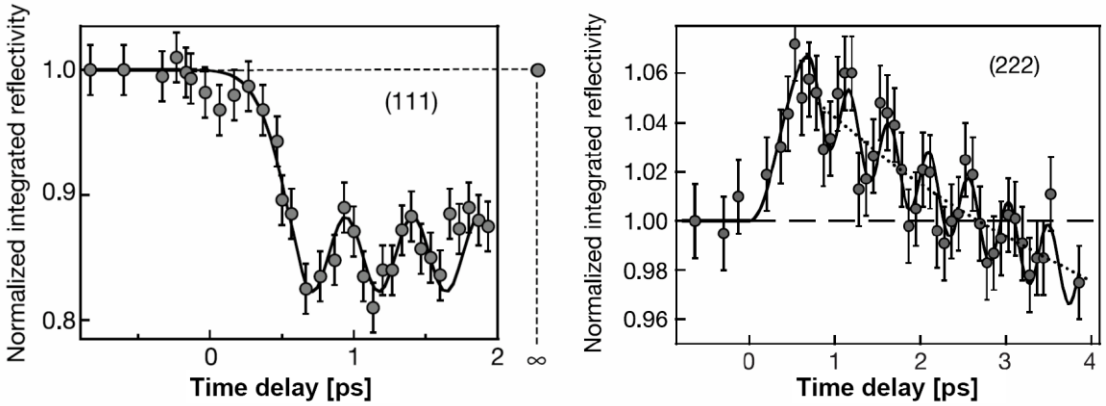

(a) **(b)**

Fig. 5.4 X-ray diffraction efficiency of the (a) (111) and (b) (222) reflections as a function of time delay between the optical pump pulse and X-ray probe pulse. Coherent phonon oscillations with oscillation frequencies of 2.12 THz were observed. Pictures reproduced from Ref. [68].

However, due to the limited signal-to-noise ratio that was available with the laser plasma-based source at that time, this successful work was only achieved at a relatively high excitation fluence. A systematic investigation of the frequency and amplitude dependence of the A_{1g} phonon towards weaker excitation was required to fill the gap to the all-optical work carried out with lower excitation fluences.

Due to a significantly higher X-ray flux, the Sub-Picosecond Pulse Source (SPPS) [257] at Stanford appeared to be the ideal X-ray source to perform this experiment. The softening of the A_{1g} phonon mode as a function of excitation density

and the detailed mapping of the carrier density-dependent PES were quantitatively characterized for the first time by the work performed at the SPPS [69, 186] . In this work, the optical phonon modes in Bi had been investigated at different absorbed laser fluences up to 2.3 mJ/cm^2. Fig. 5.5 (a) shows four time traces for different excitation fluences. The optical phonon frequency as a function of the normalized equilibrium atomic distance *x* is displayed in the inset of Fig. 5.5 (a). A softening of the A_{1g} phonon frequency was found (from 2.91 THz down to 2.3 THz) with increasing *x*. These data provide direct information about the laser-induced changes of the PES, namely the position of potential minimum as well as its curvature. In Fig. 5.5 (b), a comparison between these measured data and theoretical calculations based on DFT [237] is presented. A good agreement between the experiment and the DFT-results is found.

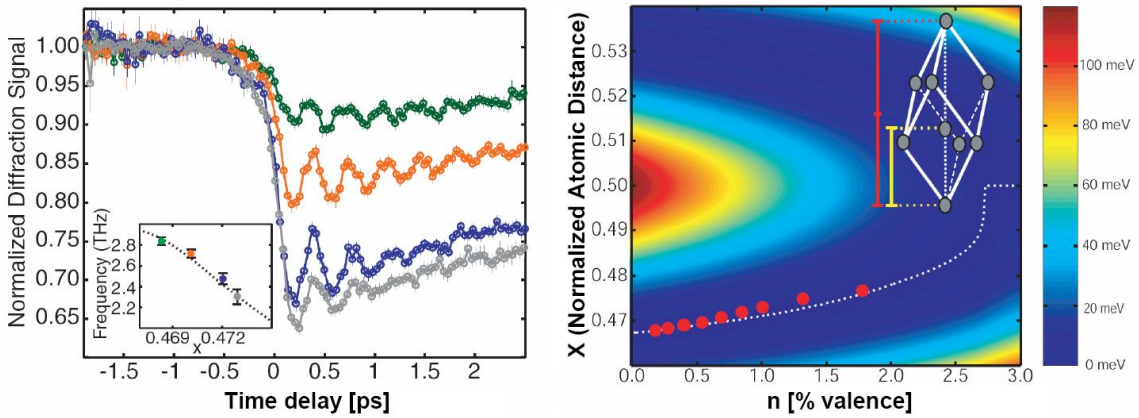

(a) **(b)**

Fig. 5.5 (a) Bi (111) X-ray diffraction efficiency as a function of time delay for different absorbed fluences: 0.7 (green), 1.2 (orange), 1.7 (blue), and 2.3 mJ/cm^2 (gray). The observed A_{1g} optical phonon frequencies are displayed in the inset as a function of *x*, the new normalized (quasi-)equilibrium atomic distance along the body diagonal of the unit cell. The dotted curve represents A_{1g} frequencies predicted from DFT calculations [237]. (b) Normalized quasi-equilibrium atomic distance *x* as a function of carrier density n, with the overlaid excited state PES (false color). The white dotted line represents the equilibrium atomic distance obtained with DFT. The red points are the measured data at the SPPS. The Bi unit cell is depicted in the top right. The ratio of yellow bar to red bar determines *x*. Pictures reproduced from Ref. [69].

These results bridged the gap between the existing work on low and high fluence. However, another interesting question has been raised here: Could the system, when excited with higher fluence, be really driven back to the high symmetry state ($x = 0.5$) and could the Peierls distortion be reversed? To answer this question, I have extended the studies of coherent optical phonons in Bi to a higher excitation fluence regime that has not been studied previously. By using the modular setup [chapter 3], time-resolved X-ray diffraction experiments were performed. A complete softening of the excited A_{1g} mode is observed in the high level excitation data. This represents conclusive experimental evidence that the Peierls distortion, which defines the equilibrium structure of Bi, is transiently reversed.

5.2 Experiments and discussion

5.2.1 Method

The measurements were performed using the modular setup, which was already introduced in chapter 3 (Fig 3.1). X-ray pulses at a photon energy of 8.05 keV (wavelength 1.54Å) were used. The (111)- oriented crystalline Bi sample (50 nm film on Silicon, same type of sample which was used in the previous experiments [68, 69]. More details on relevant parameters of the Bi sample used in this work are provided in Appendix C.) is placed under the appropriate Bragg-angle, 11.24 ° for (111)-reflection and 22.94 ° for (222)-reflection. To launch the A_{1g} optical phonon mode through displacive excitation, the sample was optically excited by near-infrared (800 nm) femtosecond laser pulses with (absorbed) fluences from 1 mJ/cm^2 to 4.2 mJ/cm^2. It should be noted that for absorbed fluences above 2.5 mJ/cm^2, the sample suffered damage after excitation with many pulses. The damage could be detected by monitoring (with a CCD-camera) the scattered fraction of the incident pump light which increased significantly upon damage. From the fact that the increase of pump light scattering occurred long before permanent changes in the X-ray diffraction

signals could be observed it can be concluded that multi-pulse damage occurs initially only at the very surface of the sample. Still, when this increase in scattering was observed the sample was shifted to a "fresh" spot. The atomic motion was probed by measuring the diffraction of the X-ray probe pulses after a controlled time delay with respect to the pump laser pulses. In order to maximize the accuracy of the experiment and to observe small changes in the diffraction signals, the direct normalization scheme with “fast” scanning (see chapter 3) had been applied in the measurements. The diffraction signals of the (111)- and (222)-reflection are recorded with the silicon avalanche photodiode and the signal from the ionization chamber detector is used for normalization. The typical time required to measure a complete time-dependence (approx. 180 delay points) of one diffraction order for one fluence with an accuracy of approximately 1 % was around 6 hours. Comparing to the 12 hours per measurement using the Ti K_α source reported by Sokolowski-Tinten *et al.* [68] (accuracy approx. 2%), this represents a significant improvement.

5.2.2 Preliminary measurements

Before performing the time-resolved experiments for studying laser-excited coherent optical phonons in Bi, two preliminary experiments were carried out to characterize the structural response of the sample upon ultrafast optical excitation.

Fig. 5.6 shows the diffraction signal of the Bi (111)-reflection and the (substrate) Si (111)-reflection as a function of sample angle. The lattice mismatch provides sufficient angular separation of the diffraction signal from the Bi film and the diffraction signal from the Si substrate. As expected the diffraction signal of the bulk Si-substrate is significantly stronger (approx. 20×) than the diffraction from the thin Bi-film. Another important information obtained from this measurement is that the angular width of the Bi diffraction curve (0.3 ° FWHM) is larger than the angular width of the incident X-ray beam (0.17 ° FWHM). As it had been discussed in the previous chapters, in this case the experiments will be performed at a fixed sample angle corresponding to the maximum detected diffraction signal.

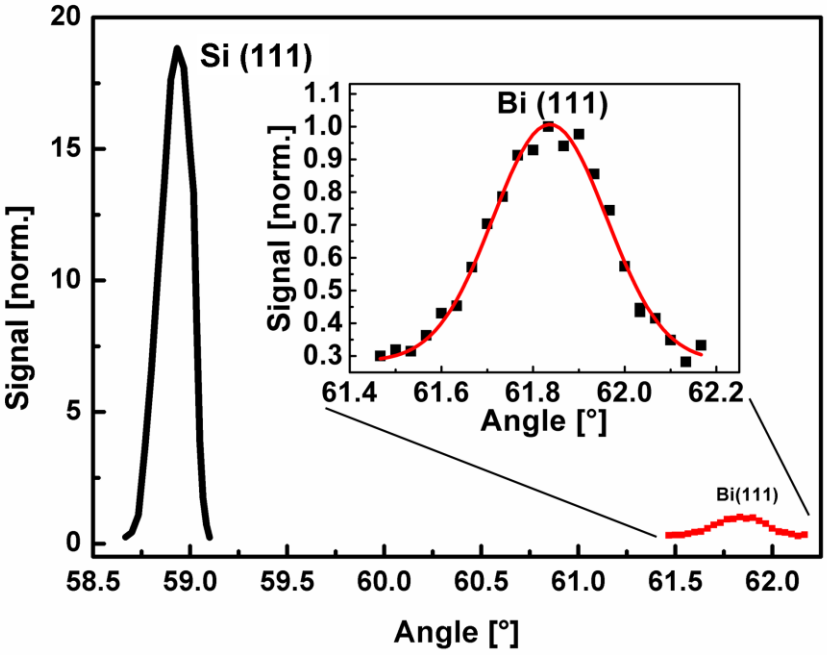

Fig. 5.6 The diffraction signal of Bi (111)-reflection and (substrate) Si (111)-reflection as a function of sample angle. Both signals are normalized to the maximal value of Bi (111) signal.

A preliminary time revolved measurement was performed on the (111)-reflection with an area detector ("Gemstar" camera). This measurement allowed to approximately determine time delay zero and provided some information on the temporal evolution of signal intensity and in particular on the changes of the angular position of the diffraction peak upon laser excitation. The incident pump fluence in this measurement was about 5 mJ/cm^2. The measured results are displayed in Fig. 5.7. Despite the low accuracy of this measurement, three different stages in the temporal evolution of the diffraction intensity can be recognized. Immediately after the photo-excitation, a rapid decrease in the diffraction efficiency is observed followed by a partial recovery of the diffraction signal during the next 5 ps. After that the diffraction intensity starts to decrease again on a 10 ps time-scale. On the other hand the angular position of the (111)-diffraction peak starts to change only after 5 - 7 ps. The shift to smaller diffraction angles indicates lattice expansion.

In consequence, the initial decrease of the diffraction signal and the 5 ps recovery are attributed to changes of the structure factor and thus changes of the normalized atomic distance *x* upon electronic excitation and subsequent relaxation. However, the expected signal oscillations could not be resolved due to the limited accuracy and the coarse delay spacing. Moreover, it is important to note that measurements on Bi can be performed within a time window of about 5 ps *without* a correction of the angle of incidence of the X-ray beam as it was necessary for the case of Au (compare discussion in chapter 4). The following detailed investigation of the coherent optical phonon concentrates, therefore, on this time window of about 5 ps after excitation (marked with the blue dashed-dotted line in Fig. 5.7), where the changes of the signal intensity caused by the shift of the Bragg peak are negligible.

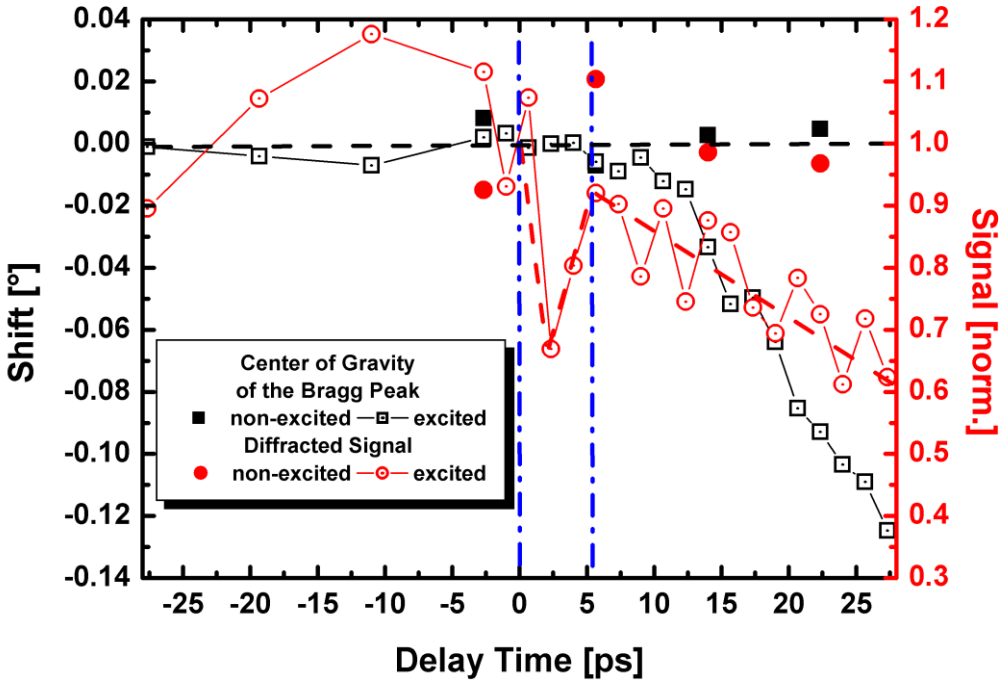

Fig. 5.7 Time revolved measurement with the Gemstar camera. The left axis shows the position of the center of gravity of the Bi (111) rocking curve. The right axis showed the integrated intensity of the diffracted signal.

5.2.3 Results of time resolved measurements and discussion

Before presenting the experimental results and discussion, it should be noted that the effective energy deposition depth of 800nm fs laser pulses is approximately 26 nm [73]. This means that initially only half of the sample thickness (50 nm) is excited. The spatially inhomogeneous excitation of the sample needs to be taken into account in the following discussion.

Fig. 5.8 shows representative examples of time-traces of the normalized diffraction efficiency of the (111)- (a) and the (222)- reflection (b) for different pump laser fluences. Since the absolute time-zero in these experiments is only known to an accuracy of about +/- 150 fs the zero-delay point is "arbitrarily" set for each curve at the half maximum of the initial transient change. A typical error bar of the measured data is given at the end of each curve. While the (111)-reflection exhibits a fluence dependent initial drop followed by oscillations and a slow recovery, the (222)-reflection initially increases in diffraction efficiency followed also by oscillations and a slow recovery. This behavior is similar to the results reported in the previous studies [68, 69] and can be readily interpreted by considering the changes of the geometrical structure factor (see Fig. 5.3) within the DECP-picture: The initial transient change is ascribed to photon-induced alteration of the minimum position of the PES that leads to a atomic motion towards a symmetric arrangement (x = 0.5). The following oscillations correspond to the A_{1g} coherent optical phonon mode of the lattice and the recovery of the diffraction efficiency is attributed to restoration of the PES to its equilibrium state.

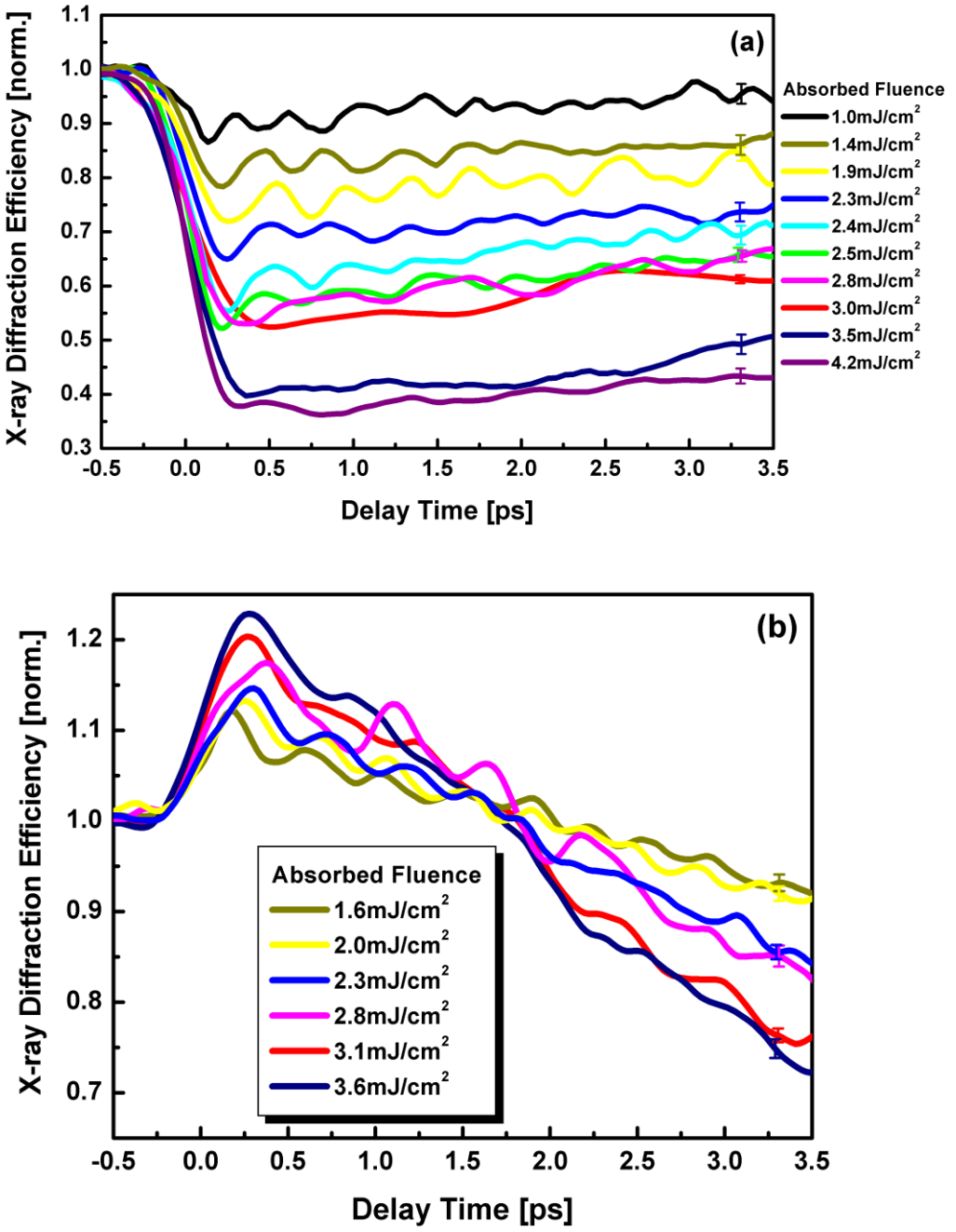

Fig. 5.8 X-ray diffraction efficiency (a): (111)-reflection and (b): (222)-reflection of a 50 nm (111)-oriented Bi-film as a function of pump-probe time delay for different excitation fluences. The zero-delay point is set at the half maximum of the initial transient change. A typical error bar of the measured data is given at the end of each curve.

It should be noted that Fig. 5.3 only takes into account changes of *x*. Upon laser-excitation other effects become important as well. For example, the Debye-Waller

effect caused by an increase of the lattice temperature ("incoherent" phonons) also affects the X-ray diffraction efficiency (see Chapter 4). Although the Debye-Waller effect can be neglected for the first few hundred femtoseconds after laser excitation since the energy exchange between the initially excited hot electrons and the lattice system occurs typically on a time-scale of a few ps, it should be considered in the later recovery processes. For the (111)-reflection, the change in the Debye-Waller factor is calculated to be a few percent from room temperature up to the melting temperature [186]. Relative to the signal changes associated with the induced changes in *x*, the drop in the signal induced by the Debye-Waller effect is negligible. On the other hand, for the (222)-reflection, the change in the Debye-Waller factor is 4 times larger for the same temperature increase and comparable to the effects caused by changes in *x*. The decrease of the mean value of the normalized (222) diffraction signal to values below that of the unexcited sample is tentatively attributed to the combination of the restoration of the PES and the Debye–Waller effect.

In the following section, the magnitude of the initial change of the diffraction efficiency and the frequency of the following oscillatory part are retrieved from the measured time traces and will be discussed in detail.

The initial maximum diffraction efficiency changes ΔI_{111} and ΔI_{222} as a function of laser pump fluence (red: (111)-refl.; black: (222)-refl.) are shown in Fig. 5.9. Data obtained at the SPPS (green) [69] are also plotted in the figure for comparison and they are consistent with the new results. The linear fits of the data points reveal that the initial changes of both reflections are linearly dependent on absorbed fluence. From the comparison of the ratio of $\Delta I_{111}/\Delta I_{222} = -(2.8 \pm 0.2)$ obtained from the fitting slopes and the value of -2.35 as estimated from the change of the geometrical structure factor upon the increase of the Bi-Bi distance *x*, a rough agreement of both values is found and this clearly demonstrates that the coherent motion of atoms is the leading contribution which influences the initial changes of the diffraction efficiencies. The initial atomic motion is proved to be mainly coherent.

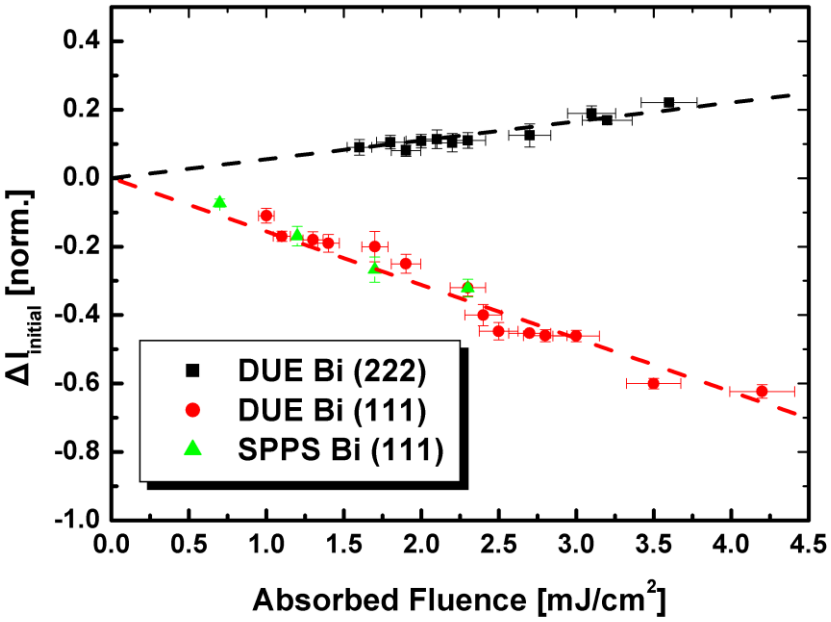

Fig. 5.9 Initial maximum changes of the diffraction efficiencies for the (111)-reflection (red) and the (222)-reflection (black), respectively, as a function of pump laser fluence. The red and black dashed lines are the linear fits for the measured data. The data obtained at the SPPS (green) [69] is also plotted in the figure for comparison.

To determine the frequencies from the oscillatory part of the measured diffraction efficiencies, a Fast Fourier Transform (FFT) had been applied to all measured time traces, including others not shown in Fig. 5.8. The slow background components (initial changes and the slow recovery) are subtracted from the time-traces before transformation. As an example, Fig. 5.10 shows as red solid curve one of those FFT results obtained from a time trace of the (222)-reflection measured at 2.3 mJ/cm^2 absorbed fluence. The FFT is characterized by one main peak at 2.4 THz and a number of secondary peaks. Due to the limited number of phonon periods covered in this measurements as well as the small amplitude of the oscillations, a relatively low signal to noise ratio in this Fourier transform analysis is expected. Therefore only the frequency with the highest amplitude, representing the main contribution of the atomic motion, is considered as reliable. Since the understanding

of the other observable frequency components is still an open question, they will not be discussed further in this thesis.

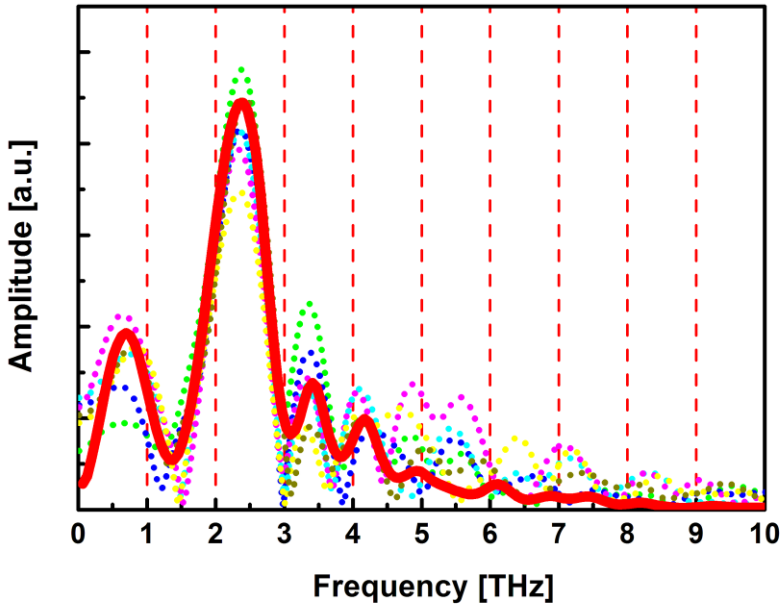

Fig. 5.10 FFT-spectra of the time traces of Bi 222-reflection with 2.3 mJ/cm^2 absorbed fluence. The solid curve and the dotted curves (6 examples) represent the FFT results obtained from the mean time trace and the random time traces produced within its error bar, respectively.

In order to validate this approach and to assess the accuracy of the obtained frequencies, it is necessary to check how the dominant frequencies are influenced by the measurement errors. The following procedure, demonstrated with the time trace used above (222-reflection at 2.3 mJ/cm^2 absorbed fluence), is applied. For each time trace the signal values of the individual data points are randomly changed within the limits set by the error bars. In this way a set of artificial time-traces is produced which represent - within the error - "possible" time traces. The variation of the FFT-spectra of all this "possible" time-traces allows to estimate the error in the FFT and to asses which frequency components can be regarded as "real". In Fig. 5.10, six of these FFT-spectra are presented as dotted curves. With respect to the main peak (the solid curve) it can be concluded that the measurement errors slightly change its amplitude and width but do not affect much its position. The variation of the peak position is

significantly smaller than the peak width, which I consider in the following as the "error" of the measured frequency. In conclusion, the dominant frequency obtained from the FFT can be regarded as reliable and it is assumed that it represents the A_{1g}-phonon mode. Some more FFT-spectra obtained from the measured time-dependencies of the diffraction efficiency are presented in Fig. 5.11.

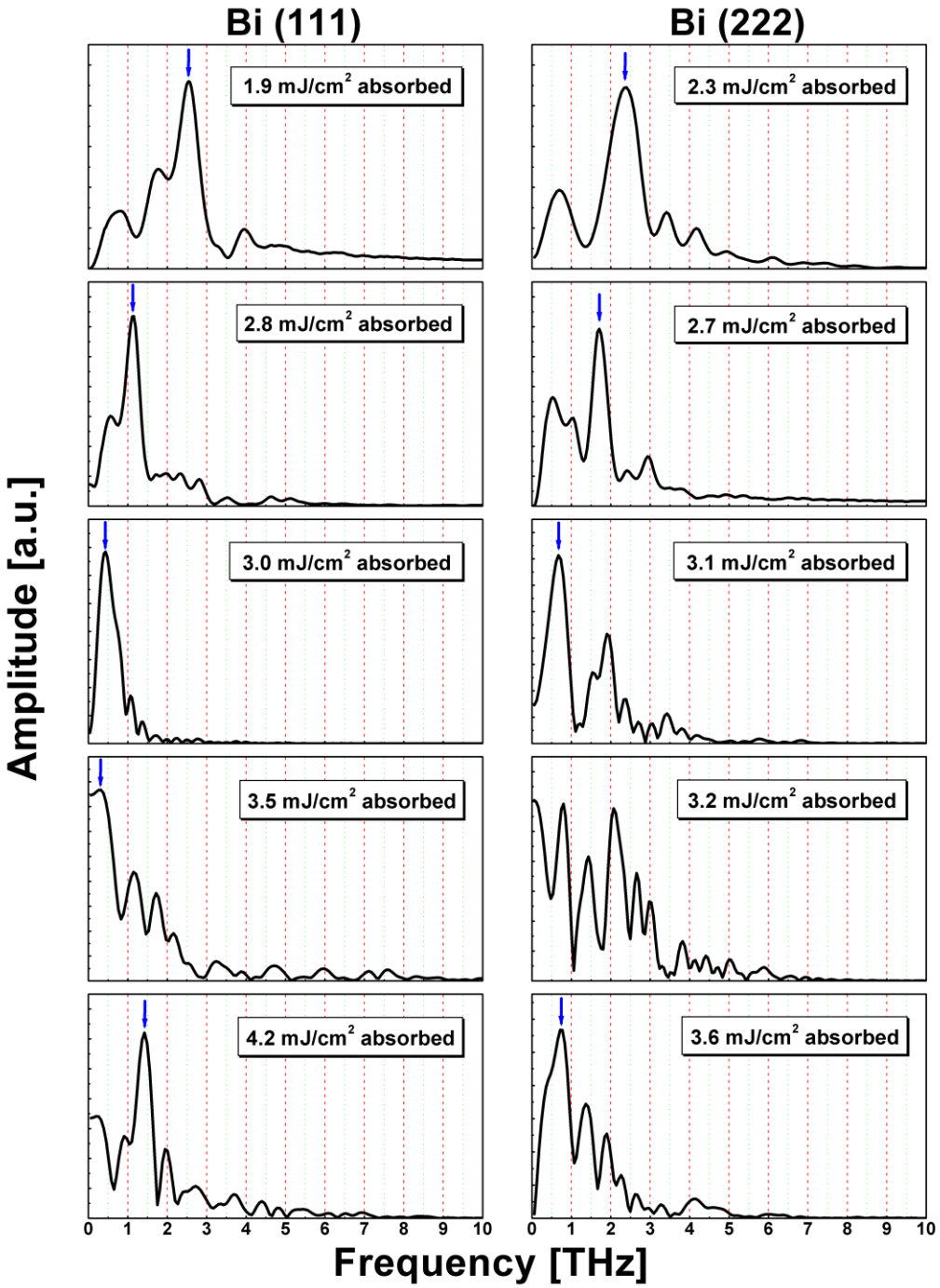

Fig. 5.11 FFT-spectra of the measured diffraction efficiencies for different absorbed fluences. The dominant frequency in each figure is marked by the blue arrow.

Fig. 5.11 clearly indicates that for each fluence a unique "dominant" frequency can be determined, as marked with the blue arrow. The only exception is the one at F = 3.2 mJ/cm^2 where several peaks of equal strength are found. Fig. 5.12 summarizes the result of the FFT-analysis. It shows the determined "dominant" frequency as a function of fluence. The frequency error bars represent the FWHM of a Gaussian fit to the "dominant" peak.

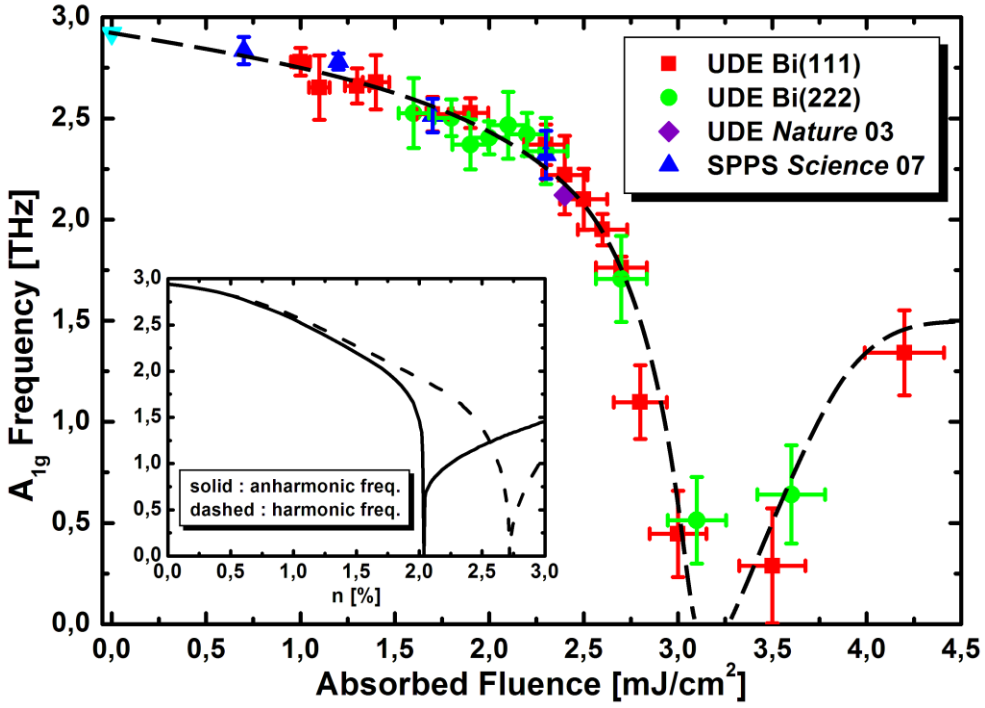

Fig. 5.12 Frequency of the excited A_{1g}-mode as function of laser fluence derived from the time resolved diffraction data; red: 111-reflection, green: 222-reflection, violet: data obtained from earlier results at University Duisburg-Essen (UDE) [68], blue: data obtained at the SPPS [69], Cyan: A_{1g}-frequency of unexcited Bi, black dashed line: guide to the eye. Insert: DFT calculations from Murray *et al.* [237]. The solid and dashed lines show the anharmonic and harmonic frequencies as a function of carrier density n, respectively.

In Fig. 5.12, the red and green data points represent the new data from my measurements. At lower fluences they compare well with the results obtained earlier which have discussed above (violet point: Ref. [68]; blue points: Ref. [69]. Most strikingly, these experimental data reveal an extreme softening of the A_{1g}-mode for

high fluences (> 2 mJ/cm^2). Particularly, by extrapolating the measured data (black dashed line as a guide to the eye) a complete softening at fluences of 3.0 to 3.3 mJ/cm^2 is expected. At first glance surprising, a further increase of fluence leads to the revival of the signal oscillations and an increase of the mode-frequency. The complete softening and later stiffening of the A_{1g}-mode clearly indicate that the Peierls distortion is transiently reversed for fluences above approx. 3.0 mJ/cm^2. Further evidence can be found in Fig. 5.9, where initial signal changes of (111) and (222) diffractions reach approx. -50% and 20% at this excitation level, respectively. These results agree with estimates based on the geometrical structure factor (see Fig. 5.3) assuming that about half of the film thickness had been excited to the symmetric arrangement $x = 0.5$ (where the 111-reflection is fully forbidden).

In order to compare my measured results with the theoretical predictions of the DFT-calculations performed by Murray *et al.* [237], the calculated harmonic and anharmonic phonon frequencies using the PES are presented in the inset of Fig. 5.12 as a function of carrier density *n*. One can immediately see qualitative agreement between the experiment and the calculation. The harmonic frequency computed from the curvature of the PES at the minimum under the assumption of harmonic approximation. The anharmonic frequency obtained from the inverse of the actual cycle period of atomic motion in the anharmonic potential. More detailed interpretations of the two frequencies are provided in Ref. [237] and [258]. At low excitation level, as already proved by experiment [69], there is little difference between the harmonic and anharmonic frequency. The difference becomes apparent at high excitation levels where the range of atomic motion increases, leading to an anharmonic oscillation of the atoms along the asymmetric part of the PES. A detailed interpretation of atomic motion upon laser excitation is given in the following.

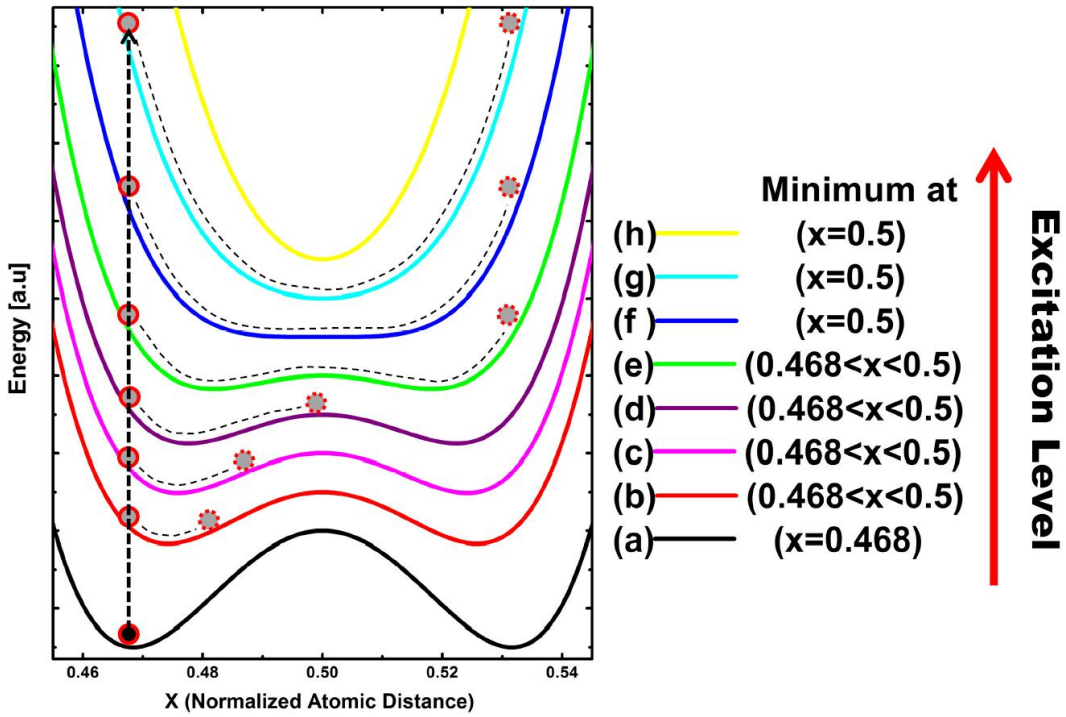

Fig. 5.13 Sketch of the interatomic potential energy surface of Bi upon laser excitation. The black curve represents the shape of initial equilibrium PES. The others represent (qualitatively) the shape of PES upon different excitation levels. For illustrative purpose, the curves are adjusted to be separated in arbitrary unit. The dashed curves along the surface indicate the range of atomic motions.

Within the DECP-picture, the atoms are immediately displaced from their (transient) equilibrium position due to the impulsive laser induced change in the PES. A restoring force whose magnitude and direction are determined by the gradient of the PES is exerted on the atoms, setting them in motion. The frequencies extracted from the X-ray diffraction signals displayed in Fig. 5.12 directly reflect this transient atomic motion along the PES, and yield information regarding the curvature of the PES of the excited sample. In order to concisely interpret this oscillatory behavior, I illustrate qualitatively the shapes of the PES of Bi upon laser excitation and the possible range of atomic motion in Fig. 5.13.

The initial equilibrium PES of Bi has a double well structure with the minimum position at x = 0.468 (curve (a)). For weak excitation, a slight shift of the minimum position of the PES and a slight decrease of the Peierls barrier can be seen (curve (b)). The atomic motion is limited to a small range around the equilibrium position and the

atom oscillates harmonically along the PES. Anharmonicity is negligible. The frequency drops approximately linearly with excitation fluence. This situation corresponds to the excitation level up to 1.5% of carrier density in the DFT calculation and excitation fluences below 2.5 mJ/cm^2 in Fig. 5.12. Extensive studies [68, 69, 237, 244-246, 248, 249, 259] on the generation of coherent optical phonons in Bi have been performed in this region with time-resolved optical and X-ray techniques. Up to now, no study has been carried out beyond this level of excitation. The behavior in this unexplored area has been revealed in this work.

Following the increase of the excitation level the range of oscillatory atomic motion becomes larger (curve c). The asymmetric, anharmonic shape of the PES leads to an additional increase of the period of atomic motion which defines the "anharmonic" phonon frequency shown in the inset of Fig. 5.12. It differs significantly from the harmonic frequency (defined by the curvature of the PES at the minimum). This situation corresponds to 1.5% ~ 2% of excited carrier density in the DFT calculations and the excitation fluences of 2.5 ~ 3 mJ/cm^2 in Fig. 5.12.

Upon further increase of excitation the system can reach the particular state in which the Peierls barrier becomes low enough to let the atom just climb to its top where it stops (curve d). In this labile equilibrium atomic motion freezes and the anharmonic frequency becomes zero. After reaching the above particular state, the Peierls barrier is further lowered by an increased fluence and the atom is allowed to cross the x = 0.5 position and moving in both wells (curve e). As the atomic motion restarts, the phonon frequency revives. Upon further increase in fluence the double well and the barrier vanish. The minimum of the PES is now at x = 0.5, which means that the Peierls distortion has been transiently reversed. Right at the transition the harmonic term of the PES vanishes (curve f) which corresponds to the situation where the harmonic frequency becomes zero. These happen at an excitation level of 2% ~ 2.7% of carrier density in the DFT calculation and absorbed laser fluences between 3.0 to 3.3 mJ/cm^2 in Fig. 5.12.

With the further increase of excitation level, corresponding to the value beyond 2.7% of carrier density in the DFT calculation and absorbed laser fluences above 3.3

mJ/cm^2 in Fig. 5.12, the PES is continuously altered and the two minima converge to one transforming the flat profile to the "sharp" parabola with the minimum position at x = 0.5 (curve g and h). As the relative potential energy (to the minimum of the PES) increases, the atom moves along a parabolic surface with higher velocity, thus shortening the motion period and leading to an increase in the phonon frequency. The A_{1g} phonon mode stiffens. However, it should be noted that due to the already reversed Peierls distortion and the transformation into a more symmetric structure with only one atom per unit cell, this atomic motion correspond now to an acoustic phonon mode at the new Brillouin-zone boundary.

In contradiction with the above description about the range of atomic motion, the observed oscillation amplitudes in the measured data (see Fig. 5.8) are much smaller compared to the average signal change. A very strong damping in the A_{1g} atomic motion can be responsible for the observation. The reason of the damping effect is not fully understood yet. Considering the high excitation level applied in the measurements, a coupling of the A_{1g} mode to other modes (e.g. E_g mode), which was proposed in the earlier electron diffraction experiment [81] and predicted in calculation by Zijlstra *et al.* [260], could be the reasonable explanation for this effect. Since the system performs small amplitude oscillations around the new equilibrium position/potential minimum, I suppose the experimental results are more suitable to be described by the "harmonic" frequency.

Finally, it should be noted that the above description of the A_{1g} phonon behavior follows the results of the first principles DFT calculation [237] which applies separate chemical potentials for electrons and holes. This model has been proved to be quantitatively correct for low excitation fluences [69] and at least qualitatively in good agreement with my experimental results. The other approach proposed by Zijlstra *et al.* [260] using all-electron full-potential linearized augmented planewave method (FLAPW) [261, 262] provides a description not only on A_{1g} phonon but also on E_g phonon and interactions between them. This model could be more accurate for the situation of Bi at the high level excitation. While these two theoretical calculations

differ quantitatively, they qualitatively predict similar changes of the PES and the phonon frequency.

5.3 Summary

In summary, an investigation of the laser-excited A_{1g} coherent optical phonon mode in Bi was performed with the laser plasma X-ray source. The reversal of Peierls distortion, as well as the coherent motions of atoms in Bi following laser excitation, was observed. In the low excitation regime, the data agree with previous results obtained at UDE and the SPPS. In the strong excitation regime (absorbed laser fluences > 2 mJ/cm^2), an extreme softening of the A_{1g} mode was observed and an interpretation was given. Particularly, the observation of a complete softening (frequency down to zero) at fluences of 3.0 to 3.3 mJ/cm^2 indicates that the Peierls distortion defining the equilibrium structure of Bi transiently vanishes. At even stronger excitation (absorbed laser fluences > 3.3 mJ/cm^2), Bi starts to respond as a material arranged in the structure with half of its equilibrium lattice constant and the atomic motion becomes a Brillouin-zone boundary acoustic phonon mode. These observations follow at least qualitatively the predictions of calculations based on DFT [237, 260].

However, due to the limited experimental accuracy, these results do not provide more detailed information with respect to the damping behavior of the oscillations, the decay of coherent phonons and the coupling of the phonon modes. For further detailed investigation in the high excitation region, more powerful X-ray sources (e.g. XFEL or LCLS) are needed.

As already mentioned in the experimental section, accumulative sample damage was observed when absorbed fluences beyond 2.5 mJ/cm^2 are used. It indicates that the applied excitation density is close to the melting threshold of the Bi sample. It questions how the phonons respond to excitations far beyond the melting threshold which allow the melting of Bi sample with a single laser pulse? Such a question had recently been investigated by Sciaini *et al.* [81]. The ultrafast melting of Bi had been

observed with time-resolved electron diffraction. It was found that under extreme excitation conditions the disordering of the Bi crystal structure occurs within 190 fs, which is substantially shorter than the disordering time determined by lattice heating, indicating a non-thermal melting process. The authors attribute such surprising speed of the non-thermal solid-to-liquid phase transition in Bi to laser induced changes in the PES, which result in strong acceleration of atoms along the longitudinal direction (A_{1g} mode) and an efficient coupling of this motion to the transverse mode (E_g mode). This coupling effect had also been theoretically predicted by Zijlstra *et al.* [260] in high excitation regime. In order to obtain the insight into more details of DECP mechanism and subsequent phonon dynamics at the high excitation regime, the E_g phonon motion as well as the coupling effect of A_{1g} and E_g mode should be included in this study. However, since amplitude of the E_g mode is much smaller than the one of the A_{1g} mode and the experimental geometry in this measurement is not sensitive to E_g motions, the E_g phonon mode as well as the coupling effect has not been observed in my data.

Nevertheless, a complete insight of A_{1g} optical phonon dynamics in laser excited Bi, from the weak excitation to melting, is provided now from the results of three excitation levels (low: data from SPPS, high: data in this thesis, extreme: data from electron diffraction). The transient reversal of Peierls distortion happening before the disordering of Bi crystal structure has been experimentally confirmed. The structural change resulting from the coherent phonons has been indicated by the appearance of the acoustic phonon mode. Since many properties of a solid including the electronic, thermal and optical properties are affected by lattice structure, this knowledge of ultrafast structural changes caused by electronically altered energy surfaces can be extended to understand not only the phonon dynamics of other Peierls distorted materials (Sb and As), but also the mechanism of ultrafast phase transition in other functional materials, e.g. insulator-metal transition in VO_2 [263, 264] and crystalline-amorphous transition in chalcogenide alloys [265, 266].

6. Towards time-resolved Debye-Scherrer X-ray diffraction

The observation of the transient changes of a single Bragg-reflection in a femtosecond X-ray diffraction measurement provides only limited information about the transient structural response of optically excited materials. To obtain a more complete picture of the induced processes, it is desirable to monitor as many Bragg peaks as possible. The Bragg diffraction scheme with a monochromatic source applied in the experiments discussed in chapter 4 and 5 requires single crystalline samples of high quality, and thus the range of materials that can be studied is limited. Moreover, a sequential measurement of many individual Bragg peaks is time consuming and difficult to handle due to multiple sample adjustments (sample rotations), as well as the instability of the laser and X-ray sources. One alternative for effectively measuring multiple diffraction peaks with single crystalline sample is the so-called rotating-crystal method [74]. By rotating a single crystalline sample at a high constant angular velocity (e.g. 180 °/s), the Bragg condition for different diffraction peaks is fulfilled and simultaneously allowing a detection of a larger number of transient diffraction peaks under the same experimental conditions in one measurement. Again, this method requires good sample preparation, precise mounting and alignment of the sample as well as extremely stable mechanical components.

Moreover, not all materials can be prepared as crystalline thin films (thin films are necessary in order to match the optical absorption depth to the X-ray probing depth). On the other hand, many materials can be prepared in polycrystalline form. For polycrystalline materials the well-known Debye-Scherrer scheme [267] represents a simpler approach to access simultaneously multiple Bragg peaks. The simultaneous

detection of several reflections/diffraction rings without additional (sample adjustments and mechanical stability) requirements allows conveniently getting as much as possible information of the sample from one measurement. A successful time-resolved experiment using the Debye-Scherrer scheme on a thick (250 μm) powder sample has been recently reported [106]. Since a material with a large unit cell size was used multiple diffraction rings were recorded simultaneously, proving the relocation of charges within the unit cell with a time resolution of 100 fs. This result demonstrates the feasibility of using a laser-plasma based X-ray source for investigating a wide range of polycrystalline inorganic and organic materials with time-resolved Debye-Scherrer diffraction.

The use of an X-ray optic with high magnification in the modular setup (see in chapter 3) can provide a quasi-collimated beam, well suited for the Debye-Scherrer diffraction scheme. In the work discussed in this chapter, I performed Debye-Scherrer X-ray diffraction experiments on thin polycrystalline metal films and I demonstrated the possibility to perform time-resolved experiments with the modular setup. The first part of this chapter presents the experimental configuration. In the second part, static Debye-Scherrer diffraction measurements on a 20μm Cu foil are presented. This measurement serves as comparison to results previously obtained by U. Shymanovich using a different kind of focusing X-ray optic (elliptical capillary) [105]. In the third part of this chapter, results of a time-resolved X-ray Debye-Scherrer diffraction measurement on a 200 nm Au film are presented and discussed.

6.1 Experimental configuration

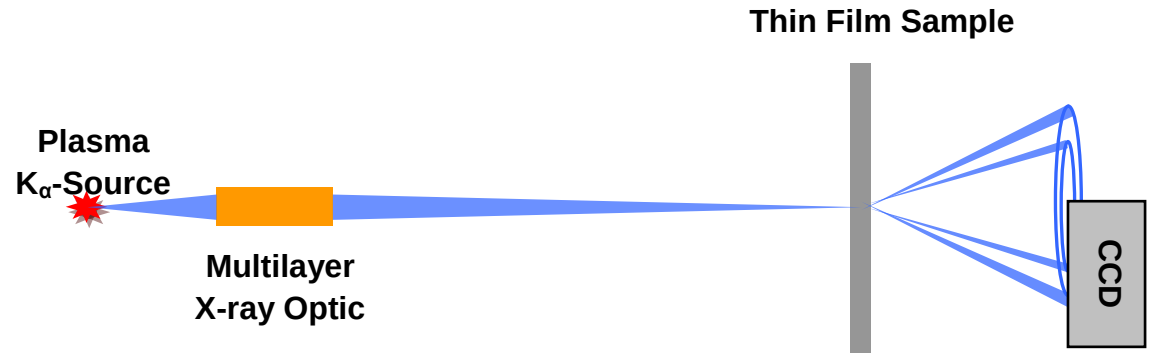

(a)

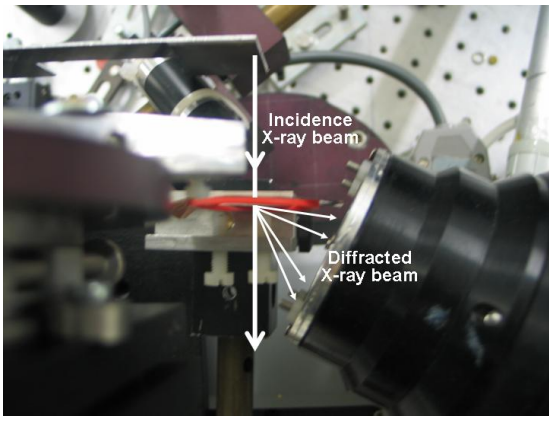

(b)

Au diffraction orders	$2\theta_{Bragg}$ [Deg]
111	38.19
200	44.39
220	64.58
311	77.58

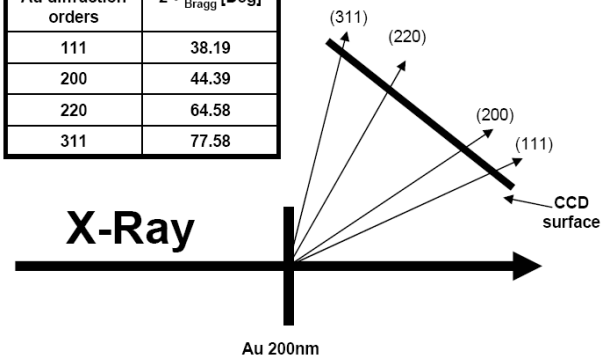

(c)

Fig. 6.1 Experimental configuration. (a) The principle schema of the experimental setup. (b) A photo of the arrangement of sample and X-ray area detector. (c) The configuration of the experiment for an Au sample.

A schematic of the experimental setup is shown in Fig. 6.1 (a). The femtosecond X-ray pulses are collected by the X-ray multilayer optic and focused on a polycrystalline thin film sample at normal incidence. Comparing to the experiments described in the previous chapters, no special alignment of the sample is necessary due to its polycrystalline structure. The diffraction pattern from the sample forms a series diffraction cones. Each diffraction cone corresponds to the diffraction from the same family of crystalline planes in all the participating crystallites. For the detection a large area detector is required to cover a sufficiently large angular range. In the experiment discussed here the phosphor-based, MCP amplified X-ray area detector (i.e. “Gemstar”) was utilized for this purpose. This camera has already been mentioned in chapter 3 and its working principle and detailed parameters are provided

in Appendix B. In order to simultaneously record as many diffraction orders as possible, the camera was placed not normal to the incident beam. Fig. 6.1 (b) presents a photo of the sample and camera arrangement. In Fig. 6.1 (c), the detectable diffraction orders have been depicted for Au as an example. Their corresponding diffraction angles are shown in the insert of Fig. 6.1 (c). Note that due to the limited size of the detector only parts of the different rings are recorded (see below).

6.2 Static Debye-Scherrer measurements

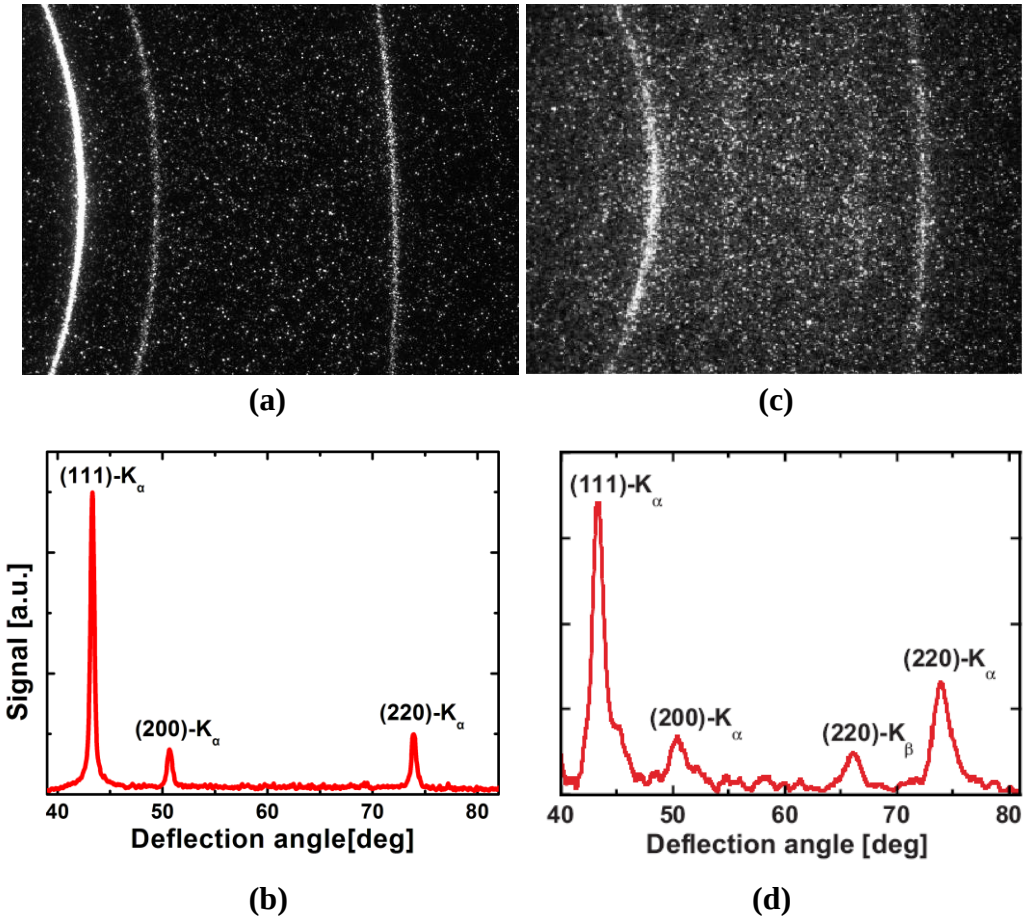

Fig. 6.2 Diffraction pattern of a 20µm polycrystalline Cu foil with Cu K_α X-ray source. The CCD images in (a) and (c) are obtained using multilayer optic and capillary optic, respectively. (b) and (d) are the radial cross section of image (a) and (c), respectively. (c) and (d) reproduced from Ref. [105].

In order to test the feasibility of the experiment and the capability of the setup, I first performed a (static) Debye-Scherrer diffraction experiment on a 20 µm thick Cu

foil. This sample was used in the above mentioned previous study with the elliptical capillary optic [105], and it provided sufficient diffraction signals to record the Debye-Scherrer diffraction pattern. Using the sample this time with the multilayer optic offered an opportunity to compare results obtained with different types of X-ray optics.

The detailed parameters of the experiment and the accessible diffraction orders of Cu with Cu K_α X-ray (8.05 keV) are provided in Appendix C. A typical Debye-Scherrer diffraction pattern obtained using the multilayer optic with 5 minutes exposure time is given in Fig. 6.2 (a). It can be seen that three different diffraction rings are detected simultaneously. These rings are the intersections of the diffraction cones and the detector plane. The shape of a complete ring, which can be a circle, an ellipse, a parabola or a hyperbola, depends on the angle of the detector plane with respect to the incoming X-ray beam. In order to derive the intensity of diffraction X-ray as a function of diffraction angle I(θ) from this CCD image, one needs to integrate the pixel intensity along the ring in which the pixels belong to the same θ. Thus a complete diffraction ring for a corresponding θ needs to be reconstructed. Considering that only small fractions of the rings are detected by the CCD, the curvatures of the detected parts are small enough to allow these ring patterns being reconstructed by approximating them as circles. As it can be seen in Fig. 6.3 (a), the coordinate origin is set at the middle of the left edge of the CCD image. By sampling the coordinates from each ring, their individual circle parameters (x_0 , y_0 and R) for a circle approximation ($(x-x_0)^2+(y-y_0)^2=R^2$) can be obtained. Knowing these parameters, the full ring pattern out of CCD plane for each diffraction order can be reconstructed. The zoom of CCD plane (Fig. 6.3(b)) presenting the well overlapping of X-ray and the reconstructed rings demonstrates feasibility of this reconstruction. With these circle fitting functions, the circle parameters (x_0 , y_0 and R) as a function of the x coordinate on the line y = 0 are obtained, as displayed in Fig. 6.3 (c). For each x coordinate (from 1 to 1392), a corresponding ring can be deduced. Each point (x,y) of the image belongs to one of these rings. By integrating the pixel intensity along

each ring and projecting all data on the line y = 0, the X-ray intensity as a function of x coordinate is obtained. Converting the pixel coordinate to the angular coordinate by applying the known angular positions of the corresponding detected diffraction orders, the diffraction X-ray intensity as a function of diffraction angle is finally derived. The result of this data processing for Fig. 6.2 (a) is given in Fig. 6.2 (b).

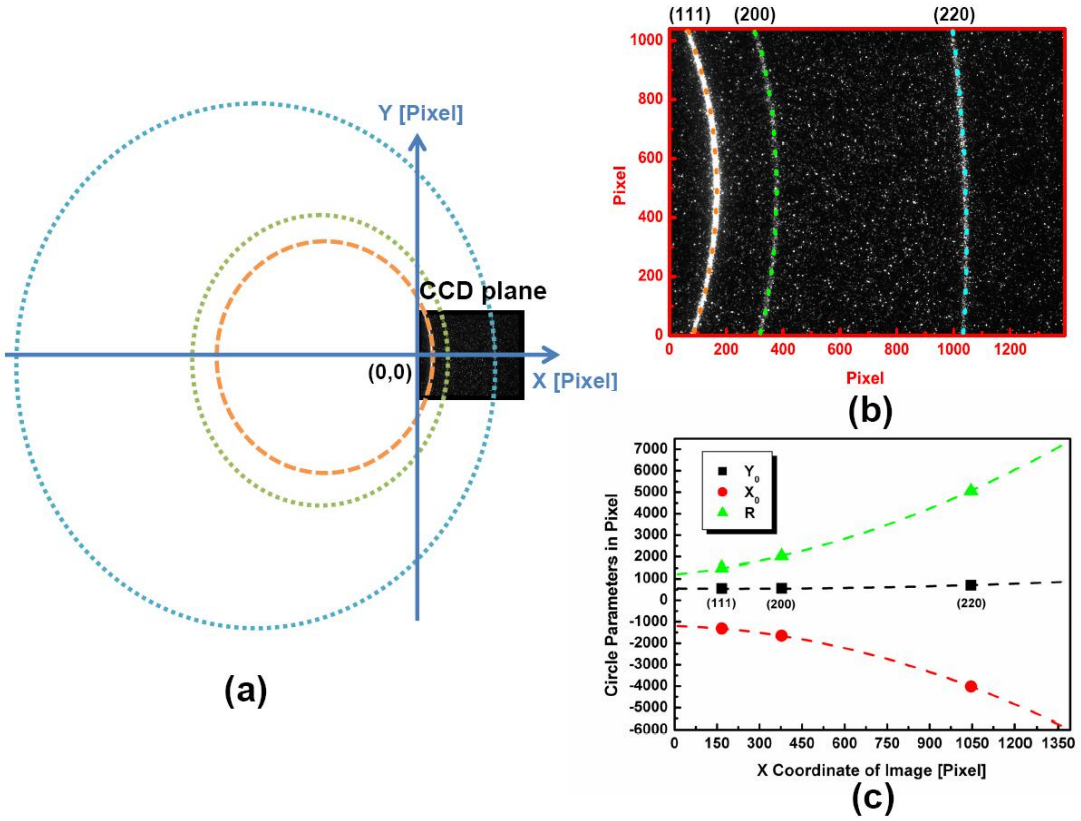

Fig. 6.3 Reconstruction of the diffraction pattern in order to extract the diffracted X-ray intensity as a function of diffraction angle. (a) Chosen coordinate system and the reconstructed ring pattern; (b) Zoom of the CCD image plane, showing the overlap of the measured diffraction pattern with the reconstructed rings; (c) Circle fit parameters (x_0 , y_0 and R) of each diffraction ring as a function of x coordinate on the y=0 line. The dashed lines are the 2nd order Polynomial Fit for the data points.

To compare my result with that obtained with a different kind of "collimating" X-ray optic, namely the elliptical capillary optics [105], a CCD image from this study and its radial profile are displayed in Fig. 6.2 (c) and (d). The elliptical capillary optics uses total reflection: All incident X-rays passing through the capillary with an angle smaller than the angle of total reflection undergo total reflection at its inner

surface. The angle of total reflection has a weak dependence on the wavelength of the X-rays and thus the optic is not wavelength sensitive. Therefore, more diffraction orders originating from K_α and also K_β radiation can be observed in Fig. 6.2 (c), instead of only three diffraction orders from the monochromatizing multilayer optics. The noisy background observed in Fig. 6.2 (d) is caused by the unfocused radiation passing directly through the capillary optic without reflection.

In conclusion, due to the monochromatic reflection of the multilayer optic and the optimized K_α flux of the laser-plasma source (see chapter 2), the modular setup can provide Debye-Scherrer diffraction patterns with much better signal-to-noise ratio than those obtained previously [105].

6.3 Time-resolved Debye-Scherrer experiment

The absorption depth of a metal at visible and near-infrared wavelengths is typically less than 20 nm [113]. However, multi-keV X-ray penetrate much deeper [189]. In particular with the transmission geometry used in this experiment, the 20 μm Cu sample presented in the former section is not a suitable sample to perform time-resolved experiments because it can not be effectively excited by the optical radiation over the whole depth probed by the X-rays. Therefore, in the experiments discussed in this section, a 200 nm thick free standing Au thin film [268] was used as sample to demonstrate the feasibility of time-resolved Debey-Scherrer diffraction.

6.3.1 Static Debye-Scherrer-diffraction pattern of the Au thin film

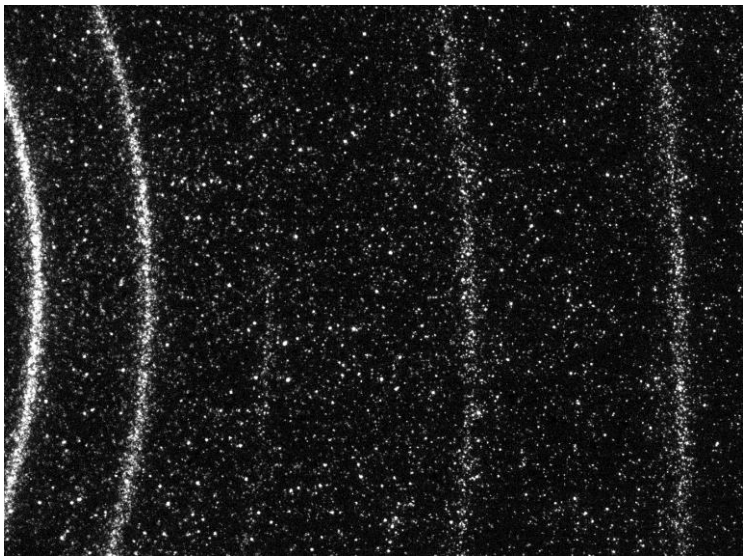

(a)

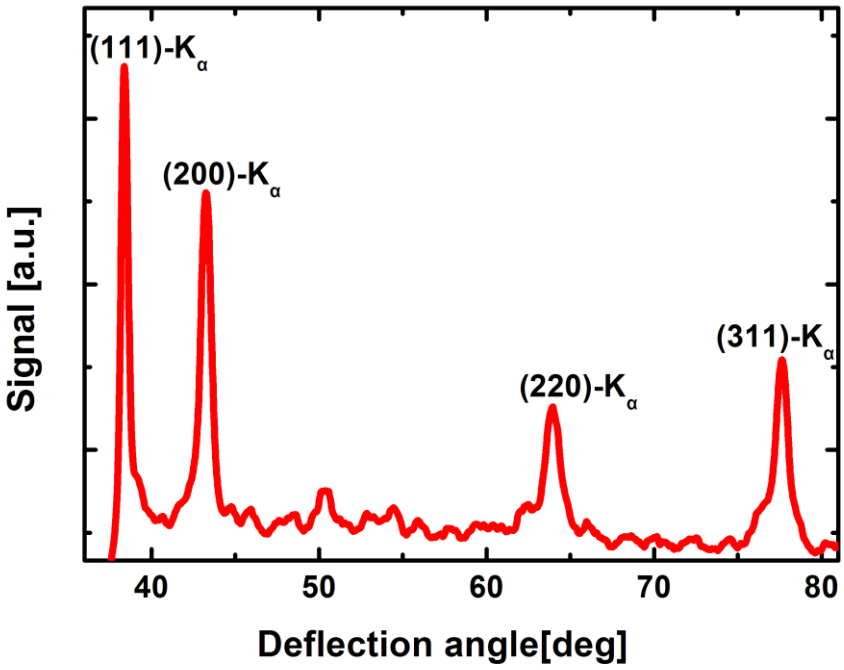

(b)

Fig. 6.4 Diffraction pattern of a 200 nm polycrystalline Au film. (a) CCD image. (b) Radial cross section of (a).

The detailed parameters of the experiment and the detectable diffraction orders

for Au are provided in Appendix C and Fig. 6.1 (c). The static Debye-Scherrer-diffraction pattern of the Au thin film is presented in Fig. 6.4 (a). Using a similar experimental configuration as described in the previous section, four diffraction orders were observed in this case due to the larger lattice constant of Au as compared to Cu. I(θ) is obtained in the same way as described in the previous section and shown in Fig. 6.4 (b). Compared to result with 20 μm Cu foil (Fig. 6.2 (b)), the signal-to-noise ratio becomes much worse. Such a difference is attributed to the small thickness of this sample: the total intensities of the diffraction peaks decrease with sample thickness, whereas the noise (background signal) coming from the scattering of X-ray are barely affected by the sample thickness.

6.3.2 Results of time-resolved pump-probe measurements

In the time–resolved measurement, the incident fluence of the pump beam was set to 160 mJ/cm^2 (wavelength 800 nm). The diffraction patterns were recorded using again the Phosphor-based X-ray area detector. An exposure time of 5 minutes had been chosen for each delay point. After subtracting the CCD background the images for a given delay were processed using a MatLab program (with the same routines described in section 6.2) to obtain I(θ)). By analyzing the transient changes of I(θ) , the laser induced changes can be deduced.

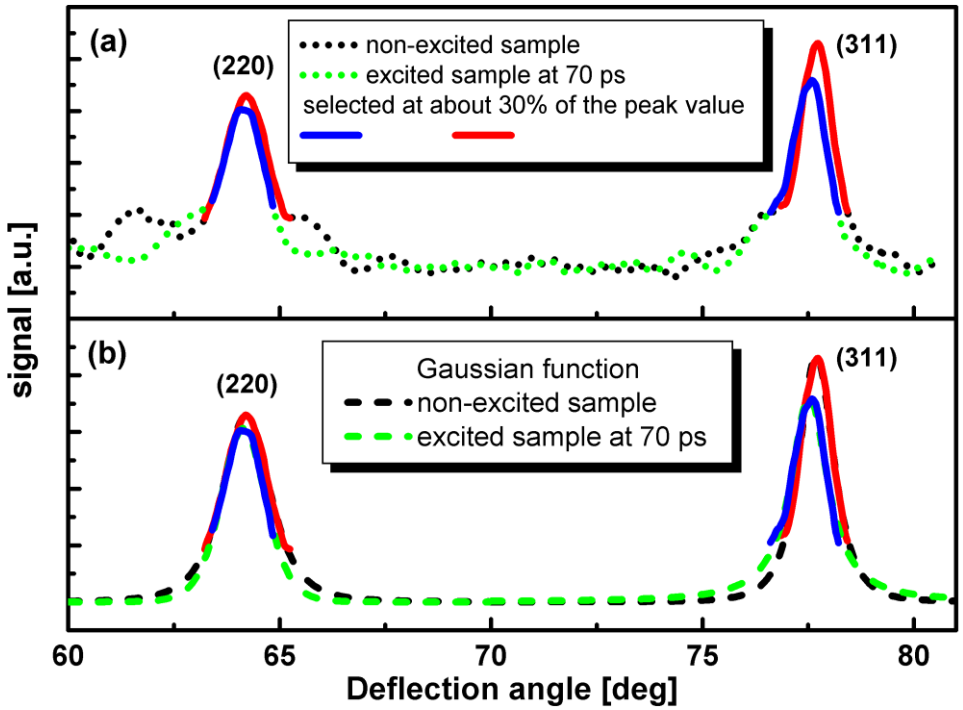

Fig. 6.5 Comparison of the signal from non-excited and excited Au sample. (a) Radial cross sections obtained from measured data. (b) The selected profiles above the noisy background (about 30% of the peak value) are fitted with Gaussian function.

It is known since many years that the excitation of a thin metal film with an ultrashort optical pump pulse leads to several effects, which can be observed with time resolved techniques [42, 75, 269, 270]. Generally, the changes of the diffraction intensity due to the Debye-Waller effect and the changes of the diffraction angle due to laser induced strain can be extracted from the measured time resolved data. Both effects have been discussed in Chapter 4. The amplitude of these changes is more pronounced for higher diffraction orders (see the discussion in section 4.2 and the latter discussion in section 6.3.3). Therefore, I focused in the analysis on the two highest diffraction orders, (311) and (220). Since the reduction of the diffraction intensity due to the Debye-Waller effect could not clearly be observed in these measurements, as will be explained in section 6.3.3, I will only discuss the observed changes in the angular position of the Bragg-peaks attributed to strain caused by acoustic waves.

The changes of the diffraction pattern induced by the optical excitation are

presented in Fig. 6.5 (a) where the I(θ)-data for the non-excited sample (black-dotted curve) and for a delay of 70 ps between the optical pump and the X-ray probe (green dotted curve) are shown. Shifts of both Bragg peaks are clearly observable. In order to quantify the shift, the two selected Bragg-peaks have been fitted using the Gaussian function. To eliminate any effects of the noisy background on the fitting, only data points with an intensity larger than 30% of the peak intensity (blue and red curves in Fig. 6.5) have been used for the fitting. The results are shown in Fig. 6.5 (b) as dashed curves and the peak positions and their error bars are obtained from the fitting parameters. Applying the same routine to all measured diffraction profiles, the peak positions as a function of delay time for the (311) and (220) Bragg reflections were obtained and are shown in Fig. 6.6.

Upon the laser excitation, pressure rises inside the sample, inducing strain. The resulting strain will modify the lattice constant of the sample and thus the radii of the diffraction rings. This is the origin of the transient peak shifts displayed in Fig. 6.6. For Au the energy will be rapidly (in a few hundred femtoseconds [211-213]) distributed after optical excitation, over the full 200 nm film thickness. Rarefaction waves are launched at both film surfaces and start to propagate into the bulk of the film. As a consequence the diffraction peaks start to shift to smaller diffraction angles indicating expansion of the material. After a time determined by the film thickness and the speed of sound of the considered material, the fronts of the strain waves traveling in the sample arrive at the opposite surface. For a free surface, the strain waves are totally reflected with a change of sign. Such recompression of the material is indicated by the diffraction peaks shifting back to larger diffraction angles without obvious damping effect. As already discussed in Chapter 4, the “triangular” shape of the time-traces results from a very fast and homogeneous (over the whole film thickness) increase of pressure in the sample upon optical excitation. [140, 186] The temporal position of the maxima and minima of the time traces in Fig. 6.6 (a) and (b) are determined by the transit time of longitudinal acoustic waves through the film. For both diffraction orders, oscillations with a half period of about (67 ± 1) ps are observed. Using the known sound velocity for polycrystalline Au of v_s = 3.24 km/s [271], this transit time

corresponds to a film thickness of 217 nm, which agrees within specifications (+/- 10%) of the manufacturer with the nominal thickness of 200 nm.

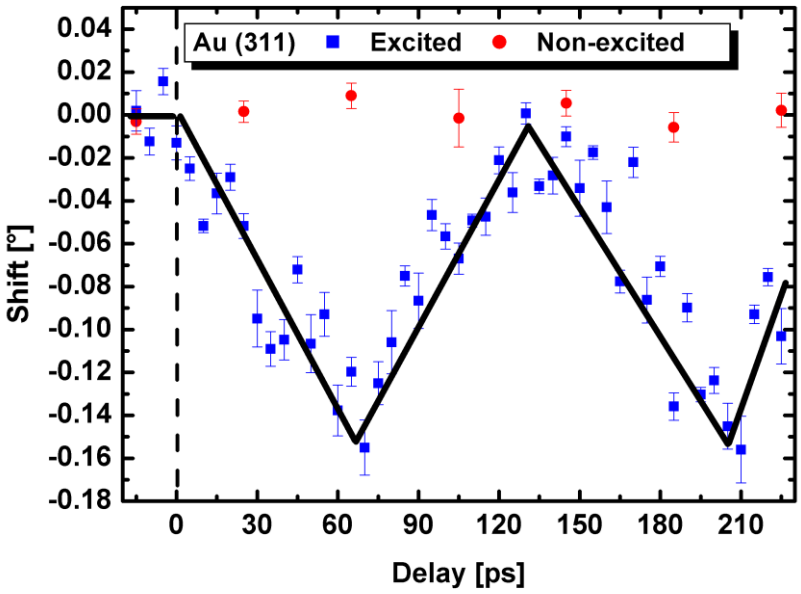

(a)

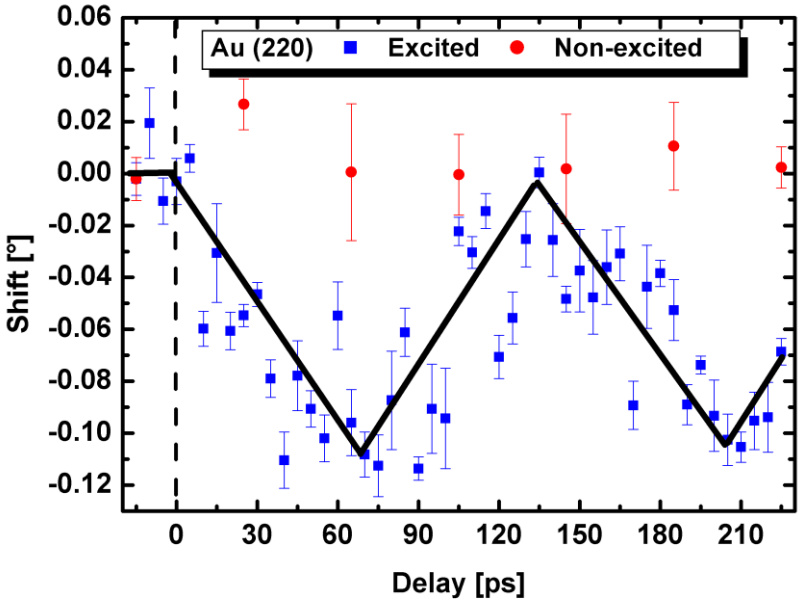

(b)

Fig. 6.6 Relative transient shift of the peak positions for the diffraction rings (311) (a) and (220) (b) after laser excitation (blue squares). The red circle points give the peak positions for non-excited sample. The black curves are guides for eye.

6.3.3 Modeling the transient behavior of the diffraction pattern after laser excitation

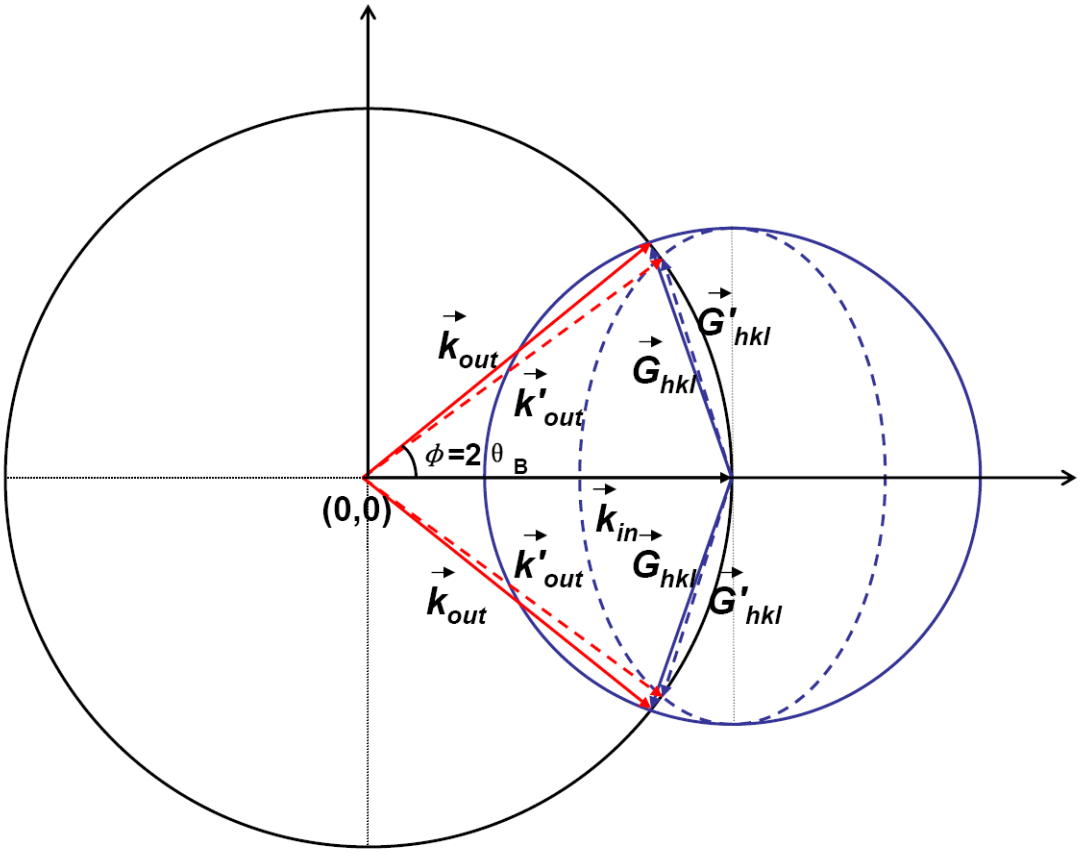

Fig. 6.7 Debye-Scherrer: Ewald-sphere construction without strain (solid circles) and with uniaxial strain (dashed circle).

In polycrystalline samples, the crystallites are randomly oriented. When the X-ray beam passes through the sample, only the crystallites with a plane orientation which fulfills the Bragg condition diffract X-rays. The diffraction contributions from all these crystallites form the Debye-Scherrer-diffraction pattern. When the sample is excited by the laser pulse with the condition that the illuminated area of laser is much larger than the sample's absorption depth, the sample expands only along the surface normal resulting in uniaxial strain. To understand the changes of the Debye-Scherrer pattern under uniaxial strain I use a Ewald-sphere-construction [272], as displayed in Fig. 6.7.

The black and blue solid circles are used to describe the situation in an

unstrained polycrystalline film. The black circle represents the Ewald-sphere. Its radius corresponds to the length of the wave vector of the incident X-rays. Since we are considering elastic scattering, the incoming wave-vector $\vec{k}_{in}$ as well as all possible wave vectors of diffracted waves have to lie on this sphere. The difference in direction is given by the reciprocal lattice vector $\vec{G}_{hkl}$. For a single crystalline sample $\vec{G}_{hkl}$ points only to one particular direction. For a polycrystalline sample all directions of $\vec{G}_{hkl}$ are possible. This is illustrated by the blue circle which has a radius corresponding to the length of $\vec{G}_{hkl}$. In two dimensions the two points of intersection mark the positions where the Bragg-condition is fulfilled. Extending this to three dimensions by rotation around $\vec{k}_{in}$ will transform the two points to a diffraction ring.

When the film is uniaxially strained/expanded, the length and direction of $\vec{G}_{hkl}$ depends on the orientation of the individual crystallite with respect to the surface normal and the circle (with direction-independent radius) transforms into an ellipse, which is represented in Fig. 6.7 by the blue dashed line. Its shorter axis corresponds to the direction of strain/expansion (larger lattice constant - smaller length of $\vec{G}_{hkl}$). Now the intersection of the ellipse with the Ewald-sphere defines the diffraction direction for the strained/expanded sample: As a result the diffraction rings should decrease their radius.

According to these considerations, a simple geometrical calculation allows to determine for a given strain what shifts will be induced for different Bragg peaks and these estimations can be compared to the experimental data. Choosing the center of the Ewald-sphere as coordinate origin, the black and the blue circle as well as the blue ellipse can be expressed as follows:

$$x^2 + y^2 = k^2 \tag{1}$$

$$(x-k)^2 + y^2 = G^2 \tag{2}$$

$$\frac{(x-k)^2}{(1-\eta)^2 G^2} + \frac{y^2}{G^2} = 1 \tag{3}$$

Where η is the uniaxial strain caused by laser excitation, defined as $\eta = \Delta d / d$ (d is lattice constant). Let (x_1,y_1) be the intersection point of the black and blue circles (unstrained case). In the strained case, the intersection point of black circle and blue ellipse change to $x_2 = x_1 + \Delta x$, $y_2 = y_1 + \Delta y$. Substituting x_1, y_1, x_2, y_2 and G from Eq. (1) and Eq. (2) in Eq. (3), and applying a first order approximation [$(1-\eta)^{-2} = 1 + 2\eta$, $\Delta x^2 \approx 0$, $\Delta y^2 \approx 0$], one obtains:

$$2(x-k)\Delta x + 2\eta(x-k)^2 + 2y\Delta y = 0 \tag{4}$$

Then substituting $x = k\cos\phi$, $y = k\sin\phi$, $\Delta x = -k\sin\phi\Delta\phi$, $\Delta y = k\cos\phi\Delta\phi$ in Eq. (4) one obtains the relationship between $\Delta\phi$ andη (and ϕ):

$$\Delta\phi = -\eta\frac{(\cos\phi - 1)^2}{\sin\phi} \tag{5}$$

Fig. 6.8 shows some results calculated using Eq. (5). The angular shift $\Delta\phi$ increases with strain η for a given diffraction order and for a given strain η, it is larger for higher diffraction orders.

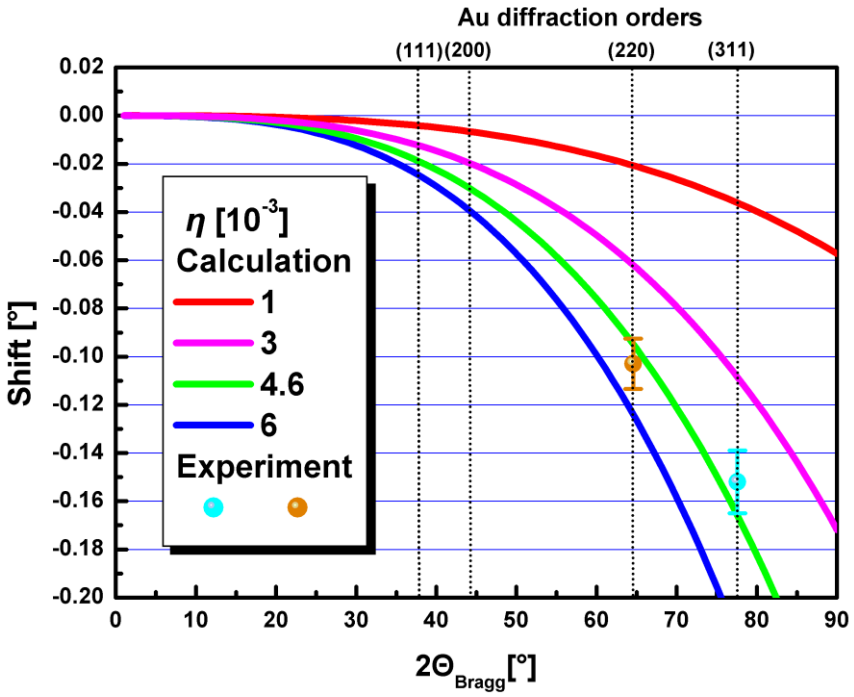

Fig. 6.8 Estimation of the shift of diffraction rings and comparison to measured data.

6.3.4 Discussion for the experimental results

Following the above discussion, the laser induced strain in the Au sample can be deduced from the angular shift of the diffraction peaks observed in the time-resolved experiment. The measured peak shifts are (- 0.152 ± 0.013) °and (- 0.103 ± 0.010) ° for the (311)- and (220)-reflection, respectively. Using equation (5), a strain of $\eta_{(311)}$ = (4.2 ± 0.4) ×10^{-3} and $\eta_{(220)}$= (5.0 ± 0.5) ×10^{-3} is derived. These two values agree within the error bars and can be used to estimate the sample temperature. For this we use the average value $\eta_{avg.} \approx$ (4.6 ± 0.5) ×10^{-3}. Since the lateral dimensions of the excited area (0.4 mm) are much larger than the film thickness, on the time scale of a few hundred picoseconds expansion of the film can only occur along the surface normal. Under these conditions, the relation between the peak strain and the laser-induced temperature increase is given by the following equation [223]:

$$\eta = \frac{6B\beta}{v_S^2 \rho} \Delta T \tag{6}$$

where B, β, ρ, v_s are the bulk modulus (B = 180 GPa), the coefficient of linear thermal expansion (β = 14.2 μm•m^{-1}•K^{-1}), the density (ρ = 19.3 g•cm^{-1}) and the speed of sound (v_s = 3.24 km/s), respectively. Equation (6) yields ΔT= (61 ± 7) K. This result is in rough agreement with the temperature increase (ΔT= (80 ± 11) K) estimated from the deposited energy in the sample for the given excitation fluence.

The Debye-Waller effect (see in Chapter 4) induced by this increase of temperature should lead to a 4.2% and 3.1% decrease in the integrated diffraction signal of the (311)- and (220)-reflection, respectively. However, due to the low diffraction signals (approx. 3 detected photons per second for the (311)-reflection; less for the (220)-reflection), these changes could not be detected in the experiment since they are of the same order (e.g. for (311)-reflection) or smaller (e.g. for (220)-reflection) than the experimental errors, which are mainly determined by counting statistics.

6.4 Summary

In this chapter, the static Debye-Scherrer-diffraction pattern of a Cu foil (20 μm) and an Au thin film (200 nm) have been presented. The feasibility of performing a time-resolved X-ray Debye-Scherrer measurement with the modular setup has also been shown. A preliminary time-resolved X-ray Debye-Scherrer measurement on a thin Au film has been preformed. The generation of acoustic waves due to rapid build-up of pressure upon laser excitation and their propagation inside the film has been followed by simultaneously measuring the transient shifts of the (311)- and (220)-reflection as a function of pump-probe time delay. The measured data are in good agreement with the behavior expected from propagation of acoustic waves in a 200 nm Au free standing film. A Ewald-sphere construction has been used to determine the strain induced by laser.

Finally, I would like to comment on the better accuracy achieved in the reported time-resolved powder diffraction experiment [106]. This is *not* related to properties of the X-ray source and the setup which are in fact quite similar (e.g. X-ray flux of the source). The essential point determining the different experimental accuracy is the samples under investigation. Comparing the thin film sample used here to the (organic) powder sample used in Ref. [106], the large penetration depth of pump beam in the latter one (up to a few tens of μm) allows much thicker samples to be used in the pump-probe experiments. Moreover, due to the large unit cell size (large lattice constant, small diffraction angles) and the use of a larger detector more diffractions orders and larger fractions of the complete diffraction rings could be recorded with the powder sample used in Ref. [106]. Only these sample properties provided diffraction patterns with a better signal-to-noise ratio, leading to a better experimental accuracy in the powder diffraction experiment.

7. Summary and outlook

7.1 Summary

This thesis describes my work on optimizing a femtosecond laser plasma K_α X-ray source, improving an existing modular setup for time-resolved X-ray diffraction experiments and several studies on ultrafast lattice dynamics in thin laser-excited metal films.

In the second chapter, the principles of ultrafast laser-plasma based X-ray sources are presented. A systematic investigation of optimizing the K_α X-ray source for time-resolved X-ray diffraction experiments was performed. The Cu and Ti K_α yield were studied as a function of different laser intensities, different angles of incidence and different controlled pre-pulse/pre-plasma conditions. The optimized conditions for both materials were determined. Introducing a controlled pre-pulse at an appropriate time in advance of the main pulse, the K_α yield can be enhanced to the same value no matter what angle of incidence is used. This result is valid for both materials under investigation. Due to the same required on-target intensity for the same K_α emission, better energy conversion efficiency is found at a small angle of incidence with a matching controlled pre-pulse. These experimental results agree well with estimations based on the classical resonance absorption mechanism and detailed Particle in Cell (PIC) simulations.

The third chapter describes the used modular setup for time-resolved X-ray diffraction and the implemented improvements. Applying the results discussed in the second chapter, the X-ray production has been improved. Two normalization methods are compared and discussed. The combination of "direct" normalization and

a “fast” delay scanning scheme represents the most efficient way to achieve high measurement accuracy.

By using the optimized setup presented in Chapter 3 the Debye-Waller effect in a thin laser-excited Au film was observed. The experimental results are presented in chapter 4. For high excitation fluences, an exponential drop of the measured diffraction signal with a decay time constant of 4.3 ps is measured. This result is in good agreement with previous experimental results as well as the Two-Temperature Model (TTM) calculations at high fluences. As the first time-revolved experiment performed with the improved modular setup, these observations also underline the capabilities as well as the restrictions of the modular setup.

The fifth chapter focuses on investigating coherent optical phonons in Bi after intense laser-excitation. Large amplitude coherent motion of atoms and a softening of the A_{1g} phonon mode were observed. At lower fluences, the measured results agree perfectly with earlier results obtained at the Sub-Picosecond Pulse Source (SPPS) and University Duisburg-Essen (UDE). Upon strong excitation (absorbed laser fluences > 2 mJ/cm^2), a further softening of the A_{1g} mode is observed. At fluences between 3.1 and 3.3 mJ/cm^2, a complete softening of the A_{1g} mode is found. This observation strongly indicates that the Peierls distortion, which defines the equilibrium structure of Bi, vanishes and the material is transformed into a transient ordered state of higher symmetry. At even stronger excitation (absorbed laser fluences > 3.3 mJ/cm^2), the atomic motion becomes a Brillouin-zone boundary acoustic phonon mode and this mode stiffens. The observations follow qualitatively the predictions of calculations based on density functional theory.

The sixth chapter is dedicated to time-resolved X-ray Debye-Scherrer diffraction measurements. The presentation of static Debye-Scherrer diffraction pattern of Cu (20 μm) and Au (200 nm) showed the feasibility of performing time-resolved X-ray Debye-Scherrer diffraction experiments with the modular setup. In the time-resolved measurements on a Au thin film, the generation of acoustic waves and their propagation inside the film had been observed through the transient shifts of the (311)- and (220)-reflection. The temporal evolution of the measured data is in good

agreement with the behavior expected from propagation of acoustic waves inside the 200 nm free standing film. A simple model based on a Ewald-sphere construction has been used to determine the laser-induced uniaxial strain from the measured time-resolved Debye-Scherrer patterns.

7.2 Outlook

As it has been underlined in this thesis, the modular setup using the laser-plasma-based X-ray source is still of great interest for performing time-resolved X-ray diffraction experiments, due to its availability and low cost (in comparison to accelerator-based sources). The following technical developments can be done to improve the performance of the modular setup and open possibilities for new types of experiments.

1) The conditions to optimize the X-ray output have been discussed in detail in this thesis. Redesign of the source chamber allowing a smaller angle of incidence of the drive laser for the X-ray source could be an option to fulfill the optimized condition with less energy requirements to the laser system.

2) Improving the overall stability is another important issue for the source. This requires improvement of the stability of the laser system as well as the mechanical parts of the tape target pulling system.

3) An automatic optimization/stabilization of the X-ray output behind the multilayer optic during experiments can be realized by an automatic adjustment of the position of the X-ray source point on the tape target through motorized actuators. To carry out this function, the manual actuators of several mirrors in the setup should be replaced by motorized actuators, and a control program should be developed and integrated into the main experiment control program.

4) The current sample holder with manual adjustments should be replaced with a motorized one. It should definitely improve the accuracy of the adjustment and also save time. Additionally, this would allow to perform irreversible time-resolved X-ray diffraction experiments, e.g. on laser-induced melting, with the modular setup.

5) The results of the time-resolved X-ray Debye-Scherrer diffraction measurements presented in this thesis successfully proved the possibility of performing Debye-Scherrer type measurements with the laser plasma X-ray source. As single crystalline samples are not required in this scheme, a much wider range of materials, which are not easily available as single crystals, can be studied now. In order to further improve the experimental accuracy (which directly relates to the number of detected photons) for this type of experiments, a new camera with large detection area [273] has been implemented in the setup and tested by F. Quirin. Once suitable samples with sufficient diffraction signal are obtained, further investigations could be made with this setup.

Since the electronic properties of the material are strongly affected by lattice structure, the laser-induced reversal of the Peierls distortion in Bi should lead to corresponding changes in its electronic band structure, resulting in a semimetal to metal phase transition. Investigation of this phase transition process can be one of the most interesting subjects for Bi. To study the electronic dynamics, it requires techniques which are sensitive to the electronic structure, e.g. time-resolved X-ray absorption spectroscopy (t-XAS) [274-276], time-resolved angle-resolved photoelectron spectroscopy (t-APRES) [277] and time-resolved THz spectroscopy [278-280].

Another interesting topic on Bi is to observe the coherent E_g motion with X-ray diffraction. The excitation of the E_g mode has been demonstrated in many ultrafast optical experiments [247, 281], which do not provide direct, quantitative information on the vibrational dynamics. These dynamics can be retrieved directly with X-rays and provide quantitative information about the amplitude of the E_g motion, as well as the coupling behavior between A_{1g} modes and E_g modes. Up to now, only one study on this topic has been performed at the Swiss Light Source (SLS) [282]. To completely understand the *displacive excitation of coherent phonons* (DECP) mechanism and the subsequent phonon dynamics, more knowledge on the E_g motion is required. The extension of this study should be continued.

In recent years, sub-picosecond time-resolved X-ray diffuse scattering technique became available. This technique gives information on the phonon population

throughout the Brillouin zone, and can yield the phonon dispersion [283]. Applying this technique to investigate the phonon softening behavior in Bi must be an interesting subject in the near future. However, this technique requires large photon flux, and is not possible to be carried out with the current laser plasma sources due to their low X-ray output. The appropriate X-Ray Sources are the new X-ray free electron lasers like LCLS (USA), SACLA (Japan) or the later XFEL (Germany).

Appendixes

A. Working principle of multilayer mirror

A multilayer optic is an artificial, two dimensional crystal. The spacing of the multilayers is designed for specific radiation to satisfy Bragg's diffraction law. As shown in Fig. A.1, the incident X-rays are reflected by diffraction at a series of interfaces between layers with differing indices of refraction. Only the wavelength of interest is effectively reflected, others which do not satisfy the conditions for Bragg reflection are absorbed in the mirror and are not reflected, thus allowing the mirror to produce a highly monochromatic beam.

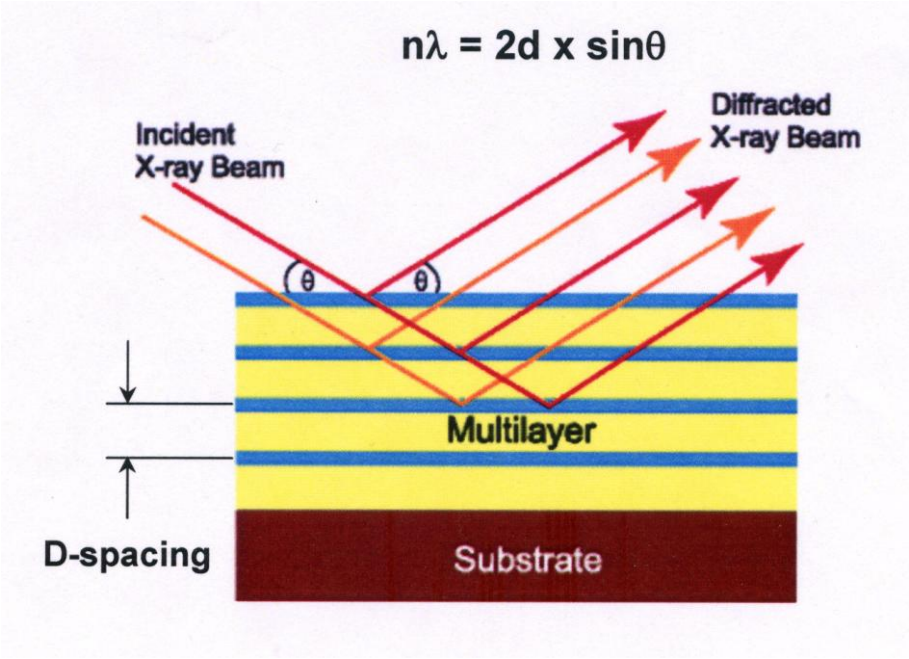

Fig. A.1 Multilayer working principle. Reprint from the manufacturer [284].

The focusing multilayer mirrors are realized by curving the mirror surfaces into either parabolic or elliptical shapes. The d-spacing (thickness of a single bi-layer) of the multilayer coating is controlled along the mirror surface to satisfy Bragg's law at every point (Fig. A.2). The band-pass of a multilayer optical system can be further controlled by using different materials and layer configurations for various applications.

The multilayer X-ray optic used in the X-ray modular setup is two–dimensional reflection systems, which is realized by using two VariMax^{TM} multilayer X-ray

mirrors in a "side-by-side" *Montel-Helios* scheme (Fig. A.3) [188]. These two mirrors are placed perpendicularly. Each mirror independently reflects x-rays in one of the two perpendicular directions. With the "side-by-side" scheme, both mirrors may be positioned at a location appropriate to optimize performance parameters including flux, spectrum and divergence by adjusting four motorized actuators on the housing. Once the mirrors are adjusted, the exact position of the X-ray point source and the focus are defined.

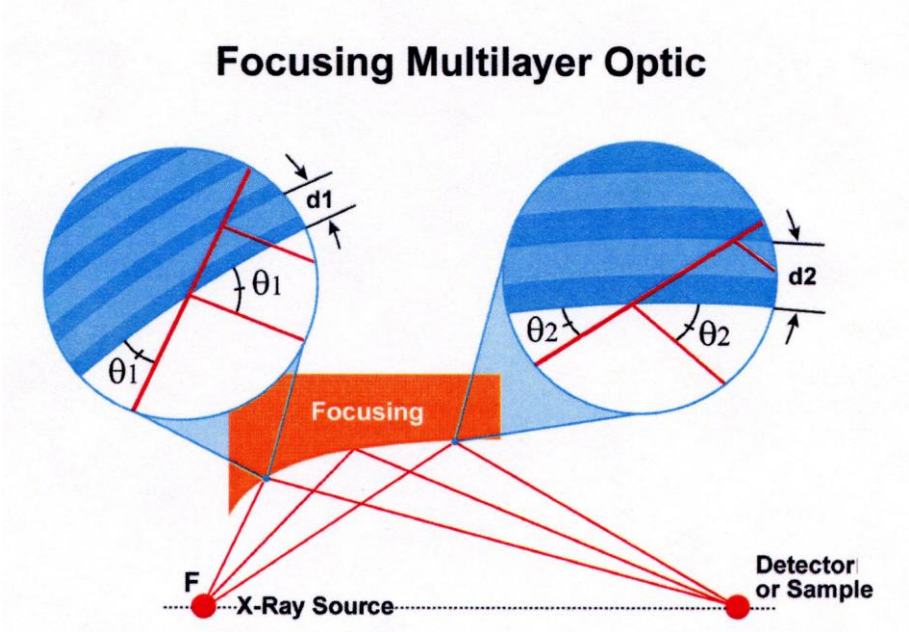

Fig. A.2 Graded d-Spacing Multilayer for focusing. Reprint from the manufacturer [284].

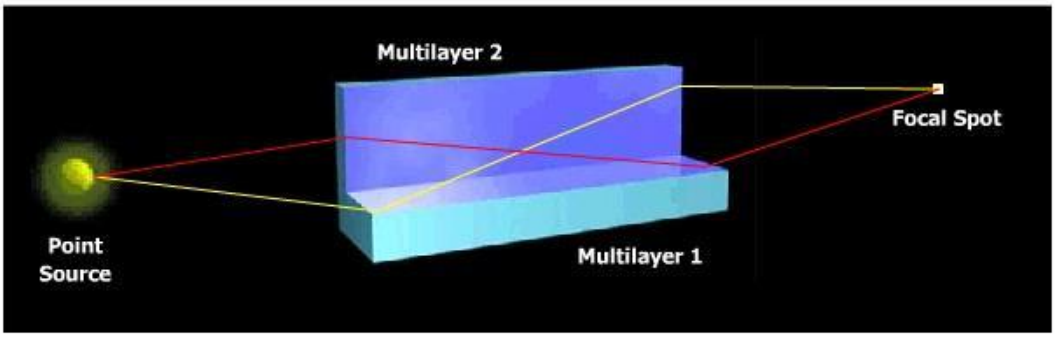

Fig. A.3 Scheme of the Montel-Helios configuration. Reprint from the manufacturer [284].

The multilayer X-ray optic prepared for the modular setup is produced by Rigaku-OSMIC Inc.. The Specifications provided by the manufacturer are shown in table A.1.

Parameters (units)	CMF10-50Cu12
Characteristic line	Cu K_α
Wavelength (Å)	1.54
Effective focal spot size (mm)	0.01
Length of the mirror (mm)	120
Focal spot – mirror distance (mm)	100
Focal spot – sample distance (mm)	600
Bragg angle in the middle point (degree)	0.97
Reflectivity Kα (parts)	0.84
Rocking curve width (arcmin)	1.98
Capture angle (rad)	0.0264
(degree)	1.5133
Convergence angle (rad)	0.0043
(degree)	0.24
Focal spot usage efficiency (parts)	0.96
Beam width at mirror (mm)	2.64
Beam width at the optic entrance (mm)	1.06
Beam width at the optic exit (mm)	1.87
Beam width at the focus (mm)	0.094
Optic efficiency (a. u.) (Reflectivity * Solid angle)	0.00045
Geometric magnification:	1:5
Ravg ²(for double reflection) (%)	75
Distance X-ray source–entrance of housing (mm)	30

Table A.1 Specifications of the Cu K_α multilayer optic provided by the manufacturer Rigaku-OSMIC Inc.. Reprint from Ref. [186].

B. X-ray detectors for diffracted signals

B. 1. Direct detection camera

The Roper Scientific Pi-MTE: 1300B from Princeton Instruments is an innovative, high-sensitivity imaging system designed to operate inside high-vacuum chambers over long operation times. The Pi-MTE: 1300B incorporates a back-illuminated CCD without AR coating for ultra-low-energy X-ray detection. With 20×20 μm pixels and 100% fill factor, this system offers a large imaging area with very high spatial resolution and dynamic range. The thermoelectrically cooled design features PCBs, thermally linked to the circulating coolant to provide reliable operation inside vacuum chambers. Its detail specifications are given in Table B.1. This camera is suitable for monitoring hard X-ray radiation due to its good quantum efficiency, e.g 55% for Ti K_α and 18% for Cu K_α. (Fig. B.1).

As a direct detection camera, the incidence photons are directly absorbed by the active area of CCD pixels, and generate charge signals. The charge signals are strictly

proportional to the incident phonon energy. For example the camera used here have conversions that one Ti K_α (4.51 keV) photon gives a signal of ~589 counts, and one Cu K_α photon (8.05 keV) gives a signal of ~1050 counts. In high flux condition (>10^4 detected photons per pulse), the detected photon number can be easily deduced from the value of integral signal (see in section 3.1). In low flux regime (for example, 1 detected photon per 40 pixels), this camera can also be used as a multi-channel energy detector. A histogram of the CCD image corresponding to the energy spectrum can be obtained [142], and the number of detected photons can easily be deduced from this histogram. This function has been applied in the measurement of X-ray source production in Chapter 2. Here, one should notice that when the histogram is used to calculate the detected photon number, the multi- pixel event issue should be taken into account.

CCD image sensor	PI Exclusive: Scientific-grade, back-illuminated, MPP device without AR coating		
CCD format	1340 x 1300 imaging pixels 20 x 20 µm pixels 100% fill factor 26.8 x 26.0 mm imaging area (optically centered)		
	MINIMUM	TYPICAL	MAXIMUM
Linear full well	130 ke-	200 ke-	
Output amplifier	130 ke-	250 ke-	
System read noise @ 50 kHz digitization @ 100 kHz digitization @ 200 kHz digitization @ 500 kHz digitization @ 1 MHz digitization @ 2 MHz digitization		 3 e- rms 4 e- rms 6 e- rms 8 e- rms 10 e- rms 15 e-rms	 4 e- rms 6 e- rms 8 e- rms 13 e- rms 15 e- rms 25 e-rms
Dark current @ -40°C operation		0.1 e-/p/s	0.5 e-/p/s
Deepest cooling temperature TE (chilled liquid)	-40°C	-45°C	-50°C
Vacuum Compatibility		10^{-4} Torr	10^{-6} Torr*
Nonlinearity @ 100 kHz	2%		
Readout bits / speed	16 bits @ 50kHz to 2MHz		
Parallel shift rate	48 µsec/row		

Table B.1 Specifications of Roper camera. Reprint from the technical datasheet [285].

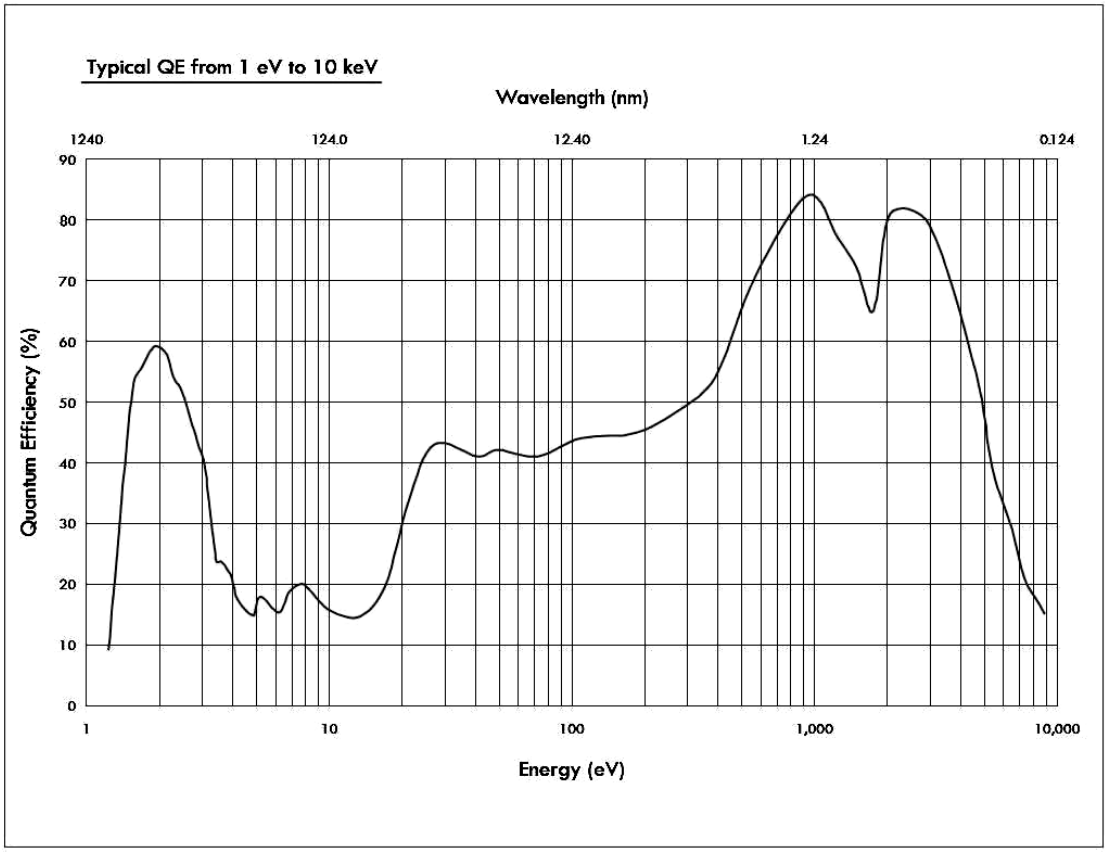

Fig. B.1 Quantum efficiency of Roper camera. Reprint from the technical datasheet [285].

Two major limitations of operating this camera should be pointed out. The first one is its working condition. During the acquisition of a picture, the charged coupled device (CCD) will accumulate not only the signal from detected photons but also the signal due to the dark current. The dark current depends strongly on the temperature on the detector. Cooling down the detector is the typical way to reduce it. In the experiment, the working temperature of the camera is -30 °C, which is realized by an integrated Peltier cooler under the chip. Due to this low temperature, to protect the CCD from ice formation on the cooled parts, the CCD chip should maintain under vacuum. It can be easily achieve in a big vacuum chamber, for example, in the experiment of Chapter 2. For the modular setup, the device needs to be operated in air. Additional configuration for keeping the vacuum inside the camera has been made. A special vacuum nose which isolates only the CCD has been installed into the camera. The nose needs to be continuously pumped to insure the required vacuum. An Al plate with a hole of approximately 1 cm^2 covered by Beryllium window is installed at

the input of the camera, which leads to only 1/4 of CCD size is available for the exposure. The second drawback of this detector is its rather slow readout time. For full size chip information, it needs 17 seconds to read out the data. The readout time can be reduced for small regions of interest, but it still remains more than 100 ms, and because of this, the Roper camera can not be used with a 10 Hz repetition mode to record each single X-ray pulse.

B. 2. Indirect detection camera

Pixel Resolution:	1392 ×1040 (4:3 aspect ratio)
Effective pixel size at input:	23 microns square
Active input size:	32 ×24 mm (40mm diagonal)
Intensifier:	Ultra high-resolution (typically > 60lp/mm) low noise
Intensifier format:	40mm diameter
Intensifier input window:	Coherent fiber optic
Gating:	Gated on when CCD is integrating, off when not acquiring
Gating speed:	Minimum gate period approx. 100ns
Coupling to scintillators:	Via coherent straight fiber-optic
Scintillator material:	Gadolinium Oxysulphide, 7.5mg/cm^2
Grey Scale Resolution:	4096 grey levels (12bits)
Readout speed:	20 MHz or 10 MHz pixel rate software selectable
Linearity:	No measurable deviation from linear response until saturation
Saturation:	Approximately 13000 electrons
Video Gain:	User variable in software in 100 setups
Intensifier Gain:	User variable in software in 100 setups
On-chip binning:	User selectable 1 × 1to 63 × 63
Exposure Time:	User selectable from 100μsec to 30 minutes
Readout Philosophy:	Correlated double sampling for highest accuracy, fast 12 bit A/D converter in head, producing LVDS differential format
Control:	PS Link 4 Line bi-directional Serial interface. Using LVDS drivers for reliability over long cables. Parameters that can be adjusted include image intensifier gain, video gain, CCD integration period, binning, and sub-area window.
Power Requirements:	110 or 230V ac 50/60Hz
Operating Environment:	Temperature – Storage: -10 to +80 ℃ Operation: 0 to +50 ℃ Humidity – 0-80% RH non-condensing

Table B.2 Specifications of Gemstar camera. Reprint from the user manual [273].

The Gemstar Camera from Photonic Science is an indirect detection camera. Its specifications are given in Table B.2. The main feature of the indirect X-ray detection is using a scintillator to transform the incoming signal into an optical signal which can be easily detected and recorded. This allows the quantum efficiency of certain wavelengths, like Cu K_α to be optimized by choosing an appropriate material. The scintillator inside this camera is made of a polycrystalline layer of Gadolinium Oxysulphide, which has a quantum efficiency of 85% for Cu K_α radiation. When incident photons are absorbed, the scintillator emits photons in the visible range. A straight fiber-optic is used to couple them into the photocathode of the intensifier. These incoming photons produce photoelectrons from the photocathode. The produced electrons are sent through a multi channel plate (MCP) for a further step amplification. The amplification of MCP can be changed in the control software. By triggering the MCP by a camera trigger signal or an additional gate signal, the amplifying process can only be active for a short period during the presence of the X-ray pulse, therefore increasing the signal to noise ratio by reducing the background signals. This method could be very useful when multiple exposures of the Bragg peaks are required. After amplified by MCP, the outcoming electrons hit on a phosphor screen and produce phosphorescence, whose intensity is proportional to the number of incident electrons. This light emitted from the screen is then collected by a tapered fiber optic and sent onto a CCD sensor cooled by a peltier cooler, which allows images to be acquired with extended integration periods with minimal build-up of CCD dark current. This whole process allows the camera to work with a repetition rate of 10 Hz when the On-Chip binning is set to large than 4×2 binning or a small region of interest is selected. This camera can record a sequence of pictures containing every single X-ray pulse per picture.

A major limitation of this camera is that it can not provide any information about the energy of the incoming X-ray photons due to several conversion processes, and unlike a direct detection camera it can not be used for obtaining the energy spectrum from a histogram of the image. This type of camera is useful when the incoming

photons are monochromatic. In this case, the average signal from the chip can be correlated with the average number of incoming photons.

B. 3. Avalanche Photodiode (APD)

CHARACTERISTIC	TEST CONDITIONS	MIN	TYP	MAX	UNITS
T_O (Operating Temperature)		+1		+40	℃
T_S (Soldering Temperature)				+240	°C
V_{TEC} (TEC Voltage)				4.3	V
I_{TEC} (TEC Current)				2	A
P (APD Die Power Diss.)				0.2	W
I_D (Dark Current)			15	35	nA
C_J (Junction Capacitance)	f = 1MHz		50		pF
λ_{range} (Spectral Application Range)	Spot Scan	350		1050	nm
R (Responsivity)	λ=500nm, V_R=0V		35		A/W
V_{op} (Operating Voltage)		1700		2000	V
t_r (Response Time)	RL=50Ω,λ=675nm		12	18	nS
I_{QTEC} (TEC Quiescent Current)	Case Temp = 35 ℃		0.95		A

Table B.3 Specifications of APD. Reprint from the technical datasheet [286].

The avalanche photodiode is essentially a solid-state equivalent of PMTs (photon-multiplier tubes) and can replace vacuum tube technology with compact, rugged, silicon devices in many applications. It is one of options for monitoring diffracted X-ray signal, if only the integrated signal is interesting. A cooled large area silicon avalanche photodiode produced by Laser Components, which is assembled with a homemade amplifier circuit, is used for the modular setup. Its specifications and spectral response at visible light range are given in Table B.3 and Fig. B.2, respectively.

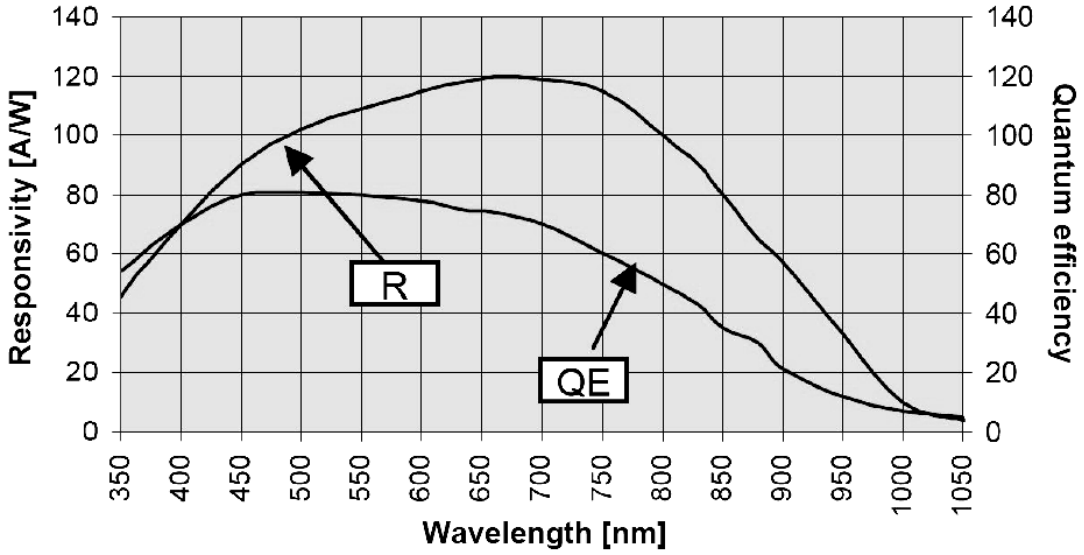

Fig. B.2 spectral response of APD at Gain = 300. Reprint from the technical datasheet [286].

One of the advantages of this detector is that it can work at very high speed, fast enough to synchronize to the 10 Hz laser system. Another advantage of APD is that it has single photon sensitivity, which allow to detecting weak signal and estimating the number of detected photons. However, as a single channel detector, the obvious drawback of APD is that it gives no information on spatial resolution. Shifts or changes of profile of the Bragg peaks can not be observed with this detector during the measurement. It limits the use of the APD only in the experiments in which the profiles of Bragg peaks do not change a lot during the laser excitation.

C. Sample material properties

The following relevant material parameters are used in this thesis. They are obtained from literatures, WebElements (http://www.webelements.com/), X-RAY SERVER (http://sergey.gmca.aps.anl.gov/x0h_search.html), and X-ray Oriented Programs (XOP) (http://www.esrf.eu/computing/scientific/xop2.1/).

C. 1. Cu

Name: copper

Symbol: Cu
Number: 29
Standard atomic weight: 63.546
Electron configuration: [Ar] $3d^{10}$ $4s^{1}$
Electrons per shell: 2, 8, 18, 1
Density : 8.94 g cm^{-3}
Crystal structure: face-centered cubic
Melting point: 1358 K
Specific heat capacity (25 ℃): 24.440 J mol^{-1} K^{-1}
Bulk modulus: 140 GPa
$K_{\alpha 1}$: 8047.78 eV, λ = 1.54060410 Å
$K_{\alpha 2}$: 8027.83 eV, λ = 1.54443266 Å
K_{β}: 8905.29 eV, λ = 1.39225593 Å
Sample thickness: 10 μm, 20 μm foil and 300nm thin film on glass substrate

C. 2. Ti

Name: titanium
Symbol: Ti
Number: 22
Standard atomic weight: 47.867
Electron configuration: [Ar] $3d^{2}$ $4s^{2}$
Electrons per shell: 2, 8, 10, 2
Density : 4.506 g cm^{-3}
Crystal structure: hexagonal
Melting point: 1941 K
Specific heat capacity (25 ℃): 25.060 J mol^{-1} K^{-1}
Bulk modulus: 110 GPa
$K_{\alpha 1}$: 4510.84 eV, λ = 2.74858848 Å
$K_{\alpha 2}$: 4504.86 eV, λ = 2.75223711 Å
K_{β}: 4931.81 eV, λ = 2.51397415 Å
Sample thickness: 20 μm foil and 300nm thin film on glass substrate

C. 3. Au

Name: gold
Symbol: Au
Number: 79
Standard atomic weight: 196.966569
Electron configuration: [Xe] $4f^{14}$ $5d^{10}$ $6s^{1}$
Electrons per shell: 2, 8, 18, 32, 18, 1
Density : 19.30 g cm^{-3}

Melting point: 1337.33 K
Specific heat capacity (25 ℃): 25.418 J mol^{-1} K^{-1}
Speed of sound: 3.24 km/s (polycrystalline)
3.39 km/s (single crystalline, 111-direction)
Linear thermal expansion (25 ℃) 14.2 μm m^{-1} K^{-1}
Thermal conductivity (300 K) 318 W m^{-1} K^{-1}
Optical constants: n=0.181, k=5.125 @ 800 nm

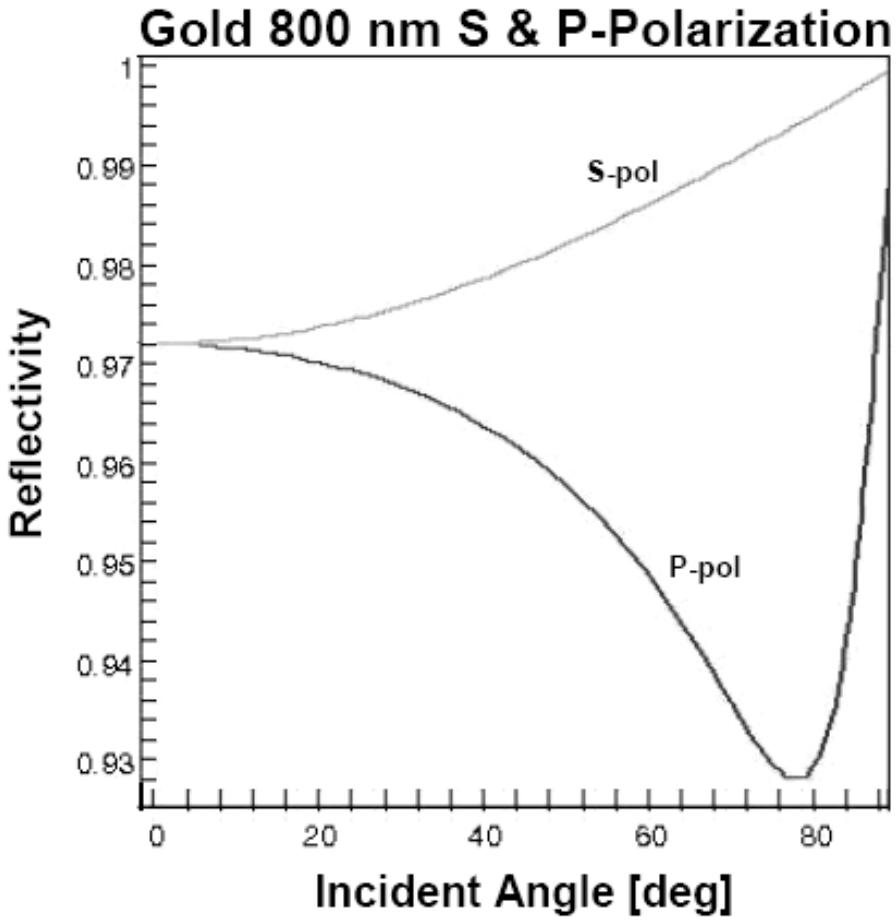

Fig. C.1 Reflectivity of Gold at 800nm, calculated from Fresnel equations.

Sample thickness: 150nm on mica substrate and 200nm free standing film
Crystal structure: Lattice face centered cubic
Symmetry group: Cubic
Unit cell constant: a = b = c = 4.0782 Å.
Unit cell angles: $\alpha = \beta = \gamma = 90°$
X-ray wavelength: 1.540562 Å
X-ray energy: 8.047984 keV
X-ray characteristic line: Cu-$K_{\alpha 1}$
Surface plane indices: (1 1 1)

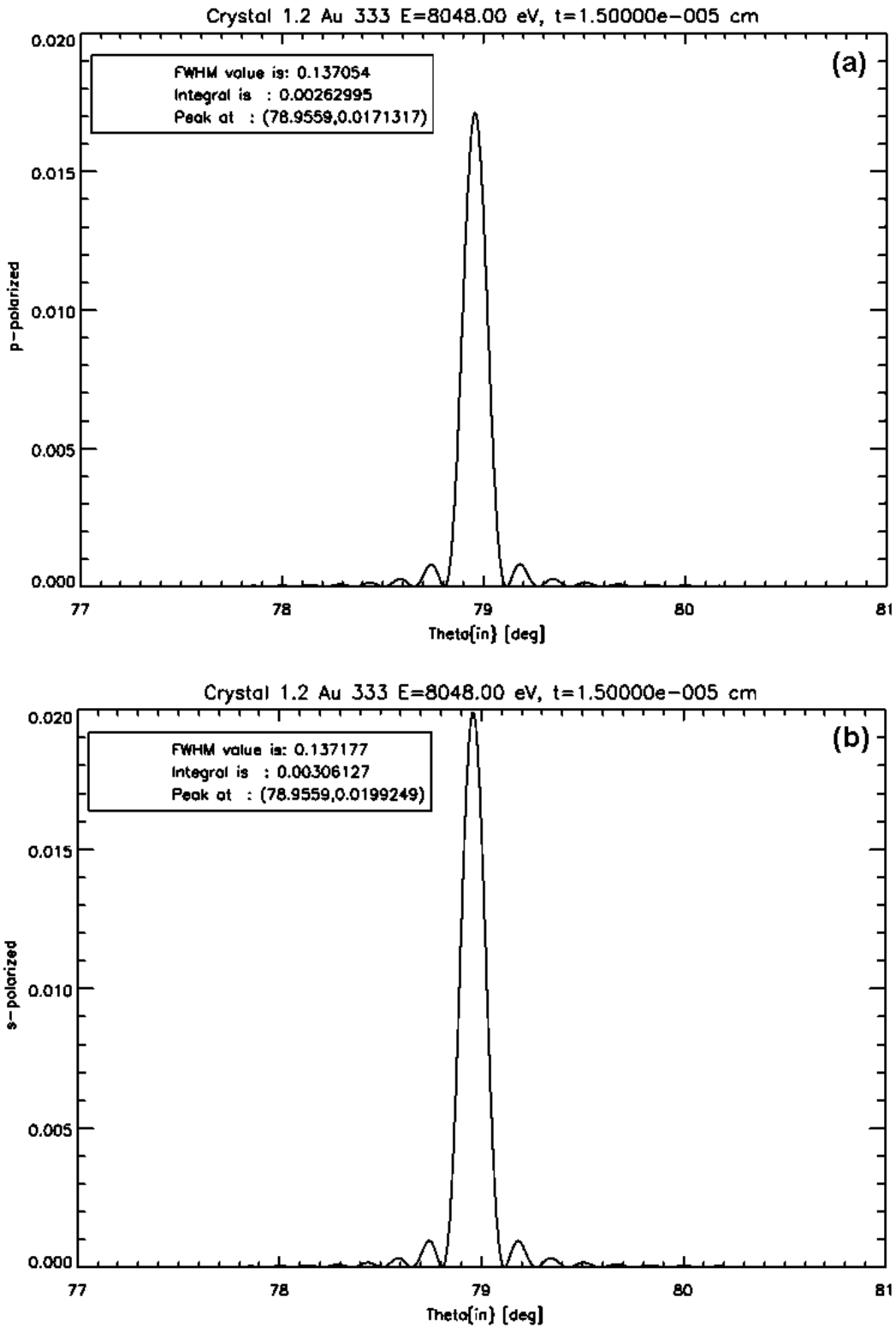

Fig. C.2 Bragg reflection of Au (333) calculated from XOP. (a) P-polarized beam and (b) S-polarized beam.

Planes found: 9. Planes being displayed: 9

hkl	Angle to surface	Bragg angle	Relative Intensity xh/x0(%)
(1 1 1)	0.0049	19.0956	82.4245
(1 1 3)	29.4962	38.7877	62.6630
(1 3 1)	29.4962	38.7877	62.6630
(1 3 3)	22.0017	55.4164	52.6226
(2 2 2)	0.0049	40.8660	61.0997
(3 1 1)	29.4962	38.7877	62.6630
(3 1 3)	22.0017	55.4164	52.6226
(3 3 1)	22.0017	55.4164	52.6226
(3 3 3)	0.0143	78.9431	46.0119

Table C.1 Bragg angle data of Au obtained from X-RAY SERVER.

C. 4. Bi

Name: bismuth
Symbol: Bi
Number: 83
Standard atomic weight: 208.98040
Electron configuration: [Xe] $4f^{14}$ $5d^{10}$ $6s^2$ $6p^3$
Electrons per shell: 2, 8, 18, 32, 18, 5
Electrical Conductivity: 8.67×10^5 Ωm^{-1}
Density : 9.78 g cm^{-3}
Melting point: 544.7 K
Specific heat capacity (25 ℃): 25.52 J mol^{-1} K^{-1}
Linear thermal expansion (25 ℃) 13.4 µm m^{-1} K^{-1}
Thermal conductivity (300 K) 7.97 W m^{-1} K^{-1}
Optical constants: n= 2.8324, k= 4.5191 @ 800 nm

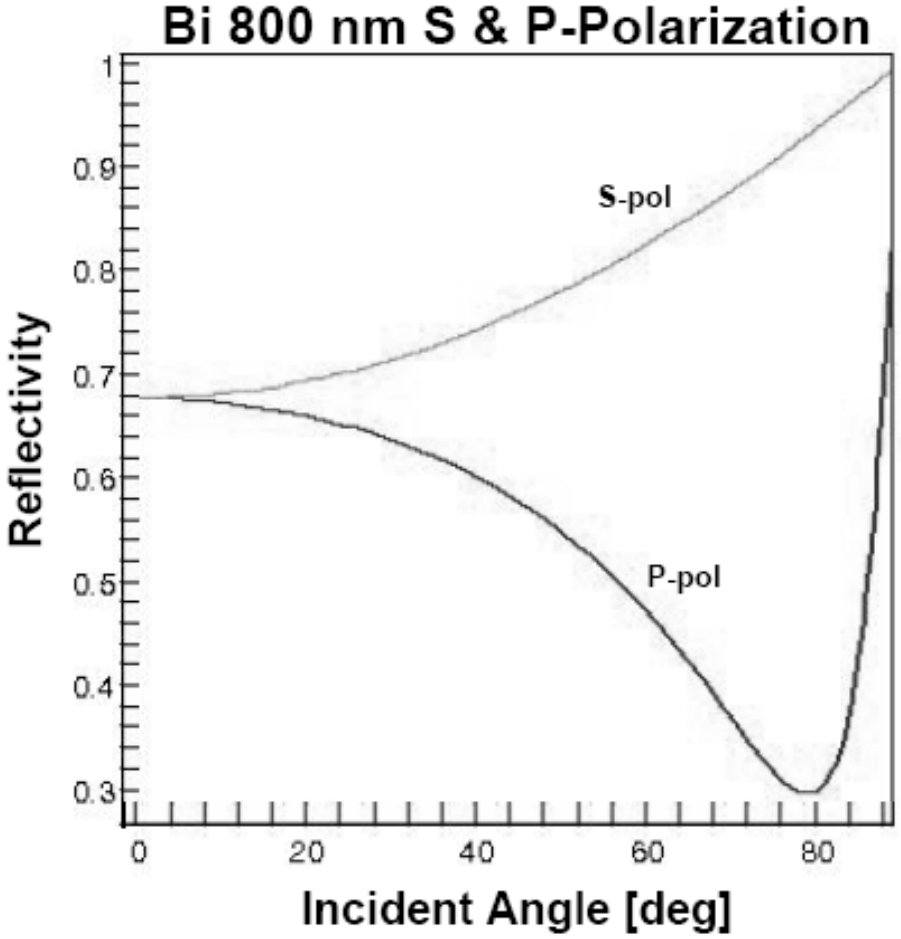

Fig. C.3 Reflectivity of Bismuth at 800nm, calculated from Fresnel equations.

Sample thickness: 50nm on Si wafer
Crystal structure: Bismuth-fcc
Symmetry group: Trigonal (Rhombohedral distortion)
Unit cell constant: a = b = c = 6.5720 Å.
Unit cell angles: $\alpha = \beta = \gamma = 87.570$ °
X-ray wavelength: 1.540562 Å
X-ray energy: 8.047984 keV
X-ray characteristic line: Cu-$K_{\alpha 1}$
Surface plane indices: (1 1 1)

Planes found: 9. Planes being displayed: 9

hkl	Angle to surface	Bragg angle	Relative Intensity xh/x0(%)
(1 1 1)	0.0035	11.2396	68.2238
(1 1 3)	31.0515	22.2835	57.5184
(1 3 1)	31.0515	22.2835	57.5184
(1 3 3)	23.2706	29.6742	51.1918

(2 2 2)	0.0035	22.9435	69.5383
(3 1 1)	31.0515	22.2835	57.5184
(3 1 3)	23.2706	29.6742	51.1918
(3 3 1)	23.2706	29.6742	51.1918
(3 3 3)	0.0163	35.7843	46.2169

Table C.2 Bragg angle data of Bi obtained from X-RAY SERVER.

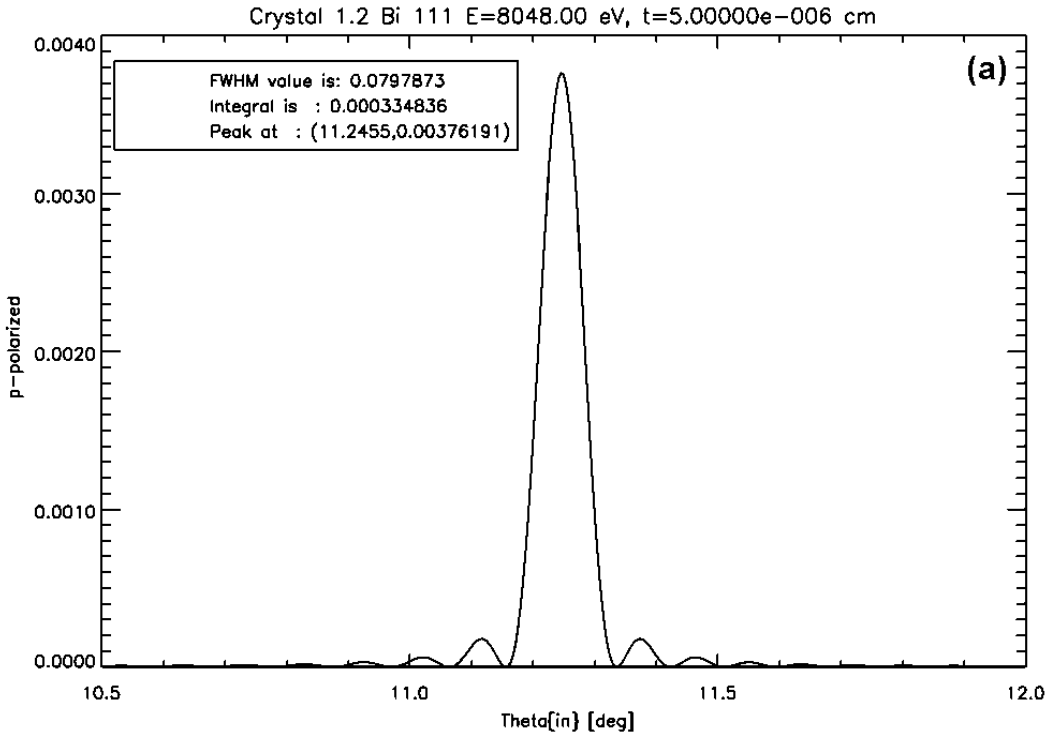

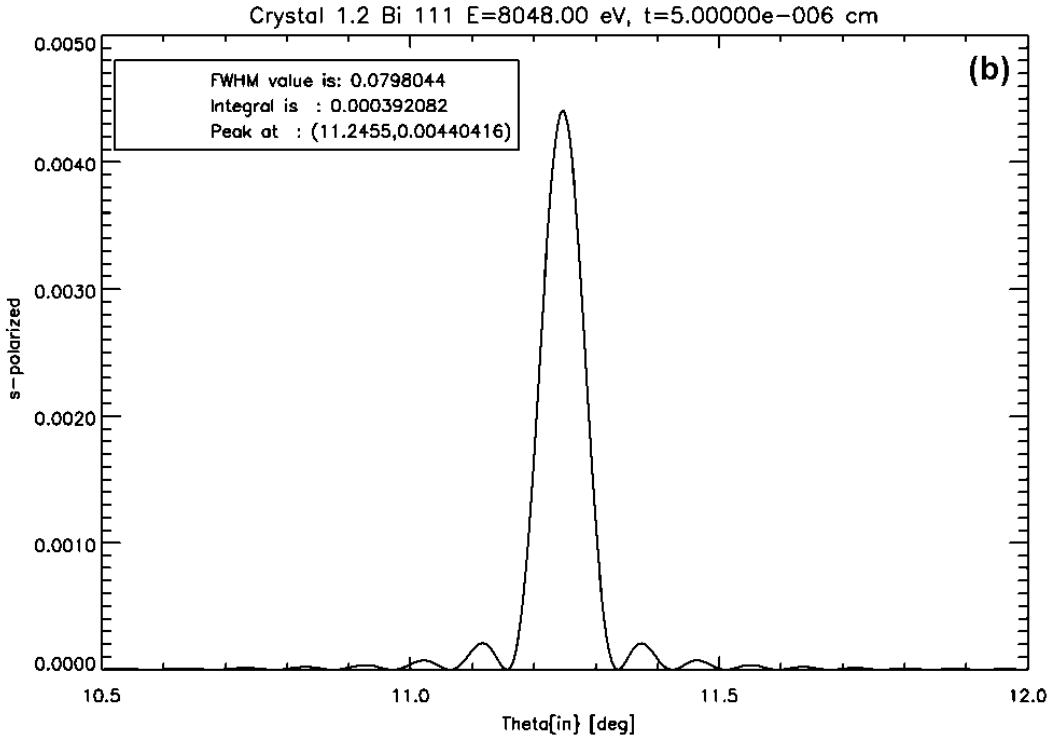

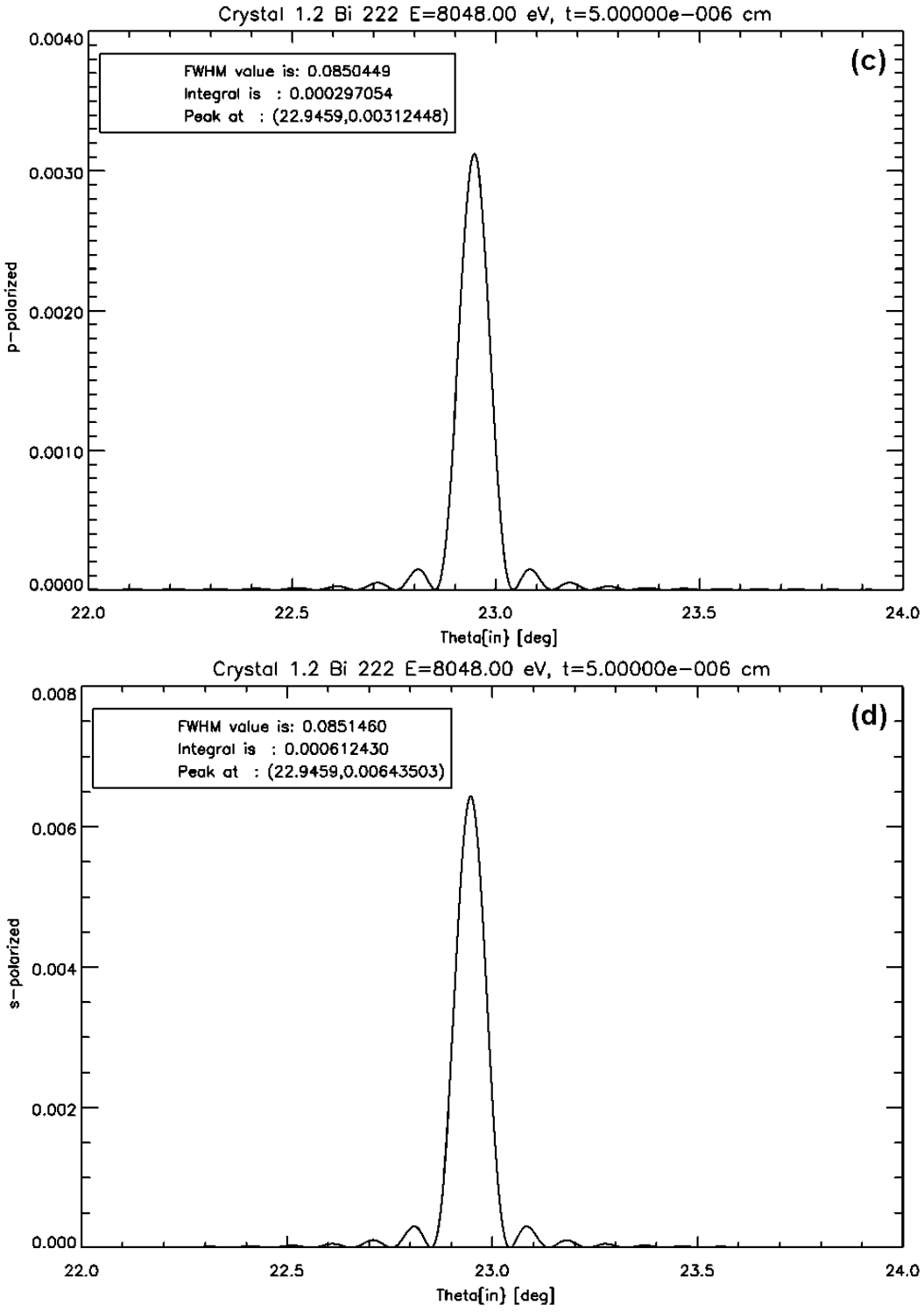

Fig. C.4 Bragg reflection of Bi (111) and (222) calculated from XOP. (a) and (c) P-polarized beam. (b) and (d) S-polarized beam.

Bibliography

[1] W. C. Röntgen, "On a new kind of Ray", *Nature* **53**, 274-277 (1896), translated by A. Stanton from, W. C. Röntgen, "Über eine neue Art von Strahlen", *Sitz. ber. an die med.-phys. Gesellschaft Würzburg*, (1895).

[2] C. Davisson and L. H. Germer, "The Scattering of Electrons by a Single Crystal of Nickel", *Nature* **119**, 558 (1927).

[3] G. P. Thomson and A. Reid, "Diffraction of Cathode Rays by a Thin Film", *Nature* **119**, 890 (1927).

[4] C. G. Shull, "Early development of neutron scattering", *Rev. Mod. Phys.* **67**, 753 (1995).

[5] D. Strickland and G. Mourou, "Compression of Amplified Chirped Optical Pulses", *Optics Communications* **55**, 447 (1985).

[6] D. Strickland and G. Mourou, "Compression of Amplified Chirped Optical Pulses *", *Optics Communications* **56**, 219 (1985).

[7] D. Kühlke, U. Herpes, D. von der Linde, "Soft x-ray emission from subpicosend laser-produced plasma", *Appl. Phys. Lett.* **50**, 1785 (1987).

[8] M. M. Murnane, H. C. Kapteyn, M. D. Rosen, R. W. Falcone, "Ultrafast X-ray Pulses from Laser-Produced Plasmas", *Science* **251**, 531 (1991).

[9] A. Rousse, P. Audebert, J. P. Geindre, F. Fall, and J. C. Gauthier, "Efficient *Kα* X-ray source from femtosecond laser-produced plasmas", *Phys. Rev. E* **50**, 2200 (1994).

[10] J. C. Williamson, J. Cao, H. Ihee, H. Frey and A. H. Zewail, "Clocking transient chemical changes by ultrafast electron diffraction", *Nature* **386**, 159 (1997).

[11] C.Y. Ruan, V. A. Lobastov, R. Srinivasan, B. M. Goodson, H. Ihee, and A. H. Zewail, "Ultrafast diffraction and structural dynamics: The nature of complex molecules far from equilibrium", *Proc. National Acad. Sci. USA* **98**, 7117 (2001).

[12] B. J. Siwick, J. R. Dwyer, R. E. Jordan and R. J. D. Miller, "Ultrafast electron optics: Propagation dynamics of femtosecond electron packets", *J. Appl. Phys.* **92**, 1643 (2002).

[13] B. J. Siwick, J. R. Dwyer, R. E. Jordan, and R. J. Dwayne Miller, "An Atomic-Level View of Melting Using Femtosecond Electron Diffraction", *Science* **302**, 1382 (2003).

[14] R. W. Schoenlein, S. Chattopadhyay, H. H. W. Chong, T. E. Glover, P. A. Heimann, C. V. Shank, A. A. Zholents, and M. S. Zolotorev, "Generation of Femtosecond Pulses of Synchrotron Radiation", *Science* **287**, 2237 (2000).

[15] S. Khan, K. Holldack, T. Kachel, R. Mitzner, and T. Quast, "Femtosecond Undulator Radiation from Sliced Electron Bunches", *Phys. Rev. Lett.* **97**, 074801 (2006).

[16] G. Ingold, P. Beaud, S. L. Johnson, D. Grolimund, V. Schlott, T. Schmidt and A. Streun, "Technical Report: FEMTO: A Sub-ps Tunable Hard X-ray Undulator Source for Laser/X-ray Pump-Probe Experiments at the SLS", *Sync. Rad. News* **20**, Issue **5**, 35 (2007).

[17] A. L. Cavalieri *et al.*, "Clocking Femtosecond X Rays", *Phys. Rev. Lett.* **94**, 114801 (2005).

[18] A. M. Lindenberg, *et al.*, "Atomic scale visualization of inertial dynamics", *Science* **308**, 392 (2005).

[19] A. Egbert, B. N. Chichkov and A. Ostendorf, "Ultrashort X-ray source driven by femtosecond laser pulses", *Europhys. Lett.* **56**, 228 (2001).

[20] A. Egbert, B. Mader, B. Tkachenko, C. Fallnich, B. N. Chichkov, H. Stiel and P. V. Nickles, "High-repetition rate femtosecond laser-driven hard-x-ray source", *Appl. Phys. Lett.* **81**, 2328 (2002).

[21] U. Hinze, A. Egbert, B. Chichkov, and K. Eidmann, "Generation of picosecond hard-x-ray pulses in a femtosecond-laser-driven x-ray diode", *Optics Letters* **29**, 2079 (2004).

[22] E. Seres, J. Seres F. Krausz, C. Spielmann, "Generation of Coherent Soft-X-Ray Radiation Extending Far Beyond the Titanium L Edge", *Phys. Rev. Lett.* **92**, 163002 (2004).

[23] J. Seres, E. Seres, A. J. Verhoef, G. Tempea, C. Streli, P. Wobrauschek, V. Yakovlev, A. Scrinzi, C. Spielmann and F. Krausz, "Laser technology: Source of coherent kiloelectronvolt X-rays", *Nature* **433**, 596 (2005).

[24] Ch. Spielmann, N. H. Burnett, S. Sartania, R. Koppitsch, M. Schnürer, C. Kan, M. Lenzner, P. Wobrauschek, F. Krausz, "Generation of Coherent X-rays in the Water Window Using 5-Femtosecond Laser Pulses", *Science* **278**, 661 (1997).

[25] J. Zhou, J. Peatross, M. M. Murnane, and H. C. Kapteyn, "Enhanced High-Harmonic Generation Using 25 fs Laser Pulses", *Phys. Rev. Lett.* **76**, 752 (1996).

[26] A. Rousse, K. Ta Phuoc, R. Shah, A. Pukhov, E. Lefebvre, V. Malka, S. Kiselev, F. Burgy, J. P. Rousseau, D. Umstadter, and D. Hulin, "Production of a keV X-Ray Beam from Synchrotron Radiation in Relativistic Laser-Plasma Interaction", *Phys. Rev. Lett.* **93**, 135005 (2004).

[27] V. Malka, J. Faure, Y. A. Gauduel, E. Lefebvre, A. Rousse and K. Ta Phuoc, "Principles and applications of compact laser–plasma accelerators", *Nature Physics* **4**, 447 (2008).

[28] H.-P. Schlenvoigt, K. Haupt, A. Debus, F. Budde, O. Jäckel, S. Pfotenhauer, H. Schwoerer, E. Rohwer, J. G. Gallacher, E. Brunetti, R. P. Shanks, S. M. Wiggins and D. A. Jaroszynski, "A compact synchrotron radiation source driven by a laser-plasma wakefield accelerator", *Nature Physics* **4**, 130 (2008).

[29] K. Nakajima, "Compact X-ray sources: Towards a table-top free-electron laser", *Nature Physics* **4**, 92 (2008).

[30] http://www-ssrl.slac.stanford.edu/lcls/index.html

[31] T. Ishikawa *et al.*, "A compact X-ray free-electron laser emitting in the sub-ångström region", *Nature Photon.* **6**, 540 (2012).

[32] http://www.xfel.eu/XFELpresse/en/hintergrund/was/index.html

[33] M. Altarelli, *et al. The European X-ray Free-electron Laser* (DESY Technical Report, Hamburg, Germany)

[34] S. Kneip, C. McGuffey, F. Dollar, M. S. Bloom, V. Chvykov, G. Kalintchenko, K. Krushelnick, A. Maksimchuk, S. P. D. Mangles, T. Matsuoka, Z. Najmudin, C. A. J. Palmer, J. Schreiber, W. Schumaker, A. G. R. Thomas, and V. Yanovsky, "X-ray phase contrast imaging of biological specimens with femtosecond pulses of betatron radiation from a compact laser plasma wakefield accelerator", *Appl. Phys. Lett.* **99**, 093701 (2011).

[35] K. Ta Phuoc, S. Corde,C. Thaury, V. Malka, A. Tafzi, J. P. Goddet,R. C. Shah, S. Sebban, A. Rousse, "All-optical Compton gamma-ray source", *Nature Photonics* **6**, 308 (2012).

[36] J. Ju, K. Svensson, A. Döpp, H. E. Ferrari, K. Cassou, O. Neveu, G. Genoud, F. Wojda, M. Burza, A. Persson, O. Lundh, C.-G. Wahlström, and B. Cros, "Enhancement of x-rays generated by a guided laser wakefield accelerator inside capillary tubes", *Appl. Phys. Lett.* **100**, 191106 (2012).

[37] M. Schnell, A. Sävert, B. Landgraf, M. Reuter, M. Nicolai, O. Jäckel, C. Peth, T. Thiele, O. Jansen, A. Pukhov, O. Willi, M. C. Kaluza, and C. Spielmann, "Betatron radiation based measurement of the electron-beam size in a wakefield accelerator", *AIP Conf. Proc.* **1462**, 231 (2011).

[38] S. Corde, C. Thaury, K. Ta Phuoc, A. Lifschitz, G. Lambert, J. Faure, O. Lundh, E. Benveniste, A. Ben-Ismail, L. Arantchuk, A. Marciniak, A. Stordeur, P. Brijesh, A. Rousse, A. Specka, and V. Malka, "Mapping the X-Ray Emission Region in a Laser-Plasma Accelerator," *Phys. Rev. Lett.* **107**, 215004 (2011).

[39] C. Rischel, A. Rousse, I. Uschmann, P. A. Albouy, J. P. Geindre, P. Audebert, J. C. Gauthier, E. Förster, J. L. Martin, and A. Antonetti, "Femtosecond time-resolved X-ray diffraction from laser heated organic films", *Nature* **390**, 490 (1997).

[40] T. Pfeifer, C. Spielmann and G. Gerber, "Femtosecond X-ray science", *Rep. Prog. Phys.* **96**, 443 (2006).

[41] M. Bargheer, N. Zhavoronkon, M. Woerner, and T. Elsaesser, "Recent progress in ultrafast X-ray diffraction", *Chem. Phys. Chem.* **7**, 783 (2006).

[42] C. Rose-Petruck, R. Jimenez, T. Guo, A. Cavalleri, C. W. Siders, F. Rksi, J. A. Squier, B. C. Walker, K. R. Wilson and C. P. J. Barty, "Picosecond–milliångström lattice dynamics measured by ultrafast X-ray diffraction", *Nature* **398**, 310 (1999).

[43] A. H. Chin, R. W. Schoenlein, T. E. Glover, P. Balling, W. P. Leemans, and C. V. Shank, "Ultrafast Structural Dynamics in InSb Probed by Time-Resolved X-Ray Diffraction", *Phys. Rev. Lett.* **83**, 336 (1999).

[44] A.M. Lindenberg, I. Kang, S. L. Johnson, T. Missalla, P. A. Heimann, Z. Chang, J.Larsson, P. H. Bucksbaum, H. C. Kapteyn, H. A. Padmore, R. W. Lee, J. S. Wark and R. W. Falcone, "Time-resolved X-ray diffraction from coherent phonons during a laser-induced phase transition", *Phys. Rev. Lett.* **84**, 111 (2000).

[45] A. Cavalleri, C. W. Siders, F. L. H. Brown, D. M. Leitner, C. Tóth, J. A. Squier, C. P. J. Barty, K. R. Wilson, K. Sokolowski-Tinten, M. Horn von Hoegen, and D. von der Linde, M. Kammler, "Anharmonic Lattice Dynamics in Germanium Measured with Ultrafast X-Ray Diffraction", *Phys. Rev. Lett.* **85**, 586 (2000).

[46] A. Cavalleri, C. W. Siders, C. Rose-Petruck, R. Jimenez, C. Tóth, J. A. Squier, C. P.J. Barty, K. R. Wilson, K. Sokolowski-Tinten, M. Horn-von Hoegen and D. von der Linde, "Ultrafast x-ray measurement of laser heating in semiconductors: Parameters determining the melting threshold", *Phys. Rev. B* **63**, 193306 (2001).

[47] D. A. Reis, M. F. DeCamp, P. H. Bucksbaum, R. Clarke, E. Dufresne, M. Hertlein, R. Merlin, R. Falcone, H. Kapteyn, M. M. Murnane, J. Larsson, Th. Missalla and J. S. Wark, "Probing impulsive strain propagation with X-Ray pulses", *Phys. Rev. Lett.* **86**, 3072 (2001).

[48] M. F. DeCamp, D. A. Reis, P. H. Bucksbaum, B. Adams, J. M. Caraher, R. Clarke, C. W. S. Conover, E. M. Dufresne, R. Merlin, V. Stoica and J. K. Wahlstrand, "Coherent control of pulsed X-ray beams", *Nature* **413**, 825 (2001).

[49] D. von der Linde, K. Sokolowski-Tinten, Ch. Blome, C. Dietrich, A. Tarasevitch, A. Cavalleri, and J. A. Squier, "'Ultrafast' extended to X-rays: Femtosecond time-resolved X-ray diffraction", *Z. f. Phys. Chemie* **215**, 1527 (2001).

[50] J. Larsson, A. Allen, P. H. Bucksbaum, R. W. Falcone, A. Lindenberg, G. Naylor, T. Missalla, D. A. Reis, K. Scheidt, A. Sjögren, P. Sondhauss, M. Wulff and J. S.Wark, "Picosecond X-ray diffraction studies of laser-excited acoustic phonons in InSb", *Appl. Phys. A* **75**, 467 (2002).

[51] O. Synnergren, M. Harbst, T. Missalla, J. Larssona, G. Katona, R. Neutze, and R. Wouts, "Projecting picosecond lattice dynamics through x-ray topography", *Appl. Phys. Lett.* **80**, 3727 (2002).

[52] A. M. Lindenberg, I. Kang, S. L. Johnson, R. W. Falcone, P. A. Heimann, Z. Chang, R. W. Lee, and J. S. Wark, "Coherent control of phonons probed by time-resolved x-ray diffraction", *Opt. Lett.* **27**, 869 (2002).

[53] M. F. DeCamp, D. A. Reis, A. Cavalieri, P. H. Bucksbaum, R. Clarke, R. Merlin, E.M. Dufresne, D. A. Arms, A. M. Lindenberg, A.G. MacPhee, Z. Chang, B.

Lings, J. S.Wark and S. Fahy, "Transient strain driven by a dense electron-hole plasma", *Phys. Rev. Lett.* **91**, 165502 (2003).

[54] M. Bargheer, N. Zhavoronkov, Y. Gritsai, J. C. Woo, D. S. Kim, M. Woerner and T. Elsaesser, "Coherent atomic motions in a nanostructure studied by femtosecond X-ray diffraction", *Science* **306**, 1771 (2004).

[55] M. F. DeCamp, D. A. Reis, D. M. Fritz, P. H. Bucksbaum, E. M. Dufresneb, and Roy Clarke, "X-ray synchrotron studies of ultrafast crystalline dynamics", *J. Synchrotron Rad.* **12**, 177 (2005).

[56] S. H. Lee, A. L. Cavalieri, D. M. Fritz, M. C. Swan, R. S. Hegde, M. Reason, R. S. Goldman and D. A. Reis, "Generation and propagation of a picosecond acoustic pulse at a buried interface: Time-resolved X-ray diffraction measurements", *Phys. Rev. Lett.* **95**, 246104 (2005).

[57] Y. Hayashi, Y. Tanaka, T. Kirimura, N. Tsukuda, E. Kuramoto, and T. Ishikawa, "Acoustic pulse echoes probed with time-resolved X-ray triple-crystal diffractometry", *Phys. Rev. Lett.*, **96**, 115505 (2006).

[58] C. V. Korff Schmising, M. Bargheer, M. Kiel, N. Zhavoronkov, M.Woerner, T. Elsaesser, I. Vrejoiu, D. Hesse, and M. Alexe, "Strain propagation in nanolayered perovskites probed by ultrafast x-ray diffraction", *Phys. Rev. B*, **73**, 212202 (2006).

[59] A. Morak, T. Kämpfer, I. Uschmann, A. Lübcke, E. Förster, and R. Sauerbrey, "Acoustic phonons in InSb probed by time-resolved x-ray diffraction", *Phys. Stat. Sol. b* **243**, 2728 (2006).

[60] H. Enquist, H. Navirian, T. N. Hansen, A. M. Lindenberg, P. Sondhauss, O.Synnergren, J. S.Wark, and J. Larsson, "Large Acoustic Transients Induced by Nonthermal Melting of InSb", *Phys. Rev. Lett.* **98**, 225502 (2007).

[61] M. Nicoul, U. Shymanovich, A. Tarasevitch, D. von der Linde, and K. Sokolowski-Tinten, "Picosecond acoustic response of a laser-heated Gold-film studied with time-resolved X-ray diffraction"**,** *Appl. Phys. Lett.* **98**, 191902 (2011).

[62] R. Shayduk, H. Navirian, W. Leitenberger, J. Goldshteyn, I. Vrejoiu, M. Weinelt, P. Gaal, M. Herzog, C. v Korff Schmising and M. Bargheer, "Nanoscale heat transport studied by high-resolution time-resolved x-ray diffraction", *New Journal of Physics* **13**, 093032 (2011).

[63] M. Herzog, D. Schick, W. Leitenberger, R. Shayduk, R. M van der Veen, C. J. Milne, S. L. Johnson, I. Vrejoiu and M. Bargheer, "Tailoring interference and nonlinear manipulation of femtosecond x-rays", *New Journal of Physics* **14**, 013004 (2012).

[64] M. Herzog, D. Schick, P. Gaal, R. Shayduk, C. v. Korff Schmising, M. Bargheer, "Analysis of ultrafast X-ray diffraction data in a linear-chain model of the lattice dynamics", *Appl Phys A* **106**, 489 (2012).

[65] M. Herzog, A. Bojahr, J. Goldshteyn, W. Leitenberger, I. Vrejoiu, D. Khakhulin, M. Wulff, R. Shayduk, P. Gaal, and M. Bargheer, "Detecting optically synthesized quasi-monochromatic sub-terahertz phonon wavepackets by ultrafast x-ray diffraction", *Appl. Phys. Lett.* **100**, 094101 (2012).

[66] C. V. Korff Schmising, A. Harpoeth, N. Zhavoronkov, M. Woerner, T. Elsaesser, M. Bargheer, M. Schmidbauer, I. Vrejoiu, D. Hesse and M. Alexe, "Femtosecond X-ray diffraction from nanolayered oxides", *Physics Procedia* **3**,333 (2010).

[67] S. L. Johnson, P. Beaud, E. Vorobeva, C. J. Milne, É.D. Murray, S. Fahy and G. Ingold, "Non-equilibrium phonon dynamics studied by grazing-incidence femtosecond X-ray crystallography", *Acta Cryst. A* **66**, 157 (2010).

[68] K. Sokolowski-Tinten, C. Blome, J. Blums, A. Cavalleri, C. Dietrich, A. Tarasevitch, I. Uschmann, E. Förster, M. Kammler, M. Horn-von Hoegen and D. von der Linde, "Femtosecond X-ray measurement of coherent lattice vibrations near the Lindemann stability limit", *Nature* **422**, 287 (2003).

[69] D. M. Fritz, *et al.*, "Ultrafast bond softening in Bismuth: Mapping a solid's interatomic potential with X-rays", *Science* **315**, 633 (2007).

[70] M. Bargheer, N. Zhavoronkov, J. C. Woo, D. S. Kim, M. Woerner, and T. Elsaesser,"Excitation mechanisms of coherent phonons unravelled by femtosecond X-ray diffraction", *Phys. Stat. Sol. (b)* **243**, 2389 (2006).

[71] C. von Korff Schmising, M. Bargheer, M. Kiel, N. Zhavoronkov, M. Woerner, T.Elsaesser, I. Vrejoiu, D. Hesse, and M. Alexe, "Accurate time delay determination for femtosecond X-ray diffraction experiments" *Appl. Phys. B* **88**, 1 (2007).

[72] B. Freyer, J. Stingl, F. Zamponi, M. Woerner, and T. Elsaesser, "The rotating-crystal method in femtosecond X-ray diffraction", *Optics Express* **19**, 15506 (2011).

[73] S. L. Johnson, P. Beaud, C. J. Milne, F. S. Krasniqi, E. S. Zijlstra, M. E. Garcia, M. Kaiser, D. Grolimund, R. Abela, and G. Ingold, "Nanoscale Depth-Resolved Coherent Femtosecond Motion in Laser-Excited Bismuth", *Phys. Rev. Lett.* **100**, 155501 (2008).

[74] K. H. Bennemann, "Ultrafast dynamics in solids", *J. Phys.: Condens. Matter* **16**, R995 (2004).

[75] C. W. Siders, A. Cavalleri, K. Sokolowski-Tinten, Cs. Tóth, T. Guo, M. Kammler, M. Horn von Hoegen, K. R. Wilson, D. von der Linde, and C. P. J. Barty, "Detection of Nonthermal Melting by Ultrafast X-ray Diffraction", *Science* **286**, 1340 (1999).

[76] K. Sokolowski-Tinten, C. Blome, C. Dietrich, A. Tarasevitch,M. Horn-von Hoegen, D. von der Linde, A. Cavalleri, J. Squier, and M. Kammler,

"Femtosecond X-ray measurement of ultrafast melting and large acoustic transients", *Phys. Rev. Lett.* **87**, 225701 (2001).

[77] T. Feurer, A. Morak, I. Uschmann, Ch. Ziener, H. Schwoerer, Ch. Reich, P. Gibbon, E. Förster, R. Sauerbrey, K. Ortner and C. R. Becker, "Femtosecond silicon K_α pulses from laser-produced plasmas", *Phys. Rev. E* **65**, 016412 (2001).

[78] A. Rousse, C. Rischel, S. Fourmaux, I. Uschmann, S. Sebban, G. Grillon, P. Balcou, E. Förster, J. P. Geindre, P. Audebert, J. C. Gauthier, and D. Hulin, "Non-thermal melting in semiconductors measured at femtosecond resolution", *Nature* **410**, 65 (2001).

[79] K. J. Gaffney ***et al.*** "Observation of Structural Anisotropy and the Onset of Liquidlike Motion During the Nonthermal Melting of InSb", *Phys. Rev. Lett.* **95**, 125701 (2005).

[80] P. B. Hillyard *et al.*, "Carrier-density-dependent lattice stability in InSb", *Phys. Rev.Lett.* **98**, 125501 (2007).

[81] G. Sciaini, M. Harb, S. G. Kruglik, T. Payer, C. T. Hebeisen, F. -J. Meyer zu Heringdorf, M. Yamaguchi, M. Horn von Hoegen, R. Ernstorfer and R. J. D. Miller, "Electronic acceleration of atomic motions and disordering in bismuth", *Nature* **458**, 56 (2009).

[82] E. Collet *et al.*, "Laser-Induced Ferroelectric Structural Order in an Organic Charge-Transfer Crystal", *Science* **300**, 612 (2003).

[83] A. Cavalleri, S. Wall, C. Simpson, E. Statz, D. W. Ward, K. A. Nelson, M. Rini, R. W. Schoenlein "Tracking the motion of charges in a terahertz light field by femtosecond X-ray diffraction,", *Nature* **442** , 664 (2006).

[84] S.K. Streiffer, J.A. Eastman, D.D. Fong, C. Thompson, A. Munkholm, M.V. Ramana Murty, O. Auciello, G.R. Bai, G.B. Stephenson, "Observation of nanoscale 180 deg stripe domains in ferroelectric PbTiO3 thin films", *Phys. Rev. Lett.* **89**, 067601 (2002).

[85] R.V. Wang, D.D. Fong, F. Jiang, M.J. Highland, P.H. Fuoss, C. Thompson, A. M. Kolpak, J. A. Eastman, S. K. Streiffer, A. M. Rappe, and G. B. Stephenson, "Reversible chemical switching of a ferroelectric film", *Phys. Rev. Lett.* **102**, 047601 (2009).

[86] M. Woerner, C. v. Korff Schmising, M. Bargheer, N. Zhavoronkov, I. Vrejoiu, D. Hesse, M. Alexe and T. Elsaesser, "Ultrafast structural dynamics of perovskite superlattices", *Applied Physics A* **96**, 83 (2009).

[87] D. Daranciang, M. J. Highland, H. Wen, *et al*. "Ultrafast photovoltaic response in ferroelectric nanolayers", *Phys Rev. Lett.* **108**, 087601 (2012).

[88] I. Radu, C. Stamm, N. Pontius, T. Kachel, P. Ramm, J.-U. Thiele, H. A. Dürr, and C. H. Back, "Laser-induced generation and quenching of magnetization on FeRh studied with time-resolved x-ray magnetic circular dichroism", *Phys. Rev. B* **81**, 104415 (2010).

[89] U. Shymanovich, F. Quirin, M. Vattilana, W. Lu, M. Nicoul, A.-E. El-Kamhawy, A. Tarasevitch, D. von der Linde, K. Sokolowski-Tinten, **"**Ultrafast lattice dynamics in FeRh during a laser-induced magnetic phase transition", *Ultrafast Phenomena XVII*, Oxford University Press (2011).

[90] C. Stamm, T. Kachel, N. Pontius, R. Mitzner, T. Quast, K. Holldack, S. Khan, C. Lupulescu, E. F. Aziz, M. Wietstruk, H. A. Dürr and W. Eberhardt, "Femtosecond modification of electron localization and transfer of angular momentum in nickel", *Nature Materials* **6**, 740 (2007).

[91] C. Stamm, J.-U. Thiele, T. Kachel, I. Radu, P. Ramm, M. Kosuth, J. Minár, H. Ebert, H. A. Dürr, W. Eberhardt, and C. H. Back, "Antiferromagnetic-ferromagnetic phase transition in FeRh probed by x-ray magnetic circular dichroism", *Phys. Rev. B* **77**, 184401 (2008).

[92] M. Wietstruk, A. Melnikov, Ch. Stamm, T. Kachel, N. Pontius, M. Sultan, C. Gahl, M.Weinelt, H. A. Dürr, U. Bovensiepen, "Hot electron driven enhancement of spin-lattice coupling in 4f ferromagnets observed by femtosecond x-ray magnetic circular dichroism**",** *Phys. Rev. Lett.* **106**, 127401 (2011).

[93] C. Boeglin, E. Beaurepaire, V. Halté, V. López-Flores, C. Stamm, N. Pontius, H. A. Dürr and J.-Y. Bigo, "Distinguishing the ultrafast dynamics of spin and orbital moments in solids", *Nature* **465**, 458 (2010).

[94] C. Stamm, N. Pontius, T. Kachel, M. Wietstruk, and H. A. Dürr, "Femtosecond x-ray absorption spectroscopy of spin and orbital angular momentum in photoexcited Ni films during ultrafast demagnetization", *Phys. Rev. B* **81**, 104425 (2010).

[95] H. A. Dürr, "Femtosecond electron and spin dynamics in ferromagnetic Ni probed by UV and soft X-ray pulses", *Nucl. Instr. and Meth. A* **601**, 132 (2009).

[96] J. Miguel, J. Sánchez-Barriga, D. Bayer, J. Kurde, B. Heitkamp, M. Piantek, F. Kronast, M. Aeschlimann, H. A. Dürr and W. Kuch, "Time-resolved magnetization dynamics of cross-tie domain walls in permalloy microstructures", *J. Phys.: Condens. Matter* **21**, 496001 (2009).

[97] T. Kachel, N. Pontius, C. Stamm, M. Wietstruk, E. F. Aziz, H. A. Dürr, W. Eberhardt, and F. M. F. de Groot, "Transient electronic and magnetic structures of nickel heated by ultrafast laser pulses", *Phys. Rev. B* **80**, 092404 (2009).

[98] H. A. Dürr, C. Stamm, T. Kachel, N. Pontius, R. Mitzner, T. Quast, K. Holldack, S. Khan, C. Lupulescu, E.F. Aziz, M. Wietstruk, W. Eberhardt, "Ultrafast Electron and Spin Dynamics in Nickel Probed With Femtosecond X-Ray Pulses", *IEEE Trans. Magn.* **44**, 1957 (2008).

[99] S. L. Johnson, *et al*. "Femtosecond Dynamics of the Collinear-to-Spiral Antiferromagnetic Phase Transition in CuO", *Phys. Rev. Lett.* **108**, 037203 (2012).

[100] K. A. Seu, S. Roy, J. J. Turner, S. Park, C. M. Falco, and S. D. Kevan, "Cone phase and magnetization fluctuations in Au/Co/Au thin films near the spin-reorientation transition", *Phys. Rev. B* **82**, 012404 (2010).

[101] I. Radu, K. Vahaplar, C. Stamm, T. Kachel, N. Pontius, H. A. Dürr, T. A. Ostler, J. Barker, R. F. L. Evans, R. W. Chantrell, A. Tsukamoto, A. Itoh, A. Kirilyuk, Th. Rasing and A. V. Kimel, "Transient ferromagnetic-like state mediating ultrafast reversal of antiferromagnetically coupled spins", *Nature* **472**, 205 (2011).

[102] K. Holldack, N. Pontius, E. Schierle, T. Kachel, V. Soltwisch, R. Mitzner, T. Quast, G. Springholz, and E. Weschke, "Ultrafast dynamics of antiferromagnetic order studied by femtosecond resonant soft x-ray diffraction", *Appl. Phys. Lett.* **97**, 062502 (2010).

[103] A. Kirilyuk, A. Kimel, and T. Rasing, "Ultrafast optical manipulation of magnetic order", *Rev. Mod. Phys.* **82**, 2731 (2010).

[104] F. Quirin, M. Vattilana, U. Shymanovich, A.-E. El-Kamhawy, A. Tarasevitch, J. Hohlfeld, D. von der Linde, and K. Sokolowski-Tinten, "Structural dynamics in FeRh during a laser-induced metamagnetic phase transition", *Phys. Rev. B* **85**, 020103(R) (2012).

[105] U. Shymanovich, M. Nicoul, W. Lu, S. Kähle, A. Tarasevitch, K. Sokolowski-Tinten, and D. von der Linde, "Towards ultrafast time-resolved Debye-Scherrer Xray diffraction using a laser-plasma source", *Rev. Sci. Instrum.* **80**, 083102 (2009).

[106] F. Zamponi, Z. Ansari, M. Woerner, and T. Elsaesser, "Femtosecond powder diffraction with a laser-driven hard X-ray source", *Optics Express* **18**, 947 (2010).

[107] F. Zamponi, Z. Ansari, C. v. Korff Schmising, P. Rothhardt, N. Zhavoronkov, M. Woerner, T. Elsaesser, M. Bargheer, T. Trobitzsch-Ryll and M. Haschke, "Femtosecond hard X-ray plasma sources with a kilohertz repetition rate", *Appl. Phys. A* **96**, 51 (2009).

[108] J. Stingl, F. Zamponi, B. Freyer, M. Woerner, T. Elsaesser, and A. Borgschulte, "Strong-field electron transfer in a virtual quantum state mapped by femtosecond x-ray diffraction", *Phys. Rev. Lett.* **109**, 147402 (2012).

[109] M. J. J. Vrakking and T. Elsaesser, "X-rays inspire electron movies", *Nature Photon.* **6**, 645 (2012).

[110] F. Zamponi, J. Stingl, M. Woerner, and T. Elsaesser, "Ultrafast soft-mode driven charge relocation in an ionic crystal", *Physical Chemistry Chemical Physics (PCCP)* **14**, 6156 (2012).

[111] M. Trigo, J. Chen, V. H. Vishwanath, Y. M. Sheu, T. Graber, R. Henning, and D. A. Reis, "Imaging nonequilibrium atomic vibrations with x-ray diffuse scattering", *Physical Review B* **82**, 235205(2010).

[112] A. M. Lindenberg *et al*, "X-Ray Diffuse Scattering Measurements of Nucleation Dynamics at Femtosecond Resolution", *Phys. Rev. Lett.* **100**, 135502 (2008).

[113] M. Born and E. Wolf, *Principles of optics*, Cambridge University Press (1988).

[114] G. Jenke, "Erzeugung von XUV- und Röntgenstralung mit Femtosecunden-Laserimpulsen", Dissertation (1999).

[115] Z. Jiang, J. C. Kieffer, J. P. Matte, M. Chaker, O. Peyrusse, D. Gilles, G.Korn, A. Maksimchuk, S. Coe, and G. Mourou, "X-ray spectroscopy of hot solid density plasmas produced by subpicosecond high contrast laser pulses at 10^{18}–10^{19} W/cm^2",*Phys. Plasmas* **2**, 1702 (1995).

[116] F. Brunel, "Not-So Resonant, Resonant Absorption", *Phys. Rev. Lett.* **59**, 52 (1987).

[117] S. C. Wilks and W. L. Kruer, "Absorption of ultrashort, ultra-intense laser light by solids and overdense plasmas", *IEEE J. Quan. Electron.* **33**, 1954 (1997).

[118] S. Bastiani, A. Rousse, J. P. Geindre, P. Audebert, C. Quoix, G. Hamoniaux, A. Antonettia, and J. C. Gauthier, "Experimental study of the interaction of subpicosecond laser pulses with solid targets of varying initial scale lengths", *Phys. Rev. E* **56**, 7179 (1997).

[119] P. Gibbon, E. Förster, "Short-pulse laser-plasma interactions", *Plasma Phys. Control. Fusion* **38**, 769 (1996).

[120] T. Feurer, A. Morak, I. Uschmann, Ch. Ziener, H. Schwörer, E. Förster, and R. Sauerbrey, "An incoherent sub-picosecond X-ray source for time-resolved X-ray-diffraction experiments", *Appl. Phys. B: Lasers Opt.* **72**, 15 (2001).

[121] C. Reich, P. Gibbon, I. Uschmann and E. Förster, "Yield optimization and time structure of femtosecond laser plasma K_α sources", *Phys. Rev. Lett.* **84**, 4846 (2000).

[122] T. Guo, Ch. Spielmann, B. C. Walker, C. P. J. Barthy, "Generation of hard X-rays by ultrafast terawatt lasers", *Rev. Sci. Instr.* **72**, 41 (2001).

[123] R. Fedosejevs, R. Ottmann, R. Sigel, G. Kühnle, S. Szatmári, F. P. Schäfer, "Absorption of subpicosecond ultraviolet laser pulses in high-density plasma", *Appl.Phy.B* **50**, 79 (1990).

[124] C. A. Quarles, "Semiempirical analysis of electron-induced K-shell ionization", *Phys. Rev. A* **13**, 1278 (1976).

[125] W. E. Burcham, *Elements of Nuclear Physics*, Pearson (1979).

[126] E. Casnati, A. Tartari and C. Baraldi, "An empirical approach to K-shell ionisation cross section by electrons", *J. Phys. B* **15**, 155 (1982).

[127] P. Gibbon, A. Andreev, E. Lefebvre, G. Bonnaud, H. Ruhl, J. Delettrez, and A. R. Bell, "Calibration of one-dimensional boosted kinetic codes for modeling high-intensity laser–solid interactions", *Phys. Plasmas* **6**, 947 (1999).

[128] D.C. Joy, *Monte Carlo Modeling for Electron Microscopy and Microanalysis*, Oxford University Press, Oxford (1995).

[129] D. Salzmann, Ch. Reich, I. Uschmann, E. Förster, P.Gibbon, "Theory of K_α generation by femtosecond laser-produced hot electrons in thin foils", *Phys. Rev. E* **65**, 036402 (2002).

[130] F. Y. Khattak, O. A. M. B. Percie du Sert, D. Riley, P. S. Foster, E. J. Divall, C. J. Hooker, A. J. Langley, J. Smith, and P. Gibbon, "Comparison of experimental and simulated K_α yield for 400 nm ultrashort pulse laser irradiation", *Phys. Rev. E* **74**, 027401 (2006).

[131] P. Gibbon and A. R. Bell, "Collisionless Absorption in Sharp-Edged Plasmas", *Phys. Rev. Lett.* **68**, 1535 (1992).

[132] D. D. Meyerhofer, H. Chen, J. A. Delettrez, B. Soom, S. Uchida, and B. Yaakobi, "Resonance absorption in high-intensity contrast, picosecond laser-plasma interactions", *Phys. Fluids B* **5** , 2584 (1993).

[133] U. Teubner, W. Theobald, and C. Wülker, "Mechanisms and origin of continuum and line emission from carbon plasmas produced by ultrashort laser pulses**"**, *J. Phys. B* **29**, 4333 (1996).

[134] M. Schnürer, M. P. Kalashnikov, P. V. Nickles, Th. Schlegel, W. Sandner, N. Demchenko, R. Nolte, and P. Ambrosi, "Hard x-ray emission from intense short pulse laser plasmas", *Phys. Plasmas* **2**, 3106 (1995)

[135] J. D. Kmetec, C. L. Gordon, III, J. J. Macklin, B. E. Lemoff, G. S. Brown, and S. E. Harris, "MeV x-ray generation with a femtosecond laser", *Phys. Rev. Lett.* **68**, 1527 (1992).

[136] A. P. Fews, P. A. Norreys, F. N. Beg, A. R. Bell, A. E. Dangor, C. N. Danson, P. Lee, and S. J. Rose, "Plasma Ion Emission from High Intensity Picosecond Laser Pulse Interactions with Solid Targets", *Phys. Rev. Lett.* **73**, 1801 (1994).

[137] D. C. Eder, G. Pretzler, E. Fill, K. Eidmann, and A. Saemann, "Spatial characteristics of K_α radiation from weakly relativistic laser plasmas", *Appl. Phys. B: Lasers Opt.* **70**, 211 (2000).

[138] S. Backus, C. G. Durfee, M. M. Murnane, and H. C. Kapteyn, "High power ultrafast lasers", *Rev. Sci. Instrum.* 69, 1207 (1998).

[139] K. Lobov, "High order harmonic generation at relativistic laser intensities", Dissertation (2008).

[140] U. Shymanovich, "Direct observation of ultrafast atomic motion using time-resolved X-ray diffraction", Dissertation (2007).

[141] F. Scholze, H. Henneken, P. Kuschnerus, H. Rabus, M. Richter, G. Ulm, "Determination of the electron–hole pair creation energy for semiconductors from the spectral responsivity of photodiodes", *Nuclear Instruments and Methods in Physics Research A* **439**, 208 (2000).

[142] F. Zamponi, T. Kämpfer, A. Morak, I. Uschmann, and E. Förster, "Characterization of a deep depletion, back-illuminated charge-coupled device in the x-ray range", *Rev. Sci. Instrum.* **76**, 116101 (2005).

[143] The quantum efficiency of the CCD was calibrated with a Si reference detector.

[144] D. W. Forslund, J. M. Kindel, and K. Lee, "Theory of Hot-Electron Spectra at High Laser Intensity", *Phys. Rev. Lett.* **39**, 284 (1977).

[145] W. L. Kruer and K. Estabrook, "Laser light absorption due to self-generated magnetic fields", *Phys. Fluids* **20**, 1688 (1977).

[146] N. H. Burnett, G. D. Enright, A. Avery, A. Loen, and J. C. Kieffer, "Time-resolved K_α spectra in high-intensity laser-target interaction", *Phys. Rev. A* **29**, 2294 (1984).

[147] W. L. Kruer, *The Physics of Laser Plasma Interaction*, Addison-Wesley (1988).

[148] N. Zhavoronkov, Y. Gritsai, M. Bargheer, M. Woerner, and T. Elsaesser, "Generation of ultrashort $\boldsymbol{K_\alpha}$ radiation from quasipoint interaction area of femtosecond pulses with thin foils", *Appl. Phys. Lett.* **86**, 244107 (2005).

[149] F. Ewald, H. Schwoerer, and R. Sauerbrey, "K_α-radiation from relativistic laser-produced plasmas", *Europhys. Lett.* **60**, 710 (2002).

[150] A. Zhidkov, A. Sasaki, T. Utsumi, I. Fukumoto, T. Tajima, F. Saito, Y. Hironaka, K. G. Nakamura, K. I. Kondo, and M. Yoshida, "Prepulse effects on the interaction of intense femtosecond laser pulses with high-*Z* solids", *Phys. Rev. E* **62**, 7232 (2000).

[151] F. Y. Khattak, E. Garcia Saiz, T. Dzelzainis, D. Riley, and Z. Zhai, "Scale-length optimizing of short pulse Cu K_α laser-plasma sources", *Appl. Phys. Lett.* **90**, 081502 (2007).

[152] Ch. Reich, I. Uschmann, F. Ewald, S. Düsterer, A. Lübcke, H. Schwoerer, R. Sauerbrey, E. Förster, and P. Gibbon, "Spatial characteristics of Kα x-ray emission from relativistic femtosecond laser plasmas", *Phys. Rev. E* **68**, 056408 (2003).

[153] K. Sokolowski-Tinten, C. Blome, J. Blums, A. Cavalleri, C. Dietrich, A. Tarasevitch, and D. von der Linde, "Ultrafast Time-Resolved X-ray Diffraction", *AIP Conf. Proc.* **634**, 11 (2002).

[154] N. Zhavoronkov, Y. Gritsai, M. Bargheer, M. Woerner, T. Elsaesser, F. Zamponi, I. Uschmann and E. Forster, "Ultrafast Optics - Microfocus Cu Kα source for femtosecond x-ray science", *Optics Letters* **30**, 1737 (2005).

[155] Bixue Hou, James Easter, Karl Krushelnick, and John A. Nees, " Generation of hard x rays by femtosecond laser pulse interaction with Cu in laminar helium flow in ambient air", *Appl. Phys. Lett.* **92**, 161501 (2008).

[156] Ch. Ziener, I. Uschmann, G. Stobrawa, Ch. Reich, P. Gibbon, T. Feurer, A. Morak, S. Düsterer, H. Schwoerer, E. Förster, and R. Sauerbrey, "Optimization of K_α bursts for photon energies between 1.7 and 7 keV produced by

femtosecond-laser-produced plasmas of different scale length", *Phys. Rev. E* **65**, 066411 (2002).

[157] U. Teubner, J. Bergmann, B. van Wonterghem, F. P. Schäfer, and R. Sauerbrey, "Angle-dependent x-ray emission and resonance absorption in a laser-produced plasma generated by a high intensity ultrashort pulse", *Phys. Rev. Lett.* **70**, 794 (1993).

[158] U. Teubner, P. Gibbon, E. Förster, F. Falliès, P. Audebert, J. P. Geindre, and J. C. Gauthier, "Subpicosecond KrF*-laser plasma interaction at intensities between 10^{14} and 10^{17} W/cm^2", *Phys. Plasmas* **3**, 2679 (1996).

[159] J. F. Liu, W. Yu and L. J. Qian, "Charge Displacement in Ultraintense Laser-Plasma Interaction", *Physica Scripta* **72**, 243 (2005).

[160] T. P. Hughes, *Plasma and Laser Light*, Adam Hilger (1975).

[161] Y. T. Lee, R. A. London, G. B. Zimmerman, and P. L. Hagelstein, "Application of escape probability to line transfer in laser-produced plasmas", *Phys. Fluids B* **2**, 2731 (1990).

[162] A. K. Sharma, R. K. Thareja, "Plume dynamics of laser-produced aluminum plasma in ambient nitrogen", *Applied Surface Science* **243**, 68 (2005).

[163] H. Nakano, T. Nishikawa, and N. Uesugi, "Enhanced K-shell x-ray line emissions from aluminum plasma created by a pair of femtosecond laser pulses", *Appl. Phys. Lett.*79, 24 (2001).

[164] H. Ahn, H. Nakano, T. Nishikawa, and N. Uesugi, "Simultaneous Measurement of Absorption and X-Ray Emission from Preformed Plasma Generated by Ultrashort Prepulse", *Jpn. J. Appl. Phys.* **35**, L154 (1996).

[165] T. Feurer, "Feedback-controlled optimization of soft-X-ray radiation from femtosecond laser-produced plasmas", *Appl. Phys. B: Lasers Opt.* **68**, 55 (1999).

[166] U. Teubner, G. Kühnle, and F. P. Schäfer, "Detailed study of the effect of a short prepulse on soft X-ray spectra generated by a high-intensity KrF* laser pulse", *Appl. Phys. B* **54**, 493 (1992).

[167] Th. Schlegel, S. Bastiani, L. Grèmillet, J.-P. Geindre, P. Audebert, J.-C. Gauthier, E. Lebebvre, G. Bonnaud, and J. Delettrez, "Comparison of measured and calculated x-ray and hot-electron production in short-pulse laser-solid interactions at moderate intensities", *Phys. Rev. E* 60, 2209 (1999).

[168] A. Schmitt, R. S. B. Ong, "The effect of collisions on wave-breaking in a cold plasma", *Appl. Phys.* 22,333 (1980).

[169] J. P. Freidberg, R. W. Mitchell, R. L. Morse, and L. I. Rudsinski, "Resonant Absorption of Laser Light by Plasma Targets", *Phys. Rev. Lett.* 28, 795 (1972).

[170] M. Abramowitz and I. Stegun, *Handbook of Mathematical functions*, National Bureau of Standards (1964).

[171] A. Tarasevitch, A. Orisch, D. von der Linde, Ph. Balcou, G. Rey, J. -P. Chambaret, U. Teubner, D. Klöpfel, and W. Theobald, "Generation of high-

order spatially coherent harmonics from solid targets by femtosecond laser pulses", *Phys. Rev. A* **62**, 023816 (2000).

[172] H.-S. Park, D. M. Chambers, H. -K. Chung, R. J. Clarke *et al.*, "High-energy K_α radiography using high-intensity, short-pulse lasers", *Phys. Plasmas* **13**, 056309 (2006).

[173] P. P. Rajeev, S. Banerjee, A. S. Sandhu, R. C. Issac, L. C. Tribedi, and G. R. Kumar, "Role of surface roughness in hard-x-ray emission from femtosecond-laser-produced copper plasmas", *Phys. Rev. A* 65, 052903 (2002).

[174] R. Rix, "Absorption intensiver, ultrakurzer Laserpulse an Festkörpertargets", Diplomarbeit, Max-Planck-Institut Für Quantenoptik, Garching, Germany (1999).

[175] U. Teubner, I. Uschmann, P. Gibbon, D. Altenbernd, E. Förster, T. Feurer, W. Theobald, R. Sauerbrey, G. Hirst, M. H. Key, J. Lister, and D. Neely, "Absorption and hot electron production by high intensity femtosecond uv-laser pulses in solid targets", *Phys. Rev. E* 54, 4167 (1996).

[176] P. Gibbon, M. Mašek, U. Teubner, W. Lu, M. Nicoul, U. Shymanovich, A. Tarasevitch, P. Zhou, K. Sokolowski-Tinten, and D. von der Linde, "Modelling and optimisation of fs laser-produced K_α sources", *Appl. Phys. A* **96**, 23 (2009).

[177] J. M. Dawson, "Particle simulation of plasmas", *Rev. Mod. Phys.* **55**, 403 (1983).

[178] T. Tajima, *Computational Plasma Physics: with Applications to Fusion and Astrophysics*, Addison–Wesley (1989).

[179] C. K. Birdsall and A. B. Langdon, *Plasma Physics via Computer simulations*, IOP Publishing Ltd., Bristol, U. K. (1991).

[180] H. L. Anderson, "Metropolis, Monte Carlo and the MANIAC", *Los Alamos Science* **14**, 96 (1986).

[181] W. Lu, M. Nicoul, U. Shymanovich, A. Tarasevitch, P. Zhou, K. Sokolowski-Tinten, D. von der Linde, M. Mašek, P. Gibbon, and U. Teubner, "Optimized K_α X-ray flashes from femtosecond-laser irradiated foils"**,** *Phys. Rev. E* **80**, 026404 (2009).

[182] D. Riley, J. J. Angulo-Gareta, F. Y. Khattak, M. J. Lamb, P. S. Foster, E. J. Divall, C. J. Hooker, A. J. Langley, R. J. Clarke, and D. Neely, "K_α yields from Ti foils irradiated with ultrashort laser pulses", *Phys. Rev. E* **71**, 016406 (2005).

[183] International Commission on Radiation Units & Measurements Report No. **37**, unpublished (1984).

[184] http://physics.nist.gov/PhysRefData/XrayMassCoef/cover.html

[185] C. Rulliere, *Femtosecond Laser Pulses: Principles and Experiments*, 2nd ed. Springer, (2004).

[186] M. Nicoul, "Time-resolved X-ray diffraction with accelerator- and laser-plasma-based X-ray sources", Dissertation (2010).

[187] A. Ruhl, “Erzeugung intensiver Röntgenimpulse mit einem Bandtarget”, Diplomarbeit (2006).

[188] M. Montel, “Aberrations du Premier Ordre des Systèmes Catoptriques Asymétriques Application au Microscope X à Réflexion Totale”, *Optica Acta* **1**, 117 (1954).

[189] http://www.cxro.lbl.gov/

[190] L. M. P. Fernandes, F. D. Amaro, A. Antognini, J. M. R. Cardoso, C. A. N. Conde, O. Huot, P. E. Knowles, F. Kottmann, J. A. M. Lopes, L. Ludhova, C. M. B. Monteiro, F. Mulhauser, R. Pohl, J. M. F. dos Santos, L. A. Schaller, D. Taqqud and J. F. C. A. Velosoe, “Characterization of large area avalanche photodiodes in X-ray and VUV-light detection”, *Journal of Instrumentation* (JINST) **2**, 08005 (2007).

[191] L. M. P. Fernandes, J. A. M. Lopes, J. M. F. dos Santos, P. E. Knowles, L. Ludhova, F. Mulhauser, F. Kottmann, R. Pohl, D. Taqqu, “LAAPD low temperature performance in X-ray and visible-light detection”, *IEEE Transactions on Nuclear Science* **51**, 1575 (2004).

[192] http://www.caen.it/jsp/Template2/CaenProd.jsp?parent=9&idmod=409

[193] W. Demtröder, *Laser Spectroscopy: Basic Concepts and Instrumentation*, 2nd Edition, Springer-Verlag (1996).

[194] J. Chesnoy and A. Mokhtari, "Resonant impulsive-stimulated Raman-scattering on Malachite Green," *Phys. Rev. A* **38**, 3566 (1988).

[195] A. Tokmakoff, B. Sauter, and M. D. Fayer, “Temperature-dependent vibrational relaxation in polyatomic liquids: Picosecond infrared pump–probe experiments”, *J. Chem. Phys.* **100**, 9035 (1994).

[196] S. Ghosh and B. M. Arora, “Photoreflectance spectroscopy with white light pump beam”, *Rev. Sci. Instrum.* **69**, 1261 (1998).

[197] R. C. Stanley, “Counting statistics in X-ray spectroscopy”, *Br. J. Appl. Phys.* **12**, 503 (1961).

[198] D. Laundy and S. Collins, “Counting statistics of X-ray detectors at high counting rates”, *J. Synchrotron Rad.* 10, 214 (2003).

[199] G. C. Cho, W. Kütt, and H. Kurz, “Subpicosecond time-resolved coherent-phonon oscillations in GaAs”, *Phys. Rev. Lett.* 65, 764 (1990).

[200] S. I. Anisimov, B. L. Kapeliovich, T. L. Perel'man, “Electron emission from metal surfaces exposed to ultrashort laser pulses”, *Sov. Phys. JETP,* **39**, 375 (1974).

[201] M. Ligges, I. Rajkovic, P. Zhou, O. Posth, C. Hassel, G. Dumpich, D. von der Linde, **“**Observation of ultrafast lattice heating using time reolved electron diffraction”**,** *Appl. Phys. Lett.* **94**, 101910 (2009).

[202] P. Chen, I. V. Tomov, and P. M. Rentzepis, "Time resolved heat propagation in a gold crystal by means of picosecondx-ray diffraction", *J. Chem. Phys.* **104**, 10001 (1996).

[203] A. A. Maznev, J. Hohlfeld, and J. Güdde, "Surface thermal expansion of metal under femtosecond laser irradiation", *J. Appl. Phys.* **82**, 5082 (1997).

[204] A. Plech, S. Kürbitz, K. -J. Berg, H. Graener, G. Berg, S. Grésillon, M. Kaempfe, J. Feldmann, M. Wulff and G. von Plessen, "Time-resolved X-ray diffraction on laser-excited metal nanoparticles", *Europhys. Lett.* **61**, 762 (2003).

[205] J. Chen, H. Zhang, I. V. Tomov and P. M. Rentzepis, "Laser Induced Transient Structures in a 150 nm Gold Crystal", *Journal of the chinese chemical society* **54**, 1619 (2007).

[206] P. Musumeci, J. T. Moody, C. M. Scoby, M. S. Gutierrez, and M. Westfall, "Laser-induced melting of a single crystal gold sample by time-resolved ultrafast relativistic electron diffraction", *Appl. Phys. Lett.* **97**, 063502 (2010).

[207] R. Ernstorfer, M. Harb, T. Dartigalongue, C. T. Hebeisen, R. E. Jordan, L. Zhu and R. J. D. Miller, "Femtosecond Electron Diffraction Study on the Heating and Melting Dynamics of Gold", *Springer Series in Chemical Physics* **88**, 755 (2007)

[208] R. Ernstorfer, M. Harb, C. T. Hebeisen, G. Sciaini, T. Dartigalongue, I. Rajkovic, M. Ligges, D. von der Linde, Th. Payer and M. Horn-von-Hoegen, F. -J. Meyer zu Heringdorf, S. G. Kruglik and R. J. D. Miller, "Atomic view of the photoinduced collapse of gold and bismuth", *Springer Series in Chemical Physics* **92**, 113 (2009).

[209] http://www.phasis.ch/

[210] E. D. Palik (Author, Editor), *Handbook of Optical Constants of Solids*, Academic Press (1985).

[211] J. Hohlfeld, J. G. Müller, S. -S. Wellershoff and E. Matthias, "Time-resolved thermoreflectivity of thin gold films and its dependence on film thickness", *Appl. Phys.* B **64**, 387 (1997).

[212] T. Juhasz, H. E. Elsayed-Ali, G. O. Smith, C. Suárez, and W. E. Bron, "Direct measurements of the transport of nonequilibrium electrons in gold films with different crystal structures", *Phys. Rev. B* **48**, 15488 (1993).

[213] S. D. Brorson, J. G. Fujimoto, and E. P. Ippen, "Femtosecond electronic heat-transport dynamics in thin gold films", *Phys. Rev. Lett.* **59**, 1962 (1987).

[214] P. Debye, "Interferenz von Röntgenstrahlen und Wärmebewegung", *Ann. d. Phys.* **348**, 49 (1913).

[215] I. Waller, "Zur Frage der Einwirkung der Wärmebewegung auf die Interferenz von Röntgenstrahlen", *Zeitschrift für Physik A Hadrons and Nuclei* **17**, 398 (1923)

[216] C. Kittel, *Introduction to solid state physics*, 6th ed. Wiley, New York (1986).

[217] G. Busch and H. Schade, *Lectures on solid state physics*, Pergamon Press (1976).

[218] B. C. Larson, J. Z. Tischler and D. M. Mills. "Nanosecond resolution timeresolved x-ray study of silicon during pulsed-laser irradiation", *Journal of Materials Research* **1**, 144 (1986).

[219] S. K. Allison, "The Natural Widths of the K_α X-Ray Doublet from 26FE to 47AG", *The physical review* **44**, 63 (1933).

[220] calculated from XOP, http://www.esrf.eu/computing/scientific/xop2.1/

[221] T. H. Johnson, "The Diffraction of Hydrogen Atoms by the Mosaic Structure of Crystals", *Phys. Rev.* **37**, 87 (1931).

[222] C. Thomsen, J. Strait, Z. Vardeny, H. J. Mark. J. Tauc, and J. Hauser, "Coherent phonon generation and detection by picosecond light pulses", *Phys. Rev. Lett.* **53**, 989 (1984)

[223] C. Thomsen, H. T. Grahn, H. J. Maris, and J. Tauc, "Surface generation and detection of phonons by picosecond light pulses", *Phys. Rev. B* **34**, 4129 (1986).

[224] American Institute of Physics (Author, Corporate Author), Dwight E. Gray (Editor), *American Institute of Physics Handbook*, 3rd ed., McGraw-Hill, Columbus (1972).

[225] S. Kähle, "Kurzzeit-Röntgenbeugung mit Hilfe einer Effizienz-optimierten, hochrepetierenden Laser-Plasma-Röntgenquelle", Dissertation (2009).

[226] P. B. Allen, "Theory of thermal relaxation of electrons in metals", *Phys. Rev. Lett.* 59, 1460 (1987).

[227] J. Hohlfeld, S. -S. Wellershoff, J. Güdde, U. Conrad, V. Jähnke, E. Matthias, "Electron and lattice dynamics following optical excitation of metals", *Chem. Phys.* **251**, 237 (2000).

[228] Online-Datenbank WebElements Periodic Table of the Elements, http://www.webelements.com (Stand November 2008)

[229] B. Rethfeld, A. Kaiser, M. Vicanek and G. Simon, "Ultrafast dynamics of nonequilibrium electrons in metals under femtosecond laser irradiation", *Phys. Rev. B* **65**, 214303 (2002).

[230] R. Peierls, *More Surprises in Theoretical Physics*, Princeton University Press (1991).

[231] H. J. Zeiger, J. Vidal, T. K. Cheng, E. P. Ippen, G. Dresselhauss, and M. S. Dresselhaus, "Theory for displacive excitation of coherent phonons", *Phys. Rev. B* **45**, 768 (1992).

[232] T. K. Cheng, J. Vidal, H. J. Zeiger, G. Dresselhaus, M. S. Dresselhaus, and E. P. Ippen, "Mechanism for displacive excitation of coherent phonons in Sb, Bi, Te, and Ti_2O_3", *Appl. Phys. Lett.* **59**, 1923 (1991)

[233] A. B. Shick, J. B. Ketterson, D. L. Novikov and A. J. Freeman, "Electronic structure, phase stability, and semimetal-semiconductor transitions in Bi", *Phys. Rev. B* **60**, 15484 (1999).

[234] O. Degtyareva, M. I. MCMahon and R. J. Nelmes, "High-pressure structural studies of group-15 elements", *High Pressure Research* **24**, 319 (2004).

[235] T. E. Stevens, J. Kuhl, and R. Merlin, "Coherent phonon generation and the two stimulated Raman tensors", *Phys. Rev. B* **65**, 144304 (2002).

[236] K. Ishioka1, M. Kitajima1, and O. V. Misochko, "Temperature dependence of coherent A_{1g} and E_g phonons of bismuth", *J. Appl. Phys.* **100**, 093501 (2006).

[237] E. D. Murray, D. M. Fritz, J. K. Wahlstrand, S. Fahy, and D. A. Reis, "Effect of Lattice Anharmonicity in Bismuth High-amplitude Phonon Dynamics", *Phys. Rev. B* **72**, 060301 (2005).

[238] X. Gonze, J.-P. Michenaud and J.-P. Vigneron, "First-principles study of As, Sb, and Bi electronic properties", *Phys. Rev. B* **41**, 11827 (1990).

[239] T. K. Cheng, S. D. Brorson, A. S. Kazeroonian, J. S. Moodera, G. Dresselhaus, M. S. Dresselhaus and E. P. Ippen, "Impulsive excitation of coherent phonons observed in reflection in bismuth and antimony", *Appl. Phys. Lett.* **57**, 1004 (1990).

[240] J. S. Lannin, J. M. Calleja and M. Cardona, "Second-order Raman scattering in the group-V_b semimetals: Bi, Sb, and As", *Phys. Rev. B* **12**, 585 (1975).

[241] A. Q. Wu and X. Xu,"Coupling of ultrafast laser energy to coherent phonons in bismuth", *Appl. Phys. Lett.* **90**, 251111 (2007).

[242] E. G. Gamaly, A. V. Rode, "Electron–phonon energy relaxation in bismuth excited by ultrashort laser pulse: temperature and fluence dependence ", *Appl. Phys. A* **online** (2012).

[243] M. Hase, K. Mizoguchi, H. Harima, S. Nakashima and K. Sakai, "Dynamics of coherent phonons in bismuth generated by ultrashort laser pulses", *Phys. Rev. B* **58**, 5448 (1998)

[244] O. V. Misochko, K. Ishioka, M. Hase and M. Kitajima, "Fano interference for large-amplitude coherent phonons in bismuth", *J. Phys.: Condens. Matter* **19**, 156227 (2007).

[245] M. F. DeCamp, D. A. Reis, P. H. Bucksbaum, and R. Merlin, "Dynamics and coherent control of high-amplitude optical phonons in bismuth", *Phys. Rev. B* **64**, 092301 (2001).

[246] O. V. Misochko, Muneaki Hase, K. Ishioka, and M. Kitajima, "Observation of an Amplitude Collapse and Revival of Chirped Coherent Phonons in Bismuth", *Phys. Rev. Lett.* **92**, 197401 (2004)

[247] M. S. Diakhate, E. S. Zijlstra, M. E. Garcia, "Quantum dynamical study of the amplitude collapse and revival of coherent A 1g phonons in bismuth: a classical phenomenon? ", *Appl. Phys. A* **96**, 5 (2009)

[248] D. Boschetto, E. G. Gamaly, A. V. Rode, B. Luther-Davies, D. Glijer, T. Garl, O. Albert, A. Rousse, and J. Etchepare, "Small Atomic Displacements Recorded in Bismuth by the Optical Reflectivity of Femtosecond Laser-Pulse Excitations", *Phys. Rev. Lett.* **100**, 027404 (2008).

[249] M. Hase, M. Kitajima, S.-i. Nakashima, and K. Mizoguchi, "Dynamics of Coherent Anharmonic Phonons in Bismuth Using High Density Photoexcitation", *Phys. Rev. Lett.* **88**, 067401 (2002).

[250] M. Hase, K. Mizoguchi, H. Harima, S. Nakashima, M. Tani, K. Sakai, and M. Hangyo, "Optical control of coherent optical phonons in bismuth films", *Appl. Phys. Lett.* **69**, 2474 (1996).

[251] C. Blome, "Untersuchung schneller Struktur anderungen mit Hilfe ultrakurzer R ontgenimpulse", Dissertation (2003).

[252] S. L. Johnson, P. Beaud, E. Vorobeva, C. J. Milne, É. D. Murray, S. Fahy, and G. Ingold, "Directly Observing Squeezed Phonon States with Femtosecond X-Ray Diffraction", *Phys. Rev. Lett.* **102**, 175503 (2009).

[253] M. Ligges, "Untersuchung der schnellen Gitteraufheizung in dünnen (Halb-) Metallfilmen mit Hilfe zeitaufgelöster Elektronenbeugung", Dissertation (2009).

[254] A. Bugayev, A. Esmail, M. Abdel-Fattah, and H. E. Elsayed-Ali, "Coherent phonons in bismuth film observed by ultrafast electron diffraction", *AIP Advances* **1**, 012117 (2011).

[255] A. Authier, S. Lagomarsino, and B.K. Tanner (Eds), *X-ray and Neutron Dynamical Diffraction Theory and Applications*, New York: Plenum Press (1996).

[256] J. Daillant and A. Gibaud (Eds), *X-ray and Neutron Reflectivity: Principles and Applications*, Lecture Notes in Physics **770**, Springer (2009).

[257] M. Cornacchia, J. Arthur, L. Bentson, R. Carr, P. Emma, J. Galayda, P. Krejcik, I. Lindau, J. Safranek, J. Schmerge, J. Stohr, R. Tatchyn, and A. Wootton, "A Sub-Picosecond Photon Pulse Facility for SLAC", SLAC-PUB-8950 (2001).

[258] P. Tangney and S. Fahy, "Density-functional theory approach to ultrafast laser excitation of semiconductors: Application to the A_1 phonon in tellurium", *Phys. Rev. B* **65**, 054302 (2002).

[259] O. V. Misochko, K. Ishioka, M. Hase and M. Kitajima, "Fully symmetric and doubly degenerate coherent phonons in semimetals at low temperature and high excitation: similarities and differences", *J. Phys.: Condens. Matter* **18**, 10571 (2006).

[260] E. S. Zijlstra, L. L. Tatarinova and M. E. Garcia, "Laser-induced phonon-phonon interactions in bismuth", *Phys. Rev. B* **74**, 220301 (2006).

[261] S. Blügel and G. Bihlmayer, "Full-Potential Linearized Augmented Planewave Method", *Computational Nanoscience: Do It Yourself!* (J. Grotendorst, S. Blügel, D. Marx (Eds.)), *NIC Series* **31**, 85 (2006).

[262] P. Blaha, K. Schwarz, G. K. H. Madsen, D. Kvasnicka, and J. Luitz, "WIEN2k, An Augmented Plane Wave+Local Orbitals Program for Calculating Crystal Properties", Karlheinz Schwarz, Techn. Universität Wien, Austria, (2001).

[263] Z. Yang, C. Ko, and S. Ramanathan, "Oxide Electronics Utilizing Ultrafast Metal-Insulator Transitions", *Annu. Rev. Mater. Res.* **41**, 337 (2011).

[264] A. Pashkin, C. Kübler, H. Ehrke, R. Lopez, A. Halabica, R. F. Haglund, Jr., R. Huber, A. Leitenstorfer, "Ultrafast Insulator-Metal Phase Transition in VO_2 Studied by Multiterahertz Spectroscopy", *Phys. Rev. B* **83**, 195120 (2011).

[265] M. Wuttig, N. Yamada, "Phase-change materials for rewriteable data storage", *Nature Mater.* **6**, 824 (2007).

[266] T. Siegrist, P. Jost, H. Volker, M. Woda, P. Merkelbach, C. Schlockermann and M. Wuttig, "Disorder-induced localization in crystalline phase-change materials", *Nature Mater.* **10**, 202 (2011).

[267] P. Debye and P. Scherrer, "Interferenzen an regellos orientierten Teilchen im Röntgenlicht", *Phys. Z.* **17**, 277 (1916).

[268] http://www.lebowcompany.com/specifications.htm

[269] E. Zolotoyabko, D. Shilo, W. Sauer, E. Pernot, and J. Baruchel, "Visualization of 10 μm surface acoustic waves by stroboscopic x-ray topography"**,** *Appl. Phys. Lett.* **73**, 2278 (1998).

[270] W. Sauer, M. Streibl, T. Metzger, A. Haubrich, S. Manus, W. A., J. Peisl, J. Mazuelas, J. Härtwig, and J. Baruchel, "X-ray imaging and diffraction from surface phonons on GaAs", *Appl.Phys.Lett.* **75**, 1709 (1999).

[271] C. Voisin, D. Christofilos, N. Del Fatti, F. Vallée, "Environment effect on the acoustic vibration of metal nanoparticles", *Physica B: Condensed Matter* **316**, 89 (2002).

[272] P. P. Ewald, "Introduction to the dynamical theory of X-ray diffraction", *Acta Cryst.A* **25**, 103 (1969).

[273] http://photonic-science.co.uk/products/XRAY-cameras-detectors.html#

[274] C. Bressler and M. Chergui, "Ultrafast X-ray Absorption Spectroscopy", *Chem. Rev.* **104**, 1781 (2004).

[275] C. Bressler and M. Chergui, "Molecular structural dynamics probed by ultrafast X-ray absorption spectroscopy", *Annu Rev Phys Chem.* **61**, 263 (2010).

[276] A. O. Er, J. Chen, and P. M. Rentzepis, "Ultrafast time resolved x-ray diffraction, extended x-ray absorption fine structure and x-ray absorption near edge structure", *J. Appl. Phys.* **112**, 031101 (2012).

[277] E. Papalazarou, J. Faure, J. Mauchain, M. Marsi, A. Taleb-Ibrahimi, I. Reshetnyak, A. van Roekeghem, I. Timrov, N. Vast, B. Arnaud, and L. Perfetti, "Coherent Phonon Coupling to Individual Bloch States in Photoexcited Bismuth", *Phys. Rev. Lett.* **108**, 256808 (2012).

[278] M. Nakajima, N. Takubo, Z. Hiroi, Y. Ueda, and T. Suemoto, "Photoinduced metallic state in VO2 proved by the terahertz pump-probe spectroscopy", *Appl. Phys. Lett*. **92**, 011907 (2008).

[279] R. Ulbricht, E. Hendry, J. Shan, T. F. Heinz, and M. Bonn, "Carrier dynamics in semiconductors studied with time-resolved terahertz spectroscopy", *Rev. Mod. Phys.* **83,** 543 (2011).

[280] Time-resolved THz studies of carrier dynamics in semiconductors, superconductors, and strongly-correlated electron materials. Lawrence Berkeley National Laboratory: Lawrence Berkeley National Laboratory. LBNL Paper LBNL-597E. Retrieved from: http://escholarship.org/uc/item/2m32w0fs

[281] O. V. Misochko, K. Ishioka, M. Hase and M. Kitajima, "Fully symmetric and doubly degenerate coherent phonons in semimetals at low temperature and high excitation: similarities and differences", *J. Phys.: Condens. Matter* **18**, 10571 (2006).

[282] arXiv:1212.2348 (http://arxiv.org/pdf/1212.2348.pdf)(2013)

[283] M. Holt, Z. Wu, H. Hong, P. Zschack, P. Jemian, J. Tischler, H. Chen, and T.-C. Chiang, "Determination of Phonon Dispersions from X-Ray Transmission Scattering: The Example of Silicon", *Phys. Rev. Lett.* 83, 3317 (1999).

[284] http://www.rigaku.com/products/components

[285] http://www.roperscientific.de/datasheets/Princeton_Instruments_PI-MTE_1300B_RevA0.pdf

[286] http://www.advancedphotonix.com/ap_products/pdfs/SD394-70-74-591.pdf

Ich bestätige, dass ich die vorliegende Dissertation „Ultrafast time-resolved X-ray diffraction using an optimized laser-plasma based X-ray source“ selbstständig verfasst habe und dabei nur die angegebenen Hilfsmittel verwendet habe.

Darüber hinaus bestätige ich, dass ich die vorliegende Dissertation „Ultrafast time-resolved X-ray diffraction using an optimized laser-plasma based X-ray source“ nur in diesem Promotionsverfahren an der Fakultät für Physik der Universität Duisburg-Essen eingereicht wurde.

Wei Lu

Duisburg， den 01.02.2013